Improved methods for sub-diffraction-limit single-molecule fluorescence measurements

Seamus J. Holden

Linacre College

University of Oxford

A thesis submitted for the degree of

Doctor of Philosophy

Hilary 2011

To John and Mary,
to Paddy and Cathy,
and to Eleanor.

Abstract

I present methods to increase the spatio-temporal resolution of two single-molecule fluorescence methods, which together can be used for measurements over a wide range of biological scales of interest.

On the nanoscale, an important topic is the study of interactions and dynamic fluctuations of DNA-processing biological machines. The characteristic distance scale for these molecules, and therefore the required measurement resolution, is one DNA base-pair (0.34 nm). To achieve this resolution, I quantified and extended the resolution of single molecule Förster resonance energy transfer (smFRET), carried out by total internal reflection fluorescence (TIRF) microscopy (TIRF-FRET), commonly used to monitor biomolecular distances and distance changes in the nanometre range. A theoretical description of the major sources of noise in such measurements was derived, which was found to be in good agreement with experimental results. The major experimental limits to resolution were identified and quantified, and distance differences of just one DNA base-pair were shown to be resolvable. This work paves the way for ultra-high resolution TIRF-FRET studies.

On the microscale, it is of interest to study the spatial organization and co-ordination of multiple molecules within cells, ideally with nanometre resolution; super-resolution microscopy is an ideal candidate for such studies. I present a new algorithm, DAOSTORM, for analysis of localization-based super-resolution data, which has significantly improved performance compared with previous approaches. Previous algorithms required very low densities of simultaneously fluorescently active molecules (imaging density); this allowed fitting of the data with a single model point spread function (PSF). DAOSTORM increases maximum imaging density by an order of magnitude, by simultaneously fitting multiple PSFs to the data. I validated the algorithm using simulations and images of densely-labelled microtubules in eukaryotic cells. DAOSTORM reduces image acquisition times and increases the ultimate spatial resolution of the super-resolution imaging.

These advances will further extend the capabilities of single-molecule fluorescence imaging in biology.

Contents

CHAPTER 1

Introduction

> *These are small. . . but the ones out there are far away.*
>
> Father Ted

The past twenty years have seen a radical shift towards the study of biology at the level of the individual molecule. Since the first room-temperature single-molecule fluorescence measurement in 1990 [1], single-molecule fluorescence methods have offered unprecedented insight into the structure and functions of biomolecules as individual nanoscale machines. This is due to two key advantages of single-molecule methods. Single-molecule methods allow measurements to be performed in inhomogeneous samples containing mixtures of distinct biomolecules, which would be unresolved in an ensemble measurement. The dynamic fluctuations of molecules may also be directly observed; a very difficult task for ensemble measurements, because it requires all molecules in a sample to be carefully synchronized.

Single-molecule Förster resonance energy transfer (smFRET) is a particularly useful method where energy transfer between two molecules reports on their separation on the 2–10 nm scale [2]. The experimental advantages of smFRET have led to numerous advances in our understanding of structural biology, particularly of protein-

folding [3–6] and protein-DNA interactions [7–9]. In total internal reflection fluorescence (TIRF) based smFRET measurements (TIRF-FRET), which are discussed in Chapters 2-4, images of multiple fluorescently-labelled surface-immobilized molecules are recorded. This allows simultaneous FRET measurements of multiple molecules to be carried out for extended periods; which has proved to be particularly useful in the study of protein-DNA interactions [9–12].

The recent advent of super-resolution microscopy, which allows imaging of biological structures with spatial resolution far below the diffraction limit [13] promises to have a similar impact on cell biology. Localization-based super-resolution imaging [14–16], where the super-resolved image is obtained by sampling small subsets of a fluorescently labelled population on a single-molecule basis, is particularly exciting. This method combines the ability to obtain super-resolved images with the advantages of single-molecule measurements, for example allowing super-resolution imaging to be performed simultaneously with single particle tracking [17]. However, the method is limited by the low imaging speed currently possible ($\sim$0.001–1 images s^{-1} [18, 19]), limiting its use for live cell studies [20].

Although single-molecule fluorescence methods have tremendous advantages, they also pose significant additional challenges compared with ensemble measurements. A particularly challenging issue is the massive volume of data produced by these experiments. For imaging-based methods, where a series of images containing many fluorescent molecules is acquired, the data from even a single five-minute measurement is typically over one gigabyte in size. Automated data analysis, and especially *data reduction*, i.e., the identification and extraction of the useful information from the data, is clearly essential if data overload is to be avoided. The primary uniting theme of this thesis is that careful consideration of this part of the experimental process can significantly improve spatio-temporal resolution in single-molecule fluorescence imaging. The secondary, closely related, uniting theme is based on the insight that

the single-molecule image analysis problem is not really a new one; astronomers have been solving almost the same problem for many years. Despite the vast difference in sample size, images of stars acquired with a telescope are surprisingly similar to images of single fluorophores acquired with a microscope [21, 22]. Therefore, when considering how to best optimize data reduction in single-molecule fluorescence imaging, I first considered whether existing methods from astronomy could be used. As a result, the methods presented in this thesis have been significantly influenced by, or in some cases directly adapted from, methods originally developed to study the skies.

Methodological advances are only as useful as they are necessary. The motivation behind this work was a desire to study the bacterial chromosome and its associated processing machinery, in particular DNA polymerase, on both the nano- and micro-scale. On the nanoscale, i.e., the level of the individual polymerase, I am interested in the mechanistic behaviour of DNA polymerase during initiation and replication [11, 23], processes essential to the remarkable fidelity with which the genome is copied [24]. Since replication proceeds one base at a time, a key distance scale for this process is the separation between adjacent base-pairs, just 0.34 nm. A TIRF-FRET assay is in principle ideal for the study of these processes, since it has high spatio-temporal resolution and can be used to study individual molecules for extended periods. However, although single base-pair distance differences have been resolved by coupling it to a much larger distance change [25], or by studying shifts in the mean of a distribution combining measurements of many molecules [11], real-time, direct single-base-pair resolution has been reported only once [11]. In order to put such measurements on a robust footing, a detailed investigation of smFRET resolution using well characterized FRET standards was required.

On the microscale, I am interested in the cellular spatial distribution of molecules such as DNA polymerase, ideally in live cells, with sub-diffraction-limit resolution.

Super-resolution microscopy is a promising candidate for such studies, but the ability to perform super-resolution studies in live cells is hindered by the slow imaging speed of the technique ($\sim$0.001–1 images s^{-1} [18, 19]). Such studies will benefit from methods to increase imaging speed, such as the one introduced in Chapter 6.

In this work I focus on the robustness and resolution of both TIRF-FRET and localization-based super-resolution imaging. For TIRF-FRET I present theoretical predictions which define the limits of resolution of the technique, together with Monte Carlo simulations which I used to test the performance of current smFRET data analysis algorithms. To obtain and accurately analyse the large datasets necessary for experimental characterization of the system, I designed and implemented specialized image analysis software, which will be useful for any TIRF-FRET study. I then present a detailed experimental characterization of the resolution limits of technique using DNA FRET standards, and identify the major experimental factors which lead to deviations from predicted limits. Based on this analysis I was able to demonstrate spatial resolution at the level of distance differences of one DNA base-pair.

For super-resolution imaging, I present a new super-resolution localization algorithm which can analyse data at a surface density of fluorescently active molecules which is 6-fold higher than was possible with previous algorithms. This was achieved by simultaneously fitting multiple model PSFs to the images, thereby explicitly accounting for the possibility of PSF overlap, which can cause significant problems for previous algorithms. Progress in this area was greatly facilitated by the fortuitous observation that an algorithm developed for use in astronomy (and applied only once previously for single-molecule imaging [21]) solves an almost identical problem for images of stars in crowded stellar fields. I successfully adapted this algorithm for use in super-resolution imaging, and quantified its performance using simulated and experimental datasets. The new algorithm facilitates reduced image acquisition times and increases maximum spatial resolution.

In Chapter 2, the principles of fluorescence and FRET are discussed, together with a review of the experimental methods used for widefield-imaging-based single-molecule FRET measurements. In Chapter 3, I present derivations of the theoretical limits of TIRF-FRET measurements, together with a description of the Monte Carlo simulations and image analysis methods used. A comparison of the performance of several image analysis algorithms on simulated data is presented. In Chapter 4, I measure the current experimental limits of TIRF-FRET resolution, and identify and quantify the major sources of error in TIRF-FRET experiments. In Chapter 5, I provide an introduction to localization-based super-resolution microscopy. Finally, in Chapter 6, I present DAOSTORM, a novel super-resolution localization algorithm.

The principal contribution of this thesis is to increase the spatio-temporal resolution of two techniques, both based on single-molecule fluorescence imaging. For smFRET, my contribution was to define the theoretical limits of TIRF-FRET resolution, and to measure both the current experimental limits of resolution, and the key sources of error which must be dealt with to further increase the precision of measurements. For super-resolution imaging, my contribution was to present a novel super-resolution localization algorithm which significantly increases the performance of the technique.

The specific contributions of other parties to the material presented here are clearly identified at the beginning of each chapter. Appendix A contains a list of published works to which I contributed as a D. Phil. candidate.

Fluorescence and FRET

2.1 Introduction

Here, I provide a brief introduction to fluorescence and Förster Resonance Energy Transfer (FRET). Ensemble and single-molecule FRET methods are discussed, focussing in particular on methods to measure FRET for surface-immobilized single molecules via widefield imaging. A brief introduction to algorithms for analysis of widefield-imaging-based FRET data is presented, together with a summary of previous work in this area. Some of the material in this chapter has previously been published as Refs. 26, 27.

2.2 Fluorescence

Fluorescence is the emission of light from a molecule due to relaxation from an excited singlet state to the singlet ground state (green arrow, Figure 2.1, [2]); typically this excited state has a lifetime on the order of nanoseconds [2]. The system may also relax to the excited triplet state by intersystem crossing. Photon emission due to transition from the excited triplet state to the singlet ground state (red arrow, Fig-
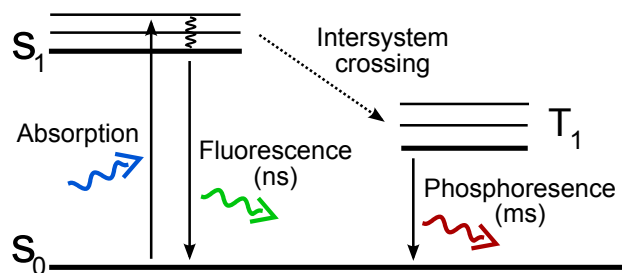
Figure 2.1 *Principle of fluorescence emission.* A fluorophore absorbs a high energy photon *(blue arrow)* and is excited to the S_1 state. A molecule may return to the S_0 state by emission of a photon, i.e., fluorescence *(green arrow)*, with a mean lifetime on the order of nanoseconds. Molecules in the S_1 state can also undergo conversion to the T_1 state via intersystem crossing *(dashed arrow)*. Phosphorescence *(red arrow)*, i.e., transition from T_1 to S_0 is forbidden and occurs on the millisecond timescale.

ure 2.1) is known as phosphorescence. This transition is forbidden, so the phosphorescence lifetime is typically on the order of milliseconds [2]. Collectively, fluorescence and phosphorescence are know as luminescence; photoluminescence (as opposed to chemiluminescence, mechanoluminescence, etc.) occurs as a result of absorption of a photons of a shorter wavelength (blue arrow, Figure 2.1, [2]).

2.3   Förster Resonance Energy Transfer

A particularly interesting fluorescence-related process is Förster Resonance Energy Transfer (FRET). This is the process whereby an excited "donor" molecule transfers energy to a nearby "acceptor" molecule via a non-radiative process (Figure 2.2a-b). If the acceptor molecule is a fluorophore, this may result in fluorescence emission of the acceptor. Classically, FRET occurs due to the coupling of a donor molecule, modelled as an oscillating dipole, with an acceptor dipole of similar resonance frequency [2]*. The rate of energy transfer from the donor to the acceptor, $k_T(r)$ is [2]

$$k_T(r) = \frac{1}{\tau_D} \left(\frac{R_0}{r} \right)^6 , \qquad (2.1)$$

---

*Quantum mechanically, FRET can be considered as due to the exchange of a virtual photon between the donor and the acceptor [28].
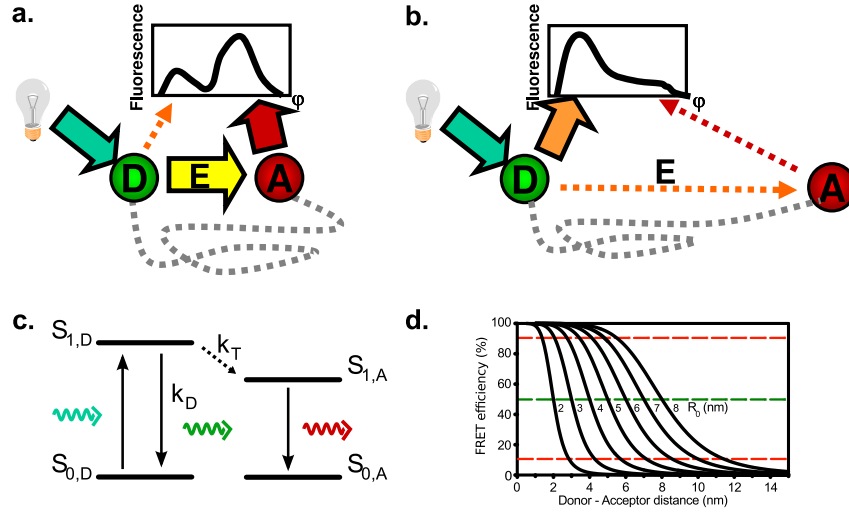
Figure 2.2 *Principle of FRET. (a-b) A donor molecule transfers energy to a nearby acceptor.* The rate of energy transfer, and thus the acceptor emission intensity, is dependent upon the donor-acceptor separation. *(c) Simplified Jablonski diagram for FRET.* The donor molecule absorbs a photon *(blue arrow)*, and is excited to the $S_{1,D}$ state. The donor may emit fluorescence *(green arrow)* or transmit energy to the acceptor through a non-radiative dipole-dipole interaction *(dashed arrow)*. If this occurs, the donor relaxes to the $S_{0,D}$ state and the acceptor is excited to the $S_{1,A}$ state, from which it may emit fluorescence *(red arrow)*. *(d)* FRET efficiency depends upon the donor-acceptor separation and the Förster radius, R_0.

where τ_D is the lifetime of the donor in the absence of the acceptor, r is the separation of the donor and acceptor, and R_0 is the Förster radius. R_0 is given by [2]

$$R_0^6 = \frac{9000(\ln 10)\kappa^2 Q_D}{128\pi^5 N_A n^4} J(\lambda). \tag{2.2}$$

κ^2 is the dipole orientation factor describing the relative orientation of the donor and acceptor transition dipoles. Q_D is the quantum yield of the donor in the absence of the acceptor, where the quantum yield is the fraction of absorbed photons converted to fluorescence. N_A is Avogadro's number. n is the refractive index of the medium. $J(\lambda)$ is the overlap integral, which expresses the degree of spectral overlap between

the donor emission and acceptor absorption spectra:

$$J(\lambda) = \int_0^\infty F_D(\lambda)\varepsilon_A(\lambda)\lambda^4 d\lambda. \tag{2.3}$$

$F_D(\lambda)$ is the normalized fluorescence emission intensity of the donor. $\varepsilon_A(\lambda)$ is the extinction coefficient of the acceptor (in units of $M^{-1}cm^{-1}$).

The energy transfer efficiency, defined here as the *true* FRET efficiency E_T, is the fraction of photons absorbed by the donor which are transferred to the acceptor [2].

$$E_T = \frac{k_T(r)}{\tau_D^{-1} + k_T(r)} \tag{2.4}$$

For a single donor-acceptor pair of fixed separation,

$$E_T = \frac{1}{1 + \left(\frac{r}{R_0}\right)^6}. \tag{2.5}$$

R_0 is typically in the 5–7 nm range [2]; the dependence of E_T on the donor-acceptor separation is plotted in Figure 2.2d for various values of R_0. The size of R_0, which is similar to the diameter of many proteins [2], together with a strongly non-linear distance dependence, makes FRET an ideal "spectroscopic ruler" for sub-diffraction-limit optical measurement of biomolecular distances.

The FRET efficiency can be measured in a number of ways [29, 30]. A common method for steady-state measurements is to measure the relative change in the fluorescence intensity of the donor, in the absence (F_D) and presence of the acceptor (F_{DA}) [2]:

$$E_T = 1 - \frac{F_{DA}}{F_D}. \tag{2.6}$$

The distance between the donor and acceptor may be calculated from a FRET measurement if R_0 is known. It is relatively straightforward to measure most of the factors in Eq. 2.2 [2], however the κ^2 term, which describes the relative orientation of

the dipoles, is difficult to measure directly, and can introduce significant uncertainty in the calculation of R_0 [31]. κ^2 ranges between 0 for perpendicular dipoles and 4 for parallel dipoles. If both dyes have unrestricted rotational freedom, averaging over all orientations gives $\kappa^2 = 2/3$ [31]. Limits can be placed on κ^2 by measurement of the fluorescence anisotropy of the donor and acceptor [31]. The fluorescence anisotropy measures the rotational freedom of the dyes and, for polarized excitation, is defined as [2]

$$r = \frac{I_\perp - I_\parallel}{I_\perp + 2I_\parallel}, \tag{2.7}$$

where $I_\perp$ is the emission intensity perpendicular to excitation, and $I_\parallel$ is the emission intensity parallel to excitation. If the anisotropy of both the donor and acceptor is low, their rotational freedom is high, and thus the assumption $\kappa^2 = 2/3$ is likely to be valid. In the case of high anisotropy and restricted dipole orientation, the uncertainty of the measurement is significantly increased. However, in most cases, FRET is used as a reporter of the presence, relative magnitude and kinetics of a distance *change* rather than as an accurate molecular ruler, so it is often unnecessary to convert FRET measurements to absolute distances.

FRET measurements require specific attachment of donor and acceptor fluorophores to the biomolecules of interest. For example, to measure a distance between a site on a protein and a site on a DNA fragment within a protein-DNA complex, fluorophores need to be incorporated site-specifically in the DNA and the protein; it is common for protein labelling with reactive forms of fluorophores to be preceded by genetic modification of the protein in order to introduce a single reactive site on the protein surface, often a single surface-exposed cysteine residue [32].

In a classic experiment in 1967, Haugland and Stryer verified the r^6 dependence of FRET by using poly-L-proline oligomers of varying lengths as spacers between the donor and acceptor [33]. In 1993, Clegg *et al.* performed similar measurements using double stranded DNA (dsDNA) as a spacer [34]. Such studies established FRET

as an ideal technique for measuring distances and distance changes in biomolecules. Over the last 30 years, ensemble FRET measurements, i.e., FRET measurements in bulk, averaged over large numbers of molecules, have become an essential component of the biochemist's toolkit. *In vitro*, FRET is used for measurements of biomolecular structure and dynamics, especially of proteins [35], nucleic acids [34] and protein-nucleic acid complexes [36]. *In vivo*, FRET can be used to test for interactions between specific proteins [37–39]. Many excellent reviews of ensemble FRET provide a detailed discussion of the method [29, 30, 40–42].

2.4 Single-molecule FRET

Although ensemble FRET methods have yielded significant biological insights, they possess several significant limitations. Since ensemble methods report on the average of billions of molecules, the ability to resolve heterogeneity within a sample is lost. Sample heterogeneity may be divided into two major types. *Static heterogeneity* is due to stable differences between molecules within the sample, e.g., a mixture of active and inactive (e.g., denatured) protein. *Dynamic heterogeneity* is due to time-dependent fluctuations of a single molecule, e.g., changes in shape of a labelled biomolecule; such fluctuations can only be observed at the ensemble level if all molecules in a sample can be temporally synchronized.

Single-molecule FRET (smFRET) allows measurement of both static and dynamic heterogeneity. Additionally, the FRET fluctuations of individual molecules may be monitored for extended periods. These advantages allow a wide range of new phenomena to be studied; in particular, stochastic (and thus unsynchronisable) dynamic fluctuations of biomolecules may be studied.

In recent years single-molecule FRET has yielded many ground-breaking results. Results on biomolecular dynamics include measurements for DNA [25], RNA [43, 44] and proteins [45]. For molecular folding, significant work has been carried out

for proteins [3–6] and RNA [46–48]. For multi-molecular interactions, results have been presented for protein-DNA [7–9], protein-RNA [10, 49] and protein-protein [50] interactions. Measurements for both linear [51, 52] and rotary [53–55] molecular motors have been carried out.

2.4.1   smFRET on the surface

Single-molecule FRET measurements may be carried out for molecules freely diffusing in solution [56] or immobilized on a surface [57]. Diffusion-based smFRET has the significant advantage of simplicity; partially because the apparatus required for such measurements is more simple, but mainly because biomolecules often interact strongly with a nearby glass surface [58]. In order to obtain meaningful results, surface-based experiments usually require much greater optimization and more extensive controls. Despite these challenges, surface-based experiments allow the FRET fluctuations of individual molecules to be studied for extended periods [9], which is a major advantage in the study of molecular machines.

There are two principle methods for surface-based smFRET: confocal microscopy [56, 59] and widefield imaging [57, 60]. Confocal microscopy is a point-detection method involving the imaging of a diffraction-limited spot onto a single avalanche photo-diode. This method has very high time resolution (up to nanoseconds), but as a point-detection method, only one molecule can be detected at a time. It is thus challenging to carry out measurements of large numbers of molecules, which are necessary for robust statistics and are particularly important in the presence of static heterogeneity (e.g., if only a small fraction of molecules show activity or binding).

The alternative is to use a widefield imaging method, where an extended area (typically hundreds of squared microns) is imaged using a sensitive camera, usually an electron multiplying charge coupled device (EMCCD). This allows hundreds of molecules to be imaged simultaneously, albeit with reduced time resolution (order of
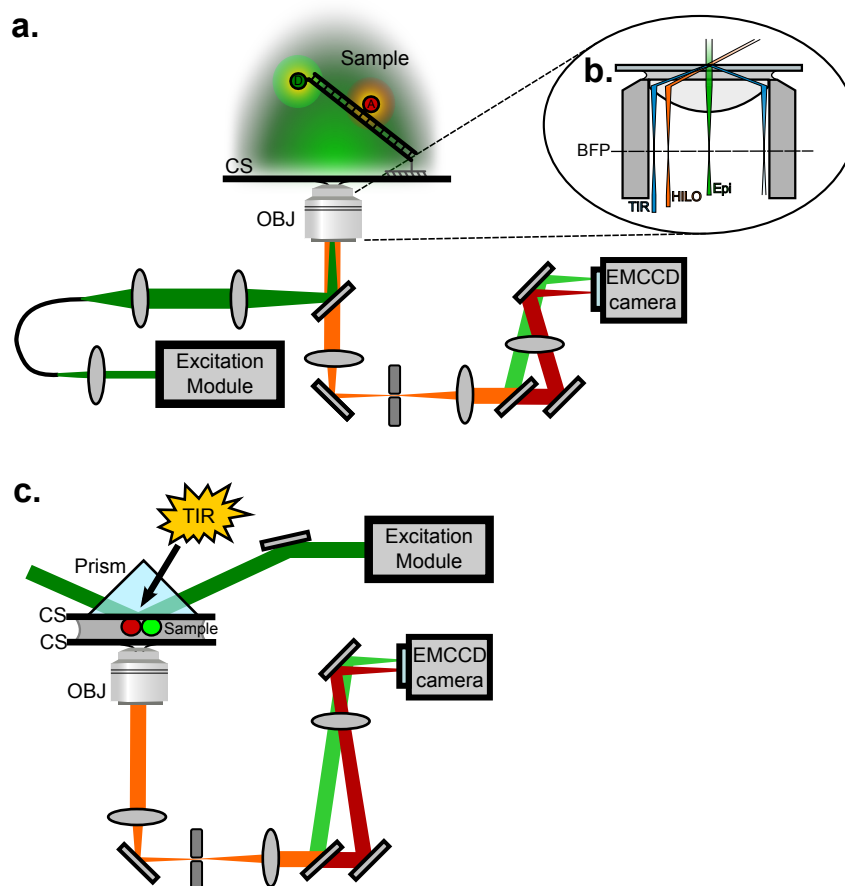
Figure 2.3 *Common widefield FRET imaging schemes. (a-b)* Objective-excitation-based widefield imaging. *(a)* Surface-immobilized molecules are excited and imaged using the same objective lens (OBJ); emitted fluorescence is directed onto an EMCCD camera. *(b)* Objective-excitation based widefield imaging schemes. *BFP*, back-focal-plane; *Epi*, epifluorescence excitation; *HILO*, highly inclined thin illumination excitation; *TIR*, total internal reflection excitation. *(c)* Prism-type TIRF-FRET imaging. *CS*, coverslip; *OBJ*, objective lens.

milliseconds). Common widefield imaging schemes are shown in Figure 2.3. In epifluorescence microscopy [60] (Figure 2.3a-b), the excitation laser is focussed into the back-focal-plane of the objective (green line, Figure 2.3b), resulting in an expanded illuminated area compared to a focus in the object plane. Emitted fluorescence is collected (scattered excitation light being filtered out with a dichroic mirror), split into donor and acceptor emission wavelengths via a second dichroic mirror, and imaged with an EMCCD.

Total internal reflection fluorescence (TIRF) microscopy [46, 57, 61] uses evanescent-wave excitation within a thin layer above a surface to reduce the excitation volume and thus increase the signal to noise ratio (SNR). When a light beam crosses an interface into a medium of lower refractive index and is inclined beyond the critical angle, an evanescent wave is generated close to the interface. The intensity of the field, $I(d)$, decays exponentially with distance

$$I(d) = I_0 e^{-z/d}, \tag{2.8}$$

where z is the distance from the surface and d is a characteristic depth, typically on the order of 100 nm. Because the evanescent wave decays rapidly with distance, single molecules immobilized on the surface can be imaged with little background from molecules diffusing in solution at focal planes away from the surface. There are two common implementations of this method: objective- and prism-type TIRF. In objective-type TIRF (Figure 2.3a-b), the excitation beam is translated parallel to the optical axis towards the edge of the objective lens (blue line, Figure 2.3b). As the displacement is increased, the angle of incidence of the beam with the coverslip increases past the critical angle, and an evanescent wave is generated. In prism-type TIRF (Figure 2.3c), an evanescent wave is generated at the surface of a quartz slide using a prism placed above the objective lens. This arrangement is more experimen-

tally complex, but increases the illuminated area and can give higher signal-to-noise ratio (SNR) [62]. In practice, I found that the decreased experimental complexity of objective-type TIRF more that compensated for the slight decrease in SNR.

Finally, one may use highly inclined and laminated optical sheet (HILO) imaging [63] (Figure 2.3a-b), which is essentially regular epifluorescence imaging, but using a highly inclined beam (orange line, Figure 2.3b). The steep inclination of the beam means that within the small area directly above the objective (i.e., within the imaging area of the detector), only a small volume is excited (although the volume is larger than for TIRF). The excitation volume may also be translated along the z-axis. HILO imaging is primarily useful for *in vivo* applications.

Widefield, and particularly TIRF-based FRET measurements have yielded very useful insights, particularly into the dynamics of nucleic-acid-binding molecular machines such as HIV reverse-transcriptase [10], DNA polymerase [11], RNA polymerase [12] and helicases [9].

2.4.2   Widefield FRET data analysis

Consider an isolated, surface-immobilized, donor- and acceptor-labelled molecule. Emitted fluorescence is collected, split into a donor- and acceptor-emission channels and imaged on an EMCCD. A series of these images is recorded, and the detected photon count for the molecule in the donor- and acceptor-channel, D and A respectively, is extracted from each image as described below. The apparent FRET efficiency E is given by

$$E = A/N, \qquad N = D + A. \tag{2.9}$$

E reports on the separation of the donor-acceptor pair and can be related to E_T upon application of experimentally obtained correction factors [62, 64]. For applications where distance changes, rather than absolute distances are required, calculation of E_T is often unnecessary.

The main advantage of widefield smFRET, its inherent parallelism, increases the complexity of the data analysis compared to point-based methods. Recorded images contain the point-spread functions* (PSFs) of many randomly-distributed surface-immobilized molecules. The analytical challenge is to obtain accurate photon counts for each molecule in the presence of PSF overlap, background noise and optical aberration. Additionally, molecules in the donor and acceptor emission channel must be colocalized in the presence of optical aberrations which cause shifts and distortion between the coordinate systems of each channel.

Previous data analysis algorithms have been relatively simple [48, 62, 66], and the description of the algorithms has been minimal. First, a mapping between each detection channel was generated, typically using fluorescent beads [48, 62, 66]. Second, molecules were identified in a single emission channel by identification of above-threshold pixels in an averaged image of the beginning images of a data series [66], with the position in the second channel assumed to be the same. In Ref. 62, the authors reported colocalization of molecules separately detected in each emission channel, but the details were not elaborated upon. Overlapping PSFs may be excluded based on circular symmetry [66]. Finally, photon counts are measured for each detected molecule for all images in a data series.

Photon counting was typically carried by measuring the sum of pixel intensities in a square region surrounding the molecule position [48, 62, 66] (in subsequent chapters, I refer to this technique as aperture photometry). The mean background level was estimated by calculating the sum of a larger aperture around the central square assumed to contain the PSF. The accuracy of the background estimate can be improved by averaging it over a number of adjacent frames [66]. Algorithms for photon counting via a fit of a model PSF to the data are well established in the context of single-molecule localization [14, 16, 67], and might be expected to give more accu-

---

*The point spread function is the intensity distribution observed in the image plane of an optical system with an input point source [65]

rate results; however this approach has not been commonly reported for FRET data analysis.

I decided that in order to facilitate the high FRET resolution measurements described in subsequent chapters, and to obtain the large statistics necessary for a characterization of the limits of the experimental system, it was necessary to design a more robust and automated TIRF-FRET data analysis algorithm, which is described in Chapter 3.

2.4.3   Alternating Laser Excitation

The capabilities of smFRET were extended by the introduction of the Alternating Laser Excitation (ALEX) scheme [68]. By alternately exciting the sample at the direct-excitation wavelength of the donor and acceptor, significant additional information is obtained. The labelling stoichiometry (i.e., single donor, single acceptor, donor-acceptor, or multiple donors and acceptors) may be determined, allowing virtual molecular sorting, and in particular allowing the "zero-peak" of single-donor labelled molecules to be excluded from analysis; this allows straightforward measurement of low-FRET donor-acceptor labelled molecules, extending the range of FRET measurements. Photophysical fluctuations of either fluorophore, which significantly complicate FRET measurements, can also be detected (see Chapter 4). This extra information is summarized by the fluorescence stoichiometry ratio,

$$S = \frac{D + A}{D + A + AA},$$

(2.10)

where AA is the detected acceptor photon count under direct acceptor excitation.

The combination of TIRF-FRET with ALEX was first demonstrated by Margeat et al. [12]; it has subsequently proved very useful, particularly for the study of nucleic acid machines [10, 66, 69].

Theoretical limits of TIRF-based FRET

3.1   Introduction

Biological systems studied by single molecule FRET (smFRET) are often charac-
terized by distance changes at the nanometre scale. In DNA replication and tran-
scription, for example, the characteristic distance scale is one DNA base-pair (1-bp),
just 0.34 nm [70]. In order to measure distance changes and dynamics on the single-
nucleotide (sub-nanometre) scale, it is necessary to understand completely the sources
of error and heterogeneity that make such dynamics difficult to detect.

A fundamental advantage of smFRET is the ability to resolve sample heterogene-
ity. A sample may contain *static heterogeneity*, i.e., differences between molecules
within the sample (e.g., the sample may contain a mixture of distinct, non-interconvert-
ing species), or *dynamic heterogeneity*, i.e., time-dependent changes of individual
molecules (e.g., conformational changes). In addition to these heterogeneity sources
related to biomolecular function, the resolution of measurements is limited by *intrin-
sic heterogeneity* introduced by experimental noise and error, which must be carefully
investigated in order to accurately quantify smFRET resolution.

Total internal reflection fluorescence (TIRF) microscopy combined with smFRET

(TIRF-FRET, hereafter tFRET), allows multiple surface-immobilized molecules to be imaged simultaneously, allowing static and dynamic heterogeneity to be monitored in complex systems. To characterize the limits of spatial and temporal resolution in tFRET, theoretical predictions for intrinsic heterogeneity are required, together with a robust experimental characterization of the technique using well understood standards. Although such characterization has been reported for confocal smFRET [71–76], this has not been reported for tFRET, a significant omission given the general importance of the method.

A tFRET measurement involves acquisition of a sequence of images of surface-immobilized molecules [62], followed by extraction of FRET data by image analysis. This imaging step adds complexity to the analysis and theoretical description of smFRET heterogeneity compared to diffusion-based smFRET or surface-immobilized confocal smFRET measurements, but careful designing and testing of novel image analysis software allowed us to minimize the effects of these complications.

Building on previous work [71–73, 77, 78], I derived a theoretical description of the heterogeneity expected on a tFRET measurement for a homogeneous, static sample (heterogeneity due to experimental sources of noise). I validated both the image analysis software and theoretical work via Monte Carlo simulations. In the next chapter, I discuss the application of these results to experimental data.

In section 3.2, I develop theoretical descriptions of expected tFRET heterogeneity under a range of conditions. The idea of adapting the work of Thompson [77] to produce a description of tFRET heterogeneity was conceived together with Stephan Uphoff. Stephan Uphoff produced the first realization of this idea (Eq. 3.18 in this work, Eq. 4.10 in Ref. 79), based on error propagation of Thompson's original predictions. I re-derived Thompson's results to correct some theoretical limitations of the original work. I showed that this yields results identical to those presented in Thompson's work, thus confirming the theoretical validity of Thompson's results,

and of Eq. 3.18. I am indebted to an anonymous reviewer of Ref. 80 who identified this theoretical subtlety. I also derived photon counting error predictions allowing for pixellation effects, implied but not stated in Thompson's work. Finally, I present FRET heterogeneity predictions for each of these cases, and also derive predictions for the case of aperture photometry measurements.

In section 3.3.1, I discuss simulation tools developed to validate both the image analysis software and theoretical description. I conceived and implemented the tools for simulation of isolated molecules, building on previous approaches [77, 81]. Johannes Hohlbein wrote the initial version of the simulator for multiple molecule simulations, which I further developed by carrying out significant testing to ensure accuracy of the noise statistics, and by adding a simulator for the electron multiplying gain register.

In section 3.3.2, I discuss the image analysis tools which I wrote for analysis of FRET heterogeneity. The C++ library for PSF fitting described was written by Oliver Britton under my supervision.

All other work was carried out independently.

3.2   Theory

For a surface-immobilized doubly fluorescently-labelled molecule with constant donor-acceptor separation excited at constant intensity, the donor and acceptor fluorescence photon counts are well approximated by independent Poisson distributions [73], with the ratio of the mean acceptor to the sum of donor and acceptor photon counts determined by the accurate ("true") FRET efficiency, E_T, given by Eq. 2.4.

Emitted photons are collected and focused onto an electron-multiplying CCD (EMCCD) camera [82], producing two images containing the point spread functions (PSFs) of immobilized molecules in the donor and acceptor emission channels. Photon counts from the molecular PSFs in the donor and acceptor emission channels are

measured, and the apparent FRET efficiency, E, is calculated using Eq. 2.9. The apparent FRET efficiency reports on the separation of the donor-acceptor pair and can be related to the accurate FRET efficiency, E_T, upon application of correction factors [62, 64]. Although derivations presented here are for apparent (uncorrected) FRET, the same expressions hold for E_T on substitution of corrected photon counts and variances.

The acceptor photon count upon direct acceptor excitation, AA, is measured via alternating laser excitation (ALEX [26, 68, 83]), and the stoichiometry S is calculated via Eq. 2.10. S and AA are used to exclusively select molecules labelled with one donor and one acceptor, and to monitor photophysical fluctuations of either fluorophore.

I derived predictions for heterogeneity on a static homogeneous sample with mean FRET, E_0, in the presence of the heterogeneity sources inherent to a tFRET measurement: shot noise from stochastic photon emission [82], background photons, noise due to the electron-multiplying gain register [84], read-out noise [82], dark noise [82], and noise due to finite spatial resolution of the camera (pixellation effects) [77, 78, 85]. The standard deviation, $\sigma(E)$, of the observed FRET distribution was used as the metric for measurement of heterogeneity.

I derived expressions for limiting heterogeneity in a tFRET measurement using two approaches. First, I calculated predictions assuming image analysis which achieves optimal signal-to-noise (i.e., where the data extraction algorithm is a maximum likelihood estimator). Secondly, predictions were derived for the commonly used data extraction method of aperture photometry (described below), which is not a maximum likelihood estimator. In both cases I obtained predictions for photon counting error in each emission channel, and then used error propagation to obtain FRET heterogeneity predictions.

3.2.1   FRET heterogeneity for maximum likelihood estimators

Building upon previous work [71, 73, 74, 77, 78] I derived expressions for limiting heterogeneity in a tFRET measurement based on χ^2-minimization. For data distributed independently and normally about their true values (a reasonable assumption for a sample with constant donor-acceptor separation [73]), this approach is the maximum-likelihood method [86, 87], and resulting predictions represent the optimal signal-to-noise achievable in a measurement.

The molecular PSF in each channel was modelled as a circular 2D Gaussian distribution [77]:

$$M_{ij} = \frac{M}{2\pi s_M^2} \exp\left(\frac{(i - x_0)^2 + (j - y_0)^2}{2s_M^2}\right) + B_M, \qquad (3.1)$$

where (i, j) are the pixel coordinates; (x_0, y_0) is the position of the molecule; M_{ij} and M are the photon counts for a single pixel and for the entire PSF, respectively, arising from fluorescence emission; s_M is the PSF width; and B_M is the expected background level. There are three significant assumptions in this model.

First, I assumed that the PSF may be modelled as a Gaussian. Recent work [88] showed that fitting to molecular PSFs using a Gaussian model ignores about 65% of a PSF's photons, mainly those contained in its power-law tail, which is ignored/ treated as background by the Gaussian model. However, the Gaussian model is still appropriate for FRET measurements since the mean of the FRET ratio is unaffected by the addition of a fixed fraction to the photon counts. I note that in principle, if the 65% extra photons could be measured and included in the photon count entirely uncontaminated by real background (a non-trivial task), this ideal situation could reduce observed FRET heterogeneity by 30% [H. Flyvbjerg, T. U. Denmark, personal communication, 2010].

Second, I assumed that the PSF may be modelled as circular symmetric for the purposes of the theoretical predictions, despite the experimental data showing non-

negligible asymmetry. This point is discussed in Section 3.2.1.2.

Third, I assumed that the integral of the PSF over an area of one pixel was well approximated by the value of the PSF at the pixel centre multiplied by the pixel area. Mortensen et al. [88] showed this is a good approximation for $s \geq a$, where s is the PSF width defined by Eq. 3.1, and a is the width of a square pixel. This condition is satisfied for data presented in this work; however, where the condition does not hold, photon counting via PSF fitting must take these accounts into consideration [82, 89].

I proceed based on the work of Thompson et al. [77] for the photon-counting error of a conventional CCD camera without an electron multiplying gain register. However, below I note certain limitations of Thompson's original derivation and provide a more robust alternative derivation. I also include electron multiplication effects, noting important experimental considerations which must be taken into account. I explicitly derive predictions (implied in Thompson's work) for photon-counting error, and predictions which include pixellation effects and do not interpolate in the regime where the effects of shot noise and background noise are of similar magnitude.

Having obtained photon-counting error predictions for a single channel, error propagation [90] was used to obtain predictions for the expected heterogeneity on a FRET measurement.

3.2.1.1 Photon counting error for an EMCCD

Fluorescence emission photons are collected from a surface-immobilized biomolecule and focused onto an electron multiplying CCD (EMCCD) camera. The photons collected on a single pixel within the integration time for a single image frame generate electrons amplified in the electron multiplying gain register of the camera, reducing the effective read noise of the device [82]. The amplified electron count is converted to digital units (DU) by the analogue to digital converter. It is these DU which form the pixel counts in the final image of fluorescence emission. For an individual channel,

DUs and photon count are related by:

$$M_{DUij} = UM_{ij}, \quad U = G/C. \tag{3.2}$$

M_{DUij} and M_{ij} are the number of DU and photons collected on a single pixel with index ij, respectively, not including background noise. U is the effective gain (DU/ photon), determined by G, the electron multiplying gain (electrons/ photon), and C, the CCD sensitivity (electrons/ DU). The value of C may be obtained from the camera manufacturer. G is set by the operator and is typically 100-1000 [91]. However, G frequently differs significantly from the manually set value, due primarily to ageing of the EM gain register [92]. For photon-counting applications U should be measured directly on a regular (at least annual) basis using standard methods [93, 94]. The photon count M_{ij} may then be calculated from the pixel count M_{DUij} by Eq. 3.2.

Modifying Thompson's result [77] to include effects of electron multiplication, the expected variance on measured photon count for a single pixel is

$$\sigma_{ij}^2 = f_G^2 M_{ij} + b^2. \tag{3.3}$$

f_G is the excess noise factor introduced by the electron multiplication [91]. For typical values of G (100-1000), $f_G = \sqrt{2}$ to good approximation [91]. The term $f_G^2 M_{ij}$ represents the total contribution of photon-counting shot noise taking into account excess noise from electron multiplication. b is the observed standard deviation of background noise per pixel (excluding photon-counting shot noise), including background in the measurement and any on-camera noise due to read noise and dark noise, which for an EMCCD is expected to be very small. Digitization noise [82, 95] was neglected since its effect is tiny for typical experimental parameters[*]. Dead time and smearing due

---

[*]Merline et al. [95] showed that the contribution of digitization noise to photon counting error is on the order of σ_{fDU}/U, where $\sigma_{fDU} \sim 0.289$ DU, and U is the effective gain. For this work, U=3.1 DU/ photon, and the mean photon count is always at least several hundred photons, making this

to frame transfer [82] were also neglected, since for currently available fluorophores, maximal photon emission rates are such that these effects are not significant.

To obtain a prediction of photon-counting error for a surface-immobilized molecule located at (x_0, y_0), with total expected photon count M_0 and independent Gaussian distributed errors, I begin with the criterion of least-squares fitting, that χ^2,

$$\chi^2(x, y, M) = \sum_{i,j} \frac{\{m_{ij} - M_{ij}(x, y, M)\}^2}{s_{ij}^2}, \tag{3.4}$$

is minimized, where m_{ij} is the observed photon count, M_{ij} is the photon count expected from a model PSF located at (x, y) with total photon count M, and s_{ij}^2 is the observed photon count variance (distinct from the expected variance σ_{ij} defined by Eq. 3.3).

The criterion of least-squares minimization, Eq. 3.4, derives from maximization of the likelihood function [96], $\mathcal{L}(\boldsymbol{\mu}, \boldsymbol{\sigma^2} \mid \boldsymbol{x})$, for n independent, normally distributed, stochastic variables, $X_1, X_2, \ldots, X_n$, where $X_i = \mathcal{N}(\mu_i, \sigma_i^2)$. $x_1, x_2, \ldots, x_n$ are the observations of each variable. The likelihood function for the vector of parameters $(\boldsymbol{\mu}, \boldsymbol{\sigma^2})$ is given by [96]

$$\mathcal{L}(\boldsymbol{\mu}, \boldsymbol{\sigma^2} \mid \boldsymbol{x}) = \frac{1}{\sigma_1 \sigma_2 \ldots \sigma_n (2\pi)^{n/2}} \exp\left[-\frac{1}{2} \sum_{1}^{n} \left(\frac{x_i - \mu_i}{\sigma_i}\right)^2\right]. \tag{3.5}$$

Least-squares minimization corresponds to minimization of the exponent term in Eq. 3.5. However, since the variance, σ_i^2, appears not only in the exponent of this distribution but also in its normalization term, it follows that least-squares minimization is the maximum likelihood estimator of the system only if the variance is held fixed. Use of the expected variance in minimization of Eq. 3.4, as per Ref. 77, means that both the normalization and exponent terms of Eq. 3.5 may vary. Therefore, minimization of a χ^2-statistic based on the expected variance is not necessarily the

---

term negligible.

maximum likelihood estimator of this system.

It is more appropriate to use the observed variance in minimization of Eq. 3.4, assuming the sample size is sufficiently large that the observed variance is a good estimate of the "true" population variance (this criterion being imposed in the derivation by calculating the expectation value of s_{ij}^2 in Eq. 3.7). Fortunately, this derivation produces identical results to the original derivations for photon counting error in Ref. 77 (similarly for localization error).

Using the condition for the minimum, $\partial \chi^2/\partial M = 0$, I expand $M_{ij}(x, y, M)$ about $M_{ij}(x_0, y_0, M_0)$. Considering only first order terms of $\Delta M = M - M_0$, and noting that $\partial s_{ij}^2/\partial M = 0$, I obtain:

$$\Delta M \sim -\frac{\sum\limits_{i,j} \Delta m_{ij} \frac{\partial M_{ij}}{\partial M} / s_{ij}^2}{\sum\limits_{i,j} \left(\frac{\partial M_{ij}}{\partial M} / s_{ij} \right)^2}, \tag{3.6}$$

where $\partial M_{ij}/\partial M$ is evaluated at $M_{ij}(x_0, y_0, M_0)$, and $\Delta m_{ij} = M_{ij}(x_0, y_0, M_0) - m_{ij}$. Squaring Eq. 3.6, calculating the expectation value, and using $\sigma^2(M) = \langle (\Delta M)^2 \rangle$ (because $\langle (\Delta M) \rangle^2 = 0$), yields

$$\sigma^2(M) = \left\{ \sum_{i,j} \left(\frac{\partial M_{ij}}{\partial M} \right)^2 / \langle s_{ij}^2 \rangle \right\}^{-1}. \tag{3.7}$$

Using the fact that the expectation value of the observed variance $\langle s_{ij}^2 \rangle$ equals the expected variance σ_{ij}^2 defined by Eq. 3.3, I obtain,

$$\sigma^2(M) = \left\{ \sum_{i,j} \left(\frac{\partial M_{ij}}{\partial M} / \sigma_{ij} \right)^2 \right\}^{-1}. \tag{3.8}$$

I assume a circular 2D Gaussian PSF (Eq. 3.1) for M_{ij}, as discussed previously. If

pixellation effects are neglected, Eq. 3.8 may be replaced with an integral:

$$\sigma^2(M) \sim \left\{ \int \int \left(\frac{\partial M_{ij}}{\partial M} / \sigma_{ij} \right)^2 didj \right\}^{-1}. \tag{3.9}$$

If I substitute Eq. 3.1 into Eq. 3.9 and assume (following Thompson) that in the intermediate regime where $f_G^2 M_{ij} \sim b^2$, $\sigma(M)$ is well approximated by the sum of the limiting cases when the first and then the second terms in Eq. 3.3 dominate, I obtain:

$$\sigma^2(M) = f_G^2 M + \frac{4\pi s^2}{a^2} b^2. \tag{3.10}$$

To include pixellation effects and avoid interpolation where $f_G^2 M_{ij} \sim b^2$, Eq. 3.1 is substituted into Eq. 3.8, and averaged over all (x_0, y_0):

$$\langle \sigma^2(M) \rangle_{x_0,y_0} = \frac{\int_{-\infty}^{\infty} \int_{-\infty}^{\infty} \sigma^2(M) dx_0 dy_0}{\int_{-\infty}^{\infty} \int_{-\infty}^{\infty} dx_0 dy_0}. \tag{3.11}$$

By symmetry, each pixel is equivalent with respect to (x_0, y_0), allowing us to reduce the range of integration to one pixel in each direction. For square pixels of width a, this yields:

$$\langle \sigma^2(M) \rangle_{x_0,y_0} = a^{-2} \int_0^a \int_0^a \left\{ \sum_{i,j=-\infty}^{i,j=\infty} \left(\frac{\partial M_{i,j}}{\partial M} / \sigma_{i,j} \right)^2 \right\}^{-1} dx_0 dy_0. \tag{3.12}$$

3.2.1.2 Effect of ellipticity on photon counting error

By inspection of Eq. 3.10, the equivalent result for photon counting error of an elliptical Gaussian PSF is:

$$\sigma^2(M) = f_G^2 M + \frac{4\pi s_x s_y}{a^2} b^2, \tag{3.13}$$

where s_x and s_y are the PSF widths along the minor and major axes of the PSF, respectively. However, for simplicity I used the expression for noise on a circular

PSF throughout, even for experimental data with non-negligible ellipticity which was fitted with an elliptical PSF. In that case, I used the average of s_x and s_y in Eq. 3.10. This introduced a small error in the noise estimate on the order of:

$$\epsilon^2 = \frac{4\pi b^2}{a^2} \left\{ \left(\frac{s_x + s_y}{2} \right)^2 - s_x s_y \right\}. \tag{3.14}$$

This reduces to:

$$\epsilon^2 = \frac{\pi b^2}{a^2} (s_y - s_x)^2, \tag{3.15}$$

which is very small unless $s_y \gg s_x$, which is not commonly observed experimentally.

3.2.1.3 Expected FRET measurement error

To obtain a prediction for FRET error, I perform error propagation [74, 90], assuming D and A are independently distributed [73], for apparent FRET, E:

$$E = A/N, \quad N = D + A. \tag{3.16}$$

where D, A and N are the donor, acceptor, and total photon counts for an individual molecule, respectively. Then

$$\sigma(E) = \sqrt{\left(\frac{\partial E}{\partial D} \right)^2 \sigma^2(D) + \left(\frac{\partial E}{\partial A} \right)^2 \sigma^2(A)}, \tag{3.17}$$

which simplifies to

$$\sigma(E) = \frac{1}{N} \sqrt{E_0^2 \sigma^2(D) + (1 - E_0)^2 \sigma^2(A)}, \tag{3.18}$$

where E_0 is the mean FRET value.

For the full prediction of $\sigma(E)$, Eq. 3.12 was numerically integrated for each channel, and the results substituted into Eq. 3.18.

If I neglect pixellation and interpolate between the high shot noise and high background limits, then using Eq. 3.10 I obtain:

$$\sigma(E) = \sqrt{\frac{f_G^2 E_0(1 - E_0)}{N} + \frac{4\pi}{a^2 N^4}\left(D^2 s_D^2 b_D^2 + A^2 s_A^2 b_A^2\right)}. \tag{3.19}$$

E_0 is the mean FRET value. s_D, s_A are the PSF widths in donor and acceptor channels. b_D , b_A are the standard deviations (photons per pixel) of observed background noise in each channel. a is the pixel size. f_G is the excess noise factor.

3.2.2   FRET heterogeneity for aperture photometry

An alternative to least-squares or maximum likelihood approaches to photon counting is to simply count the number of photons within a small circle centred around the PSF. This is known as *aperture photometry* [48, 62, 66, 97, 98], carried out by creating apertures, defined by radii r_1, r_2 and r_3 centred around a molecule. The total collected number of photons is estimated from pixels falling within the aperture defined by $r(ij) < r_1$, where $r(ij)$ is the distance of the pixel at (i, j) from the position of the molecule. The background is estimated from pixels within the annulus defined by $r_2 < r(ij) < r_3$ (I generally set $r_1 = r_2$). The background-subtracted photon count is thus

$$M_{ap} = \sum_{r(ij)<r_1} M_{ij} - \frac{n_{pix}}{n_B} \sum_{r_2<r(ij)<r_3} M_{ij}, \tag{3.20}$$

where n_{pix} is the number of pixels within the inner circle, and n_B is the number of pixels in the annulus,

$$n_{pix} = \sum_{r(ij)<r_1} 1, \quad n_B = \sum_{r_2<r(ij)<r_3} 1. \tag{3.21}$$

Variant methods include the use of square apertures [48, 62, 66] and time-averaging the background value over a number of adjacent frames to reduce noise [66]. I note

that the noise predictions do not necessarily achieve maximum signal-to-noise [95]; I therefore derived a prediction for FRET error on an aperture photometry measurement. The photon-counting error for aperture photometry is given to good approximation [95] by

$$\sigma_{ap}^2(M) = f_G^2 M + \alpha b^2, \quad \alpha = n_{pix}\left(1 + \frac{n_{pix}}{n_B}\right). \tag{3.22}$$

Applying error propagation, a prediction for aperture photometry FRET measurement error may be derived:

$$\sigma_{ap}(E) = \sqrt{\frac{f_G^2 E_0(1 - E_0)}{N} + \frac{1}{N^4}\left(D^2\alpha_D b_D^2 + A^2\alpha_A b_A^2\right)}, \tag{3.23}$$

where E_0 is the mean FRET value, D, A and N are the donor, acceptor and total photon counts. b_D and b_A are standard deviations of background noise in the donor and acceptor channels. α_D and α_A are defined in each channel by Eq. 3.22.

3.3 Methods

3.3.1 Simulations

I carried out Monte Carlo simulations to model tFRET data, including the Poisson noise on detected photons, explicit simulation of electron multiplying gain, simulation of the analogue to digital converter, a general background noise term, and pixellation effects. The position of a molecule was randomly chosen with sub-nanometre accuracy, and the effects of pixellation were simulated using pixel size, a, and PSF widths, s_D, s_A, matching typical experimental values ($a = 94$ nm, $s_D \sim 130$ nm and $s_A \sim 150$ nm).

In order to separate the effects of different noise sources, I carried out two sets of simulations. First, I carried out simulations which neglected the effect of multiple overlapping molecules, by simulating an isolated single molecule randomly positioned within a single pixel at the centre of a small area (24×24 pixels). Second, I analysed

the errors introduced by the presence of multiple overlapping molecules using simulations of multiple molecules of varying surface density, randomly positioned within an area of $256{\times}256$ pixels.

I assume that photon counts in the donor and acceptor channels are independently Poisson distributed variables [73], with mean values

$$\langle D \rangle = N(1 - E_0), \quad \langle A \rangle = NE_0. \tag{3.24}$$

Molecular PSFs are modelled as 2D circular Gaussians (Eq. 3.1) with a total photon count (i.e., volume) determined by Eq. 3.24. The photon count arising from a single molecule for each pixel is then drawn from a Poisson distribution with mean equal to the value of the PSF at that pixel.

The electron multiplying gain was modelled for a 526-stage gain register, matching that of the camera used for experiments (Andor iXon 89, UK). Although it is straightforward to explicitly model each stage of a multi-stage gain register [99], this is an exceedingly slow process. Instead, rejection sampling [100] of the approximate probability density function for electron counts resulting from a gain register [99] was carried out:

$$P(n) \begin{cases} = \frac{(n-m+1)^{m-1}}{(m-1)!(G-1+1/m)^m} \exp\left(-\frac{n-m+1}{G-1+1/m}\right) & \text{if } n \geq m, \\ = 0 & \text{otherwise,} \end{cases} \tag{3.25}$$

where n is the final electron count, m is the input photon count and G is the electron multiplying gain. This algorithm has been shown to be accurate for even low values of G [99], and use of this approximation produces a speed increase of a factor of $\sim$1000. In order to avoid floating point overflow errors during simulation, Eq. 3.25 is refactored slightly, and Stirling's approximation is employed where appropriate (i.e., where it does not cause significant loss of precision); for details see Appendix B.

The analogue to digital converter was simulated by calculating the conversion from electrons to DUs and rounding the result. Finally, a general background noise term was included by adding Gaussian distributed noise with standard deviation $b_{DU} = Ub$ (b_{DU} is the noise measured in DU, U is the effective gain, b is the noise measured in photons), rounding the final result.

Simulations with one molecule per image were written in MATLAB. Simulations with multiple molecules per image were written in C++.

3.3.2   Data analysis: Image analysis

To optimize extracted signal-to-noise and ensure statistical robustness of data, it is important to automate the data extraction from tFRET movies. To this end, I built on previous work within the field of single molecule biophysics [48, 62, 66, 77, 101] and in astronomy [85, 89, 95, 97, 102], which deals with the similar problem of accurate photon-counting for multiple overlapping diffraction limited PSFs using CCDs. I designed and implemented automated and robust image analysis software (called *TwoTone*, available online [103]). Image analysis software was written in MATLAB, except for the PSF-fitting software, which was written as a C++ library with a MATLAB interface.

The source data consists of synchronized movies of fluorescence emission in the donor and acceptor emission channels from multiple randomly distributed surface-immobilized single molecules. Image analysis for tFRET consists of 5 essential steps: *image registration*, *detection & localization*, *association*, *photometry* and *filtering*.

3.3.2.1   Image registration

Image registration is the process of generating a spatial mapping between the donor and acceptor coordinate systems. I apply the simple method of calibration using the leakage of acceptor emission of immobilized fluorescent beads into the donor channel

to identify matching positions in each channel [62, 104]. These "control points" are manually selected using a simple GUI and a spatial mapping is generated between the coordinate systems by solving

$$\mathbf{x_A} = \mathbf{T}\mathbf{x_D}, \tag{3.26}$$

in the least-squares sense, where $\mathbf{T}$ is a projective transformation matrix, $\mathbf{x_D}$ are the donor control points and $\mathbf{x_A}$ are the acceptor control points. The resulting quality of alignment is checked visually using a colour-coded overlay of the green and red channels. The semi-automatic nature of this task is acceptable since it is only necessary to perform it at most once for a daily set of experiments, however it should be straightforward to automate this task [105, 106].

3.3.2.2   Detection & localization

Detection and localization are the steps of automatically detecting molecules, and localizing their centroid. This step is performed separately in each channel. For detection, the classic approach is to apply a high pass spatial filter to remove noise, followed by convolution with a Gaussian mask of size similar to the candidate molecules, followed by identification of above-threshold local maxima [85, 89, 101]. I utilize the fact that molecules are immobilized; therefore auto-detection and localization are only performed at the beginning of a movie, averaging typically 5-10 frames to maximize signal-to-noise.

To localize the centroid to high precision, a small sub-image around each detected molecule is fitted with an elliptical 2D Gaussian [14],

$$M_{ij} = \frac{M}{2\pi s_x s_y} \exp\left(\frac{x'^2}{2s_x^2} + \frac{y'^2}{2s_y^2}\right) + B_M. \tag{3.27}$$

M_{ij} and M indicate the expected photon count for a single pixel and for the en-

tire PSF, respectively; and B_M is the expected background level. y' and x' are the pixel coordinates in the coordinate system aligned to the major and minor axis of the observed elliptical PSF, respectively. $y' = (i - x_0)sin\theta + (j - y_0)cos\theta$, and $x' = (i - x_0)cos\theta - (j - y_0)sin\theta$, where (x_0, y_0) is the expected position of the molecule, (i, j) are the pixel coordinates and θ is the angle between the (i, j) and (x', y') coordinate systems. s_y and s_x are the PSF widths along each elliptical axis. Since θ is a free parameter, the elliptical axis of the fitted PSF is not constrained to only the x or y axis.

Fitting was carried out using ordinary least-squares minimization, with the position of the molecule, (x_0, y_0), set as a free parameter. The fitting algorithm and size of the selected sub-image are identical to that employed for photometry, discussed shortly.

3.3.2.3   Point matching

Point matching is the process of matching detected molecules in the donor channel with molecules in the acceptor channel. If the data were entirely free from noise and optical aberrations, and the coordinate transform matrix was perfectly accurate it would be possible to assume that the position of a donor molecule in the acceptor channel is exactly given by Eq. 3.26. However, primarily due to an imperfect transformation matrix, it is necessary to account for the remaining differences between the apparent positions of a molecule in each channel, or inaccurate photon counts would result. This is achieved by carrying out distance-based hierarchical clustering [107] for both the acceptor channel positions $\mathbf{x_A}$ and the transformed donor channel positions $\mathbf{Tx_D}$. Clusters containing zero or one molecules in each channel are retained, whereas clusters with ambiguous stoichiometry (for example a cluster containing two donor molecules and one acceptor) are discarded.

3.3.2.4 Photometry

Photometry is the term given in astronomy to the measurement of photon counts. The main algorithm used here is *profile-fitting photometry* [14, 81, 89, 102, 108, 109]: fitting of a model PSF profile to an identified molecule. Eq. 3.27 is fitted to a square subimage of width $2w_{im}$*, centred on the position identified during the localization step. The Lourakis implementation [110] of constrained Levenberg-Marquardt optimization [111] was used to carry out *ordinary least-squares (OLS) minimization* [111], i.e., minimization of:

$$OLS = \sum_{i,j} (m_{ij} - M_{ij})^2, \tag{3.28}$$

where m_{ij} is the observed photon count and Eq. 3.27 defines M_{ij}. For algorithmic speed, I set the coordinates (x_0, y_0) as constants (although it is straightforward to relax this assumption if experimental factors such as stage drift are significant). This algorithm implicitly assumes uniform noise across the whole image.

An alternative profile-fitting photometry algorithm is *weighted least-squares (WLS) minimization* defined by Eq. 3.4 and used e.g., by Thompson et al. [77]. OLS implicitly assumes uniform noise throughout the image, whereas WLS explicitly models the noise for each pixel. In principle, where uniform noise cannot be assumed (as is the case for single-molecule fluorescence measurements, due to additional photon-counting shot noise arising directly from the immobilized molecule), WLS might optimize signal-to-noise where OLS fails to do so.

The simplest method available, and one commonly employed for tFRET measurements is *aperture photometry* [48, 62, 66, 97, 98], mentioned in section 3.2.2.

---

*I define the subimage width as $2w_{im}$ for simplicity of comparison with methods which use a circular subimage of radius w_{im}

3.3.2.5   Filtering

A significant concern for the analysis of surface-immobilized molecules is to exclude errors introduced by overlapping unresolved molecules. I use two metrics to identify and exclude overlapping molecules. First, the nearest-neighbour distance between resolved molecules in any channel is calculated, based on the position of molecules in the image used for autodetection. Any resolved molecules with too small separation will significantly affect the measured photon-counts for each molecule, so they are excluded. Secondly, the eccentricity of each molecular PSF is calculated, for each individual frame [14],

$$\varepsilon = \sqrt{1 - \frac{s_y^2}{s_x^2}}, \tag{3.29}$$

where s_y and s_x are the PSF widths along the major and minor axes respectively, defined in Eq. 3.27. Monitoring the eccentricity on a per-frame basis has the additional advantage of providing a robust means to test whether sections of a recorded dataset are significantly out of focus (these sections can then be excluded from analysis if necessary). The most appropriate thresholds for each of these filtering metrics will be explored shortly.

3.4   Results and discussion

3.4.1   Validation of image analysis software

3.4.1.1   Photometry results

I examined the performance of the different photometry methods on simulations of isolated immobilized molecules (Figures 3.1-3.2) for an effective window radius of 6 pixels ($\sim 4s$) and typical experimental parameters specified in the Methods. I set s_D=132 nm and s_A=150 nm. Considering first the photon-counting performance (Figure 3.1), OLS showed the smallest systematic error, but showed a constant $\sim$25 %
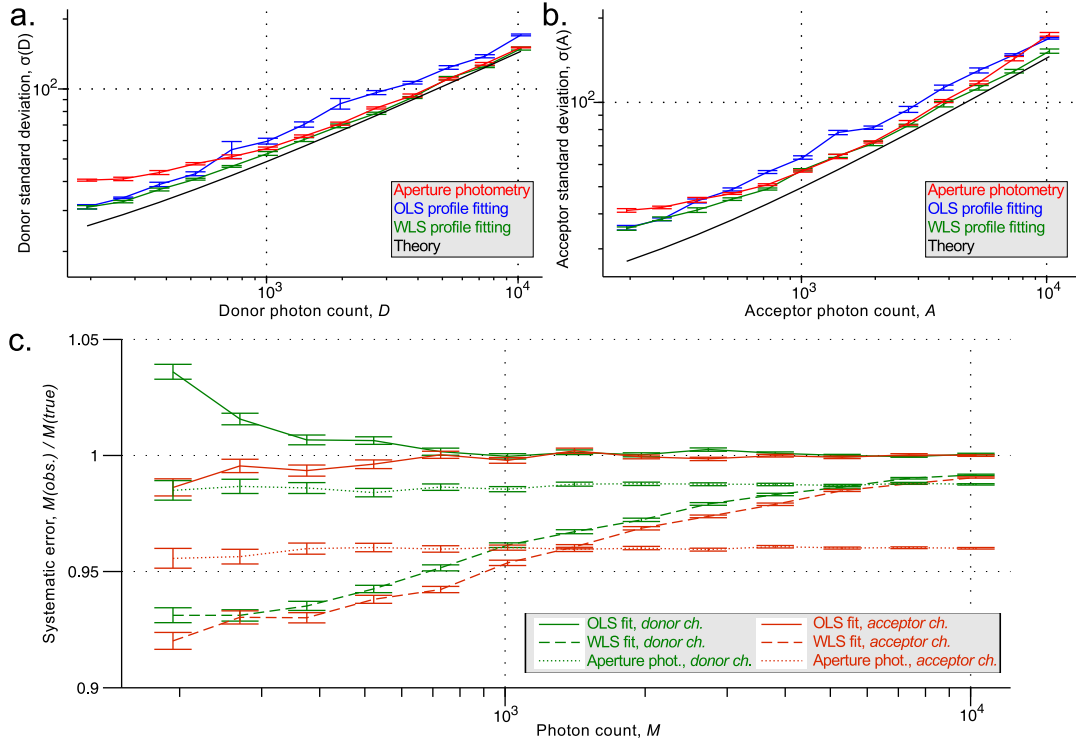
Figure 3.1 *Photon counting performance of different photometry methods. (a-b)* Photon counting standard deviation for increasing photon count. *(a)* Simulations for typical PSF width of donor channel, 132 nm. *(b)* Simulations for typical PSF width of acceptor channel, 150 nm. *(c)* Systematic photon-counting error for increasing photon count. *Green lines*, simulations for donor channel, PSF width 132 nm; *red lines*, simulations for acceptor channel, PSF width 150 nm. *Solid lines*, OLS minimization results; *dashed lines*, WLS minimization results; *dotted lines*, aperture photometry results.

excess noise compared to theoretical predictions. WLS asymptotically approached optimal signal-to-noise, confirming that it was noise introduced by OLS fitting which caused the 25 % error (this finding is supported by previous reports [77, 88]). However, WLS showed significant systematic photon-counting errors, consistent with the literature [87, 112]. In particular, the size of WLS systematic error varied as a function of total photon count, making it unsuitable for accurate measurements. Aperture photometry showed the greatest noise at low photon counts, however, for high photon counts it approached optimal signal-to-noise. Aperture photometry showed significant systematic photon-counting errors, mainly in the acceptor channel (∼4 % error
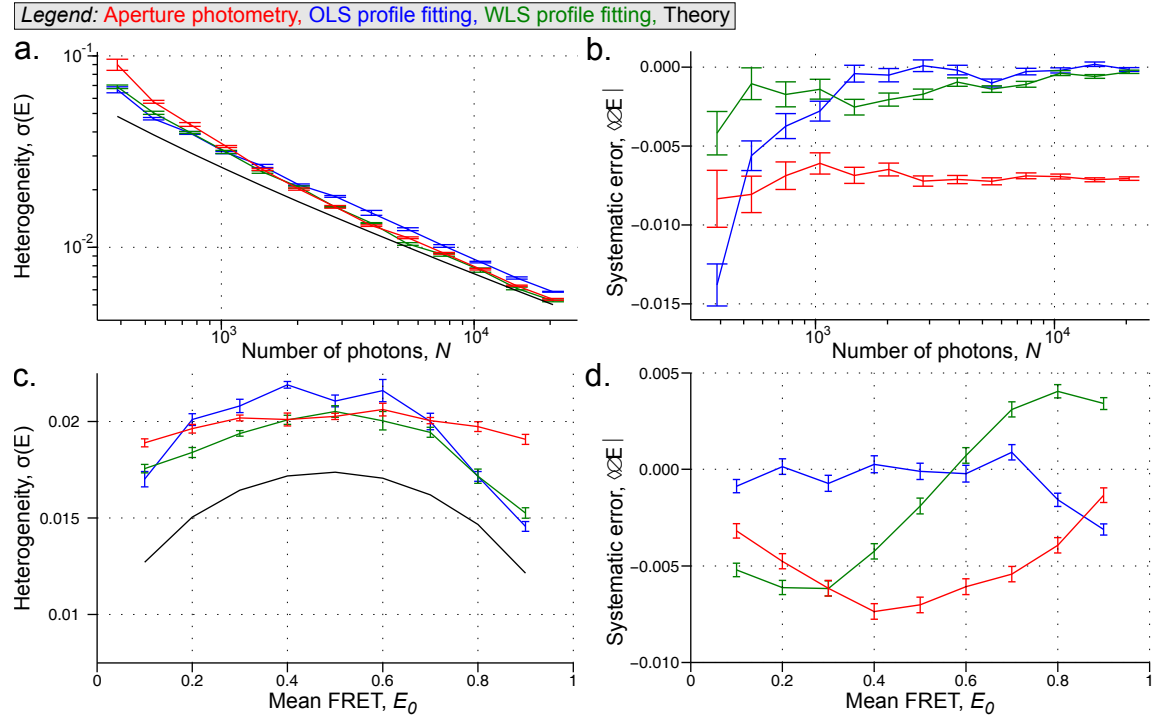
Figure 3.2 *FRET error for different photometry methods. Red line*, aperture photometry; *blue line*, OLS minimization; *green line*, WLS minimization; *black line*, theoretical predictions. PSF width in donor channel, s=132 nm, PSF width in acceptor channel, s=150 nm. *(a-b)* FRET standard deviation and systematic error for increasing photon count, mean FRET 0.5. *(c-d)* FRET standard deviation and systematic error for varying E_0, total photon count per molecule, 2000 photons.

in acceptor channel), which had a larger PSF width[*]. Systematic errors for aperture photometry also caused an eventual increase in observed noise in the acceptor channel (Figure 3.1b).

Next, I analysed FRET measurement performance of the different methods (Figure 3.2). OLS and WLS showed the best performance at low photon counts, with WLS and aperture photometry showing the best performance at high photon counts. At extreme FRET values (E_0=0.1 or 0.9) the performance of aperture photometry suffered because of the low photon counts in one of the channels (Figure 3.2c). Because FRET is a ratiometric method, the systematic errors observed for WLS and aperture photometry photon counts largely cancel out for FRET measurements; systematic

---

[*]I note that approaches exist to correct for these systematic errors [98, 113]

FRET measurement error for either method was effectively negligible.

I recommend the use of OLS profile fitting for the following reasons. I discount first the WLS method because in practice it was found to be rather unstable, requiring good initial estimates of background level and background noise, and knowledge of the effective gain, U (consistent with previous reports [88]). Considering aperture photometry, the method offers acceptable and in some cases better signal-to-noise performance than OLS, and high computational speed. However, I found that OLS is generally a more robust method. OLS shows negligible systematic photon-counting errors, even for quite small effective window radii, w_{im}, whereas aperture photometry requires care in the choice of aperture size to avoid systematic errors. I also found that OLS is less error prone in the presence of nearby or overlapping molecules, since the eccentricity of the OLS fit can be monitored on a per frame basis and used to exclude such molecules (see Section 3.4.1.2). Where x-y stage drift or focal drift is an issue, by relaxing the assumption of fixed position in the fit and by fitting using an elliptical Gaussian, these effects could be minimized by using OLS. The computational speed of OLS is quite acceptable (58 molecular fits per second for a 2.40GHz processor). Finally, the performance of OLS for low photon counts was observed to be better than aperture photometry. However, for low surface density of molecules and high signal-to-noise, aperture photometry is a fast alternative method.

The ideal solution to photon-counting for tFRET is a profile fitting approach which has the advantages described for OLS, but which also obtains optimal signal-to-noise. A recent report by Mortensen by al. [88] shows that maximum-likelihood methods [114] may be just that approach; it should be straightforward to adapt the software describe here to use these methods.

3.4.1.2   Filtering results

The efficiently of the filtering algorithm described at excluding overlapping molecules was tested for Monte Carlo simulated datasets of multiple immobilized molecules in a single fluorescence emission channel. Simulations were carried out for molecules with uniform mean photon count $M = 5000$ photons per molecule/ frame, and fixed surface density, n molecules per μm^2, with a uniform random spatial distribution. Images were generated for a 256×256 pixel imaging grid with pixel size of 94 nm and PSF width of 132 nm, to match typical experimental values for the donor-emission channel. Other simulation parameters were as previously described. Image analysis was carried out as described above, using OLS fitting and including calculation of a 10-frame-averaged image for auto-detection and calculation of nearest-neighbour distance.

I first tested the effectiveness of eccentricity filtering for a random distribution of particles at moderate density (0.86 molecules per μm^2). Distance-based hierarchical clustering [107] was used to segregate the detected points into correctly identified single molecules and multiple molecules incorrectly identified as a single molecule, using a distance threshold of 2.5 pixels (approximately twice the PSF width). The resulting eccentricity distributions were calculated for each case (Figure 3.3a). The distribution including both unresolved and resolved molecules separated into two clear peaks, and the vast majority of overlapping molecules could be excluded by a simple threshold on eccentricity after visual inspection of the eccentricity distribution.

I tested the efficiency of filtering (including both nearest-neighbour distance and eccentricity) in improving photon-counting accuracy, and compared it with the performance expected from a Rayleigh-criterion limited technique. The Rayleigh-limit for a visible light microscope is approximately $\lambda/2$ [65, 115]. For Gaussian PSFs, this roughly corresponds to $\Delta x_{min} \sim 2s$ (s is the PSF width), which I use here as a reference standard for a filtering algorithm with Rayleigh-limit performance. I assume
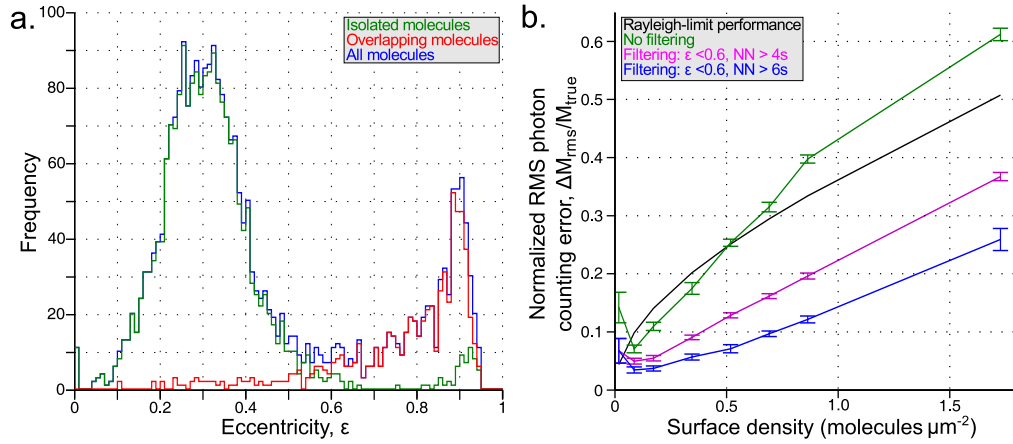
Figure 3.3 *Thresholding based on eccentricity and nearest-neighbour distributions allows discrimination of overlapping molecules with super-Rayleigh-limit performance. (a)* Analysis of the eccentricity distribution for a simulated dataset with moderate surface density (0.86 molecules μm^{-2}). Distribution for all detected positions (*blue line*) is compared with the known stoichiometry of the simulated molecules: isolated molecules (*green line*), multiple overlapping molecules (*red line*). By filtering all molecules after the first major peak in the eccentricity distribution ($\varepsilon < 0.6$), most overlapping molecules were excluded. *(b)* Effect of filtering on normalized RMS photon-counting error for simulated datasets of increasing surface density. *Black line*, photon-counting error assuming Rayleigh-limit performance; *green line*, unfiltered molecules; *pink line*, filtered molecules, minimum nearest-neighbour distance $> 4s$; *blue line*, filtered molecules, minimum nearest-neighbour distance $> 6s$ (s is width of molecular PSF). $\varepsilon < 0.6$ for both filtered datasets.

that the photon count observed for k unresolved molecules is simply the sum of their individual photon counts, kM. For a surface density of n molecules per unit area, I derived an expression for the root-mean-square (RMS) photon-counting error of a theoretical Rayleigh-limit performance filtering algorithm based on simple Poisson statistics[*]:

$$\frac{\Delta M_{rms}}{M_{true}} = \sqrt{\frac{1 - e^{-\mu} - \mu + \mu^2}{1 - e^{-\mu}}}, \quad \mu = 4\pi s^2 n. \tag{3.30}$$

The observed photon-counting errors were analysed for a wide range of surface densities (Figure 3.3b), and the effect of different filtering thresholds. Without filtering, photon-counting errors are approximately at the same level as Rayleigh-limit performance. For a standard eccentricity threshold of $\varepsilon \leq 0.6$ (see Figure 3.3a),

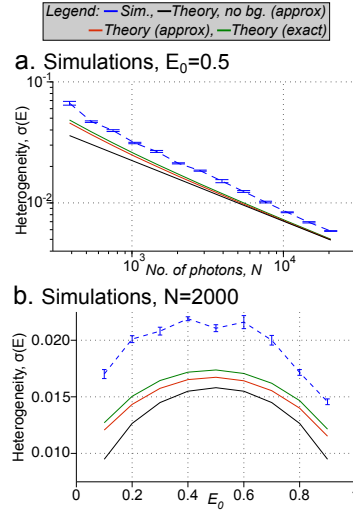---

[*]See Appendix C for derivation.

Figure 3.4   *(a-b) Simulated datasets (sim., blue line) compared to theoretical predictions for a wide range of number of collected photons N (a) and mean FRET efficiencies E_0 (b). Theoretical predictions presented for numerical integration of full theoretical prediction (theory, (exact), green line); for analytic result, Eq. 3.19, with approximations discussed in main text (theory, (approx), red line); and for analytic result, neglecting background noise in the prediction (theory, no bg. (approx), black line). Results in a for E_0=0.50, results in b for N=2000 photons per molecule per frame.*

and different nearest-neighbour thresholds, photon-counting errors were observed to be significantly smaller than the Rayleigh-limit level. Since higher thresholds lead to the exclusion of a larger fraction of candidate molecules, in many cases a low nearest-neighbour threshold of $4s$ is entirely sufficient to give good performance at moderate surface density. For maximum accuracy, a higher threshold of $6s$ reduces photon-counting errors even further.

3.4.2   Validation of theoretical predictions

Having validated the fitting and filtering algorithms, I tested the validity of the theoretical FRET heterogeneity predictions. Predictions were compared to heterogeneity seen in simulations of isolated immobilized molecules (Figure 3.4). For the simplest case where only shot noise was included, FRET heterogeneity decreases as $1/\sqrt{N}$ for increasing photon count N (black line, Figure 3.4a). The heterogeneity has a parabolic

dependence on mean FRET, E_0, reaching a maximum at E_0=0.5 and decreasing for lower or higher FRET (black line, Figure 3.4b). If background noise is included in the predictions, similar behaviour is observed, except that heterogeneity is significantly increased for low photon counts (21 % for $E_0 = 0.5$, $N = 390$ photons) or extreme FRET values (27 % for $E_0 = 0.1$, $N = 2000$ photons), demonstrating the importance of incorporating background noise into predictions (red line, Figure 3.4a-b).

I tested the validity of the assumptions made in derivation of Eq. 3.19 (see Theory section) by performing numerical integration of Eqs. 3.12, 3.17 (green line, Figure 3.4a-b). The numerical predictions are only 6 % larger than those from Eq. 3.19 at low photon counts ($E_0 = 0.5$, $N = 390$ photons), becoming negligible for large photon counts, showing that Eq. 3.19 is an acceptable approximation in most cases. For accuracy, I compared subsequent experimental results with the numerical expression.

Simulations showed good agreement with theoretical predictions for all values of FRET and photon counts, even outside the linear range of FRET (blue dashed line, Figure 3.4a-b); however, the simulations showed constant ∼30 % excess heterogeneity. This arises because the PSF fitting algorithm used (OLS minimization) does not account for shot noise in the image, but assumes constant Gaussian background noise only [77, 88] (as discussed previously). Although the ideal solution would be to remove this excess heterogeneity e.g., by using maximum likelihood methods, this excess heterogeneity is not a serious issue for the analysis of experimental data. In following chapters, to verify that experimental results agreed with the theoretical description of the system, I simply compared observed heterogeneity to predictions based on simulation rather than theory alone, thereby incorporating excess fitting heterogeneity into predictions.

3.5 Conclusions

Here, I developed the theoretical and image analysis tools necessarily to carry out high resolution heterogeneity analysis on experimental data. Each of these tools was validated using Monte Carlo simulations. I derived predictions for expected FRET heterogeneity where the photon counting method applied is a maximum likelihood estimator, for the pixellated and non-pixellated cases. FRET heterogeneity predictions for photon counting via aperture photometry were also derived. An automated, robust approach to tFRET image analysis was described, which I implemented and validated via simulation. These results show that the effects of PSF overlap may be largely excluded if eccentricity and nearest-neighbour thresholding are applied. Of the photon count estimators used, OLS was found to give the most reliable performance; however it introduces $\sim 30\,\%$ excess heterogeneity into results due to incorrect modelling of the background noise. Finally, I tested the FRET heterogeneity predictions against simulations, and found that, once the $\sim 30\,\%$ excess photon counting heterogeneity is accounted for, they agree well. The implementation of photon counting via maximum likelihood methods is expected to resolve the excess heterogeneity issues discussed; I intend to implement this approach in the near future.

The predictions presented here extend previous results for the expected FRET heterogeneity of point-based measurements [71–76] to the case of widefield-imaging based measurements. The TIRF-FRET data analysis algorithm extends previous work [48, 62, 66] to allow robust, automated analysis of large datasets. This will facilitate studies in samples containing significant static heterogeneity. In the following chapter, I apply the predictions and algorithms presented here to rigorously define the current experimental limits of TIRF-FRET resolution.

Experimental limits of TIRF-based FRET

4.1 Introduction

In this chapter, I quantify the current experimental limits of tFRET resolution by comparing the heterogeneity predictions derived in the previous chapter with experimental results for dsDNA FRET standards. Heterogeneity predictions were compared with simulations and experimental data, considering results for static and dynamic heterogeneity separately (I term these analysis methods *dynamic heterogeneity analysis* and *static heterogeneity analysis*, respectively). I then characterized the current limits of spatial and temporal resolution of tFRET. This analysis paves the way for measurement of molecular dynamics within immobilized molecules at timescales inaccessible to dwell time analysis and for design of experiments involving multiple static or molecular subpopulations.

David Yadin optimized the DNA labelling protocol, and labelled approximately half of the dsDNA samples used in this work. Ludovic Le Reste built the TIRF-FRET apparatus and carried out the measurement of R_0 for the Cy3B-Atto647N pair described in Section 4.3.2. All other work was carried out independently.
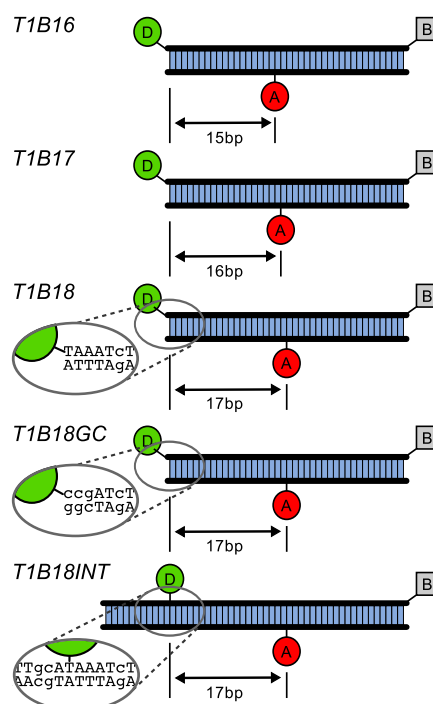
Figure 4.1   *DNA FRET standards used for heterogeneity analysis. D, donor fluorophore; A, acceptor fluorophore; B, biotin. T1B16, T1B17, T1B18*: 15-, 16 and 17-bp donor-acceptor separation, respectively, with an end-labelled donor, and an internally labelled acceptor. *T1B18GC*, 17-bp donor-acceptor separation, sequence adjacent to donor changed to CCG, as shown. *T1B18INT*, 17-bp donor-acceptor separation, internally-labelled donor, modified sequence as shown. Full sequences included in Section 4.2.1.

4.2   Materials and methods

4.2.1   dsDNA FRET standards

The sequences and positions of labels for all dsDNA FRET standards used in this work (shown in Figure 4.1) are listed below. X indicates a 5-C6-Amino-dT, labelled with ATTO647N. Y indicates a 5'-Amino-C6, labelled with Cy3B, except for FRET standard number 5, where Y indicates a 5-C6-Amino-dT, labelled with Cy3B. Amino-modified biotinylated top strand, and amino-modified bottom strand single-stranded DNA was purchased from IBA (Göttingen, Germany). Top strands were labelled with Cy3B, bottom strands with ATTO647N, and purified using denaturing PAGE. Strands were annealed by mixing equimolar amounts of top and bottom strand in

annealing buffer (Tris-HCl pH 8.0, 500 mM NaCl, 1 mM EDTA), and heating to 95 °C, followed by slow cooling to 4 °C.

1. T1B16

    ```
    Top:     Y-5'-TAAATcTAgTAAcATAAggTAAcATAAcgTAAgcTcATTcgcg-3'-Biotin
    Bottom:  3'-ATTTAgATcATTgTAXTccATTgTATTgcATTcgAgTAAgcgc-5'
    ```

2. T1B17

    ```
    Top:     Y-5'-TAAATcTAAgTAAcATAAggTAAcATAAcgTAAgcTcATTcgcg-3'-Biotin
    Bottom:  3'-ATTTAgATTcATTgTAXTccATTgTATTgcATTcgAgTAAgcgc-5'
    ```

3. T1B18

    ```
    Top:     Y-5'-TAAATcTAAAgTAAcATAAggTAAcATAAcgTAAgcTcATTcgcg-3'-Biotin
    Bottom:  3'-ATTTAgATTTcATTgTAXTccATTgTATTgcATTcgAgTAAgcgc-5'
    ```

4. T1B18GC

    ```
    Top:     Y-5'-ccgATcTAAAgTAAcATAAggTAAcATAAcgTAAgcTcATTcgcg-3'-Biotin
    Bottom:  3'-ggcTAgATTTcATTgTAXTccATTgTATTgcATTcgAgTAAgcgc-5'
    ```

5. T1B18INT

    ```
    Top:     5'- gcgTTgcAYAAATcTAAAgTAAcATAAggTAAcATAAcgTAAgcTcATTcgcg-3'-Biotin
    Bottom: 3'- cgcAAcgTATTTAgATTTcATTgTAXTccATTgTATTgcATTcgAgTAAgcgc-5'
    ```

Biotinylated dsDNAs at a concentration of ∼50 pM were surface-immobilized on a polyethylene-glycol coated coverslip [116]. Silicone gaskets (Grace Bio-Labs, USA) were used, covered with an additional glass coverslip to seal the imaging chambers from oxygen. To minimize unwanted stochastic photophysical fluctuations of either dye (photophysics), I used an imaging buffer containing an oxygen-scavenging system and a triplet-state quenching agent: phosphate buffered saline (PBS) pH 7.4, 2 mM TROLOX (6-hydroxy-2,5,7,8-tetramethylchroman-2-carboxylic acid), 1% w/v glucose, 2 mg/ml glucose oxidase, and 80 µg/ ml catalase.
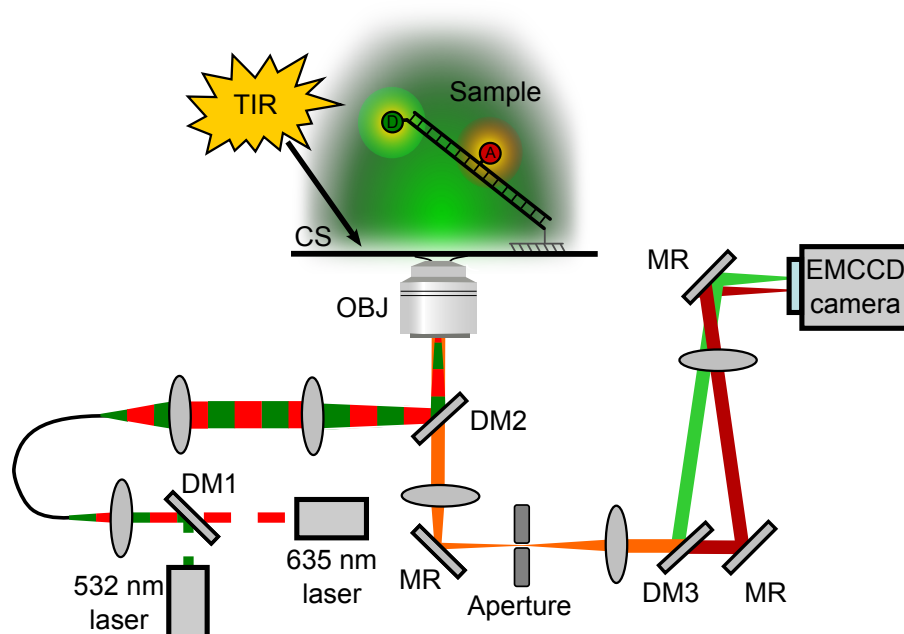
Figure 4.2   *Apparatus for tFRET.* Modulated 532 nm and 635 nm lasers are combined into an optical fibre and excite a surface-immobilised sample in TIRF mode. Fluorescence emission is collected and imaged onto an EMCCD camera. DM, dichroic mirror; BS, beam-splitter; OBJ, objective lens; CS, coverslip; TIR, Total Internal Reflection; MR, mirror; EMCCD, electron-multiplying charge-coupled device.

4.2.2   smFRET data acquisition

I used a custom-built objective-type TIRF apparatus (Figure 4.2) to collect smFRET data for fluorescently labelled dsDNA immobilized on a microscope coverslip. A green laser (532 nm, continuous-wave solid state laser, Samba model, Cobolt, Sweden; modulated using an acousto-optical modulator from AA Optics, France) and a red laser (635 nm, directly modulated diode laser, Cube model, Coherent, USA) operated in ALEX mode [26, 68, 83] were combined via a dichroic mirror and coupled into an optical fibre. The output of the fibre was focused onto the back-focal-plane of the objective lens (100× oil immersion objective, NA 1.4, Olympus, Japan), displaced from the centre of the optical axis such that the excitation light was incident upon the coverslip at an angle greater than the critical angle for total internal reflection, generating an exponentially decaying evanescent wave with a decay constant of ∼100 nm [61], in

order to selectively excite only a small volume adjacent to the coverslip [46, 61]. All experiments were carried out at laser powers of 2 mW (532 nm) and 1 mW (635 nm). An integration time of either 20 ms with 50 Hz frame rate and 25 Hz alternation rate, or of 100 ms with 10 Hz frame rate and 5 Hz alternation rate, was used, the choice for each experiment being specified in Section 4.3. A motorized xy-scanning stage (MS-2000, ASI Imaging, USA) was used to control the sample position relative to the objective.

Emission fluorescence was collected by the objective lens and separated from the excitation light using a dichroic mirror (545 nm/ 650 nm, Semrock, USA) and additional filters (545 nm LP, Chroma, USA; and 633 nm/ 25 nm notch filter, Semrock, USA). The emission fluorescence was then focused through an aperture to make the field of view rectangular, and spectrally separated into green and red emission channels via a dichroic mirror (630 nm DRLP, Omega, USA). The two emission channels were focused side by side onto an EMCCD camera (Andor iXon 897, UK), with pixel size, a, measured as 94 nm using a 10 μm stage micrometer.

4.2.3   Simulations

Monte Carlo simulations of surface-immobilized fluorescent molecules included the effects of shot noise, electron multiplying gain, digitization noise, pixellation noise and Gaussian background noise, as discussed in the Chapter 3. For results in this chapter, isolated immobilized molecules were simulated, neglecting complications due to random PSF overlap. This approximation is supported by results presented in Chapter 3 for multiple randomly distributed surface-immobilized molecules, which showed that the filtering algorithm is effective at excluding the effects of PSF overlap. Simulated PSFs were modelled as circular 2D Gaussian PSFs (Eq. 3.1). All simulation parameters were chosen to match the experimentally observed mean values for each dataset.

4.2.4   Data analysis: Image analysis

Image analysis was carried out as described in chapter 3. Briefly, molecules were automatically identified by convolution of an averaged image of the first 5 recorded frames in each channel* with a Gaussian kernel, and selection of above threshold pixels [85, 101]. Photon counts in each channel were measured by fitting molecular PSFs with an elliptical 2D Gaussian (Eq. 3.27). Fitting was carried out by ordinary-least-squares (OLS) minimization [111], i.e., by minimizing Eq. 3.28.

The apparent FRET, E, and the stoichiometry, S, were calculated (Eqs. 2.9 and 2.10). Only molecules detected in both emission channels (indicating the presence of a single donor and acceptor) were included in the analysis. Molecules with close nearest-neighbours were excluded from the analysis. Data were filtered on a per-frame basis to exclude molecules too dim, too bright, or with large eccentricity (i.e., a very asymmetric PSF, see Eq. 3.29) to minimize errors introduced by overlapping PSFs.

4.2.5   Data analysis: Heterogeneity analysis

I separately performed two types of analysis: heterogeneity analysis on the distributions of individual molecules, which I term *dynamic heterogeneity analysis*, and heterogeneity analysis on the combined distributions of many molecules, which I term *static heterogeneity analysis*. Both include *intrinsic heterogeneity* due to photon-counting shot noise and background noise (determined by Eq. 3.19). In addition to intrinsic heterogeneity, dynamic heterogeneity is sensitive to conformational changes of individual molecules, whereas static heterogeneity is sensitive to constant differences between individual molecules; these latter heterogeneity sources are typically of interest in terms of biomolecular function. Any additional heterogeneity must arise

---

*Precisely, since the experiment is performed using ALEX, 10 frames are required to record 5 frames under donor excitation and 5 frames under acceptor excitation. Additionally, the first frame is skipped, because a quirk of the recording software means this frame is often recorded with the camera's shutter closed.

from unexpected experimental noise or error, which I term *excess heterogeneity*. In particular, since the dsDNA standards were expected to be static and homogeneous, any heterogeneity larger than intrinsic heterogeneity may be identified as excess heterogeneity.

For dynamic heterogeneity analysis, it is important to separate the timescales at which different sources of heterogeneity are significant. To achieve this, I calculated the standard deviation of the difference series [77], formally known as the Allan deviation [117],

$$\sigma_{AD}(E) = \frac{1}{\sqrt{2}} \left\langle (E_{i+1} - E_i)^2 \right\rangle^{1/2}, \qquad (4.1)$$

where i indicates the index in an n data-point time-series. This time-series metric is standard in metrology [117, 118] and is now finding use in biophysics [119, 120] because, unlike the standard deviation, σ_{AD} is sensitive only to noise sources on the timescale of the integration time for a measurement, and not to longer timescale variations. To test for the presence of longer timescale variations, the Allan variance was recalculated after increasing the integration time post-hoc by software binning [120]. Additionally, in the presence of drifts (i.e., any time-correlated variation in mean value) the conventional standard deviation is rather counter-intuitively dependent on the duration of the measurement, whereas the Allan deviation is not [117]. In the absence of drifts, the Allan deviation converges exactly to the conventional standard deviation [117].

For static heterogeneity analysis, since it was not possible to calculate the Allan deviation when combining data from multiple molecules, I calculated the standard deviation from the fit of a 1D Gaussian to the combined histogram of the data.

For heterogeneity analysis of simulated data, the mean and standard deviation was calculated directly from the raw data rather than from a fit to the data. Errors on measurements in all cases represent the standard error on the mean.
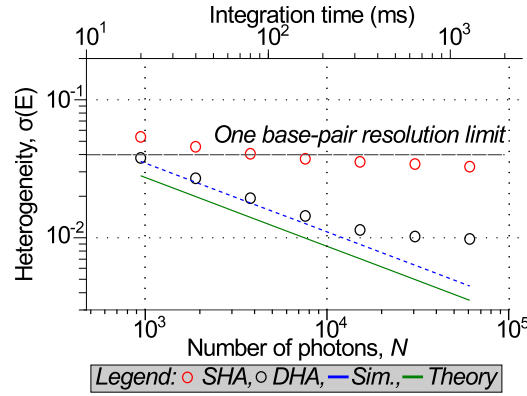
Figure 4.3   *Heterogeneity analysis for 17-bp donor-acceptor separation dsDNA (T1B18, $E_0 = 0.45$).*   Results of dynamic heterogeneity analysis (*dynamic, black circles*) and static heterogeneity analysis (*static, red circles*) compared to predictions from simulation (*blue dashed line*) and theory (*green line*). Heterogeneity $\sigma < 0.04$ is required for 1-bp resolution (see text). Integration time at acquisition was 20 ms; duration of each measurement, 20 s. Each data point combines results for all molecules observed for > 5 frames at that integration time in a 648-molecule dataset from 18 combined FOVs. Simulation parameters matched experimentally observed values at the original 20 ms integration time. Simulation values for longer integration times, τ, were calculated as $\sigma_{sim}(\tau) = \sigma_{sim}(20\text{ms})\sqrt{20\text{ms}/\tau}$.

4.3   Results and discussion

4.3.1   Heterogeneity analysis of dsDNA FRET standards

4.3.1.1   Dynamic heterogeneity analysis

To test whether dynamic heterogeneity present on individual static molecules (with constant donor-acceptor separation) was consistent with theory, I carried out dynamic heterogeneity analysis for 648 dsDNA molecules labelled with donor and acceptor at 17-bp separation (T1B18 standard, $E_0 = 0.45$, black circles, Figure 4.3). When the integration time, and thus photon count per molecule per frame, is increased by post-hoc software binning, dynamic heterogeneity decreases, eventually levelling off towards $\sigma_{AD}(E) = 0.01$. Consistent with results in Figure 3.4a-b, both experimental results and simulations (black circles and blue dashed line respectively, Figure 4.3) showed excess heterogeneity of 30 % compared to theory (due to noise introduced

by the OLS fitting algorithm).

For timescales below 200 ms, good agreement between experimental data and simulation was observed (from 6 % excess heterogeneity at 20 ms up to 14 % excess heterogeneity at 160 ms), validating the description of the major sources of heterogeneity affecting a static sample on short timescales. Furthermore, these results confirm that for timescales between 20 and 200 ms, doubly labelled dsDNA indeed behaves as static FRET standard, with measured heterogeneity arising solely from shot noise, background noise and the OLS algorithm, rather than dynamic fluctuations of the dsDNA or of the fluorophores; previously a topic of some debate [71, 72, 76].

Above 200 ms, I observed significantly excess heterogeneity compared to simulations (black circles deviate from blue dashed line, Figure 4.3, 27 % excess heterogeneity at 320 ms, increasing to 119 % excess heterogeneity at 1280 ms). I investigated the source of this heterogeneity by analysing and manually classifying the individual fluorescence trajectories of all molecules in the dataset (Figure 4.4). Of the 648 molecules, 119 contained too few frames for analysis of dynamics at the longest integration times and were excluded from analysis. The remaining molecules appeared to be separated into three distinct subpopulations (Figure 4.4).

The major population (Figure 4.4a, 227 molecules, 43 %), showed steady FRET, stoichiometry and fluorescence intensities for the entire measurement, resulting in small excess heterogeneity for all measured integration times (Figure 4.4a). A second population (Figure 4.4b, 191 molecules, 36 %), showed step-like fluctuations in FRET coincident with significant changes in stoichiometry and acceptor photon count upon acceptor excitation, but without changes in total photon count under donor excitation. This resulted in large excess heterogeneity for integration times > 200 ms. A third population (Figure 4.4c, 58 molecules, 11 %), showed slow fluctuations in FRET and total photon count under donor excitation, again resulting in large excess heterogeneity for integration times > 200 ms. Finally, 53 molecules (10 %) could not
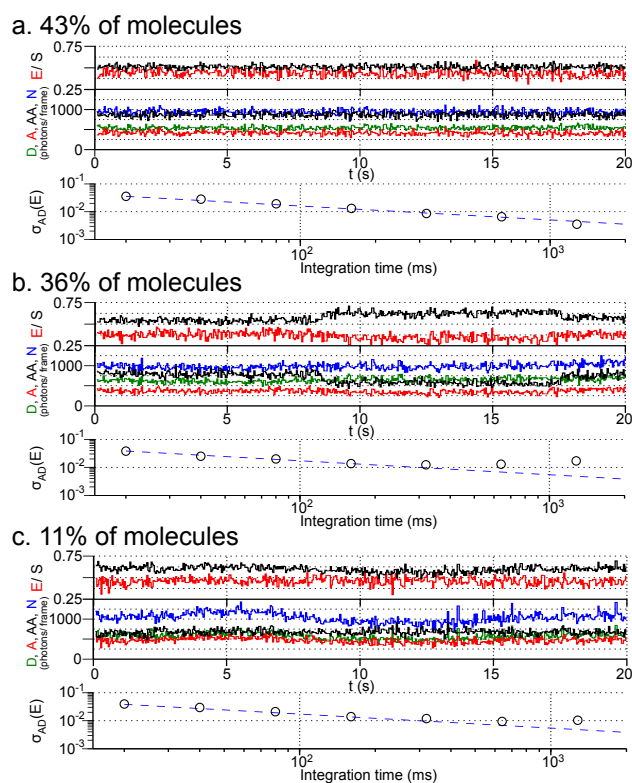
Figure 4.4 *Excess dynamic heterogeneity investigated by manual analysis and classi-fication of molecular subpopulations.* Example of single-molecule time-traces from 648-molecule dataset used for heterogeneity analysis (T1B18, Figure 4.3c). 119 molecules with too few above-threshold frames were excluded from manual analysis. Top: Apparent FRET (*E, red line*) and stoichiometry (*S, black line*). Middle: D, donor excitation donor emission (*green*); A, donor excitation acceptor emission (*red*); AA, acceptor excitation acceptor emission (*black*); total emission during donor excitation, N, (*cyan*). Bottom: Observed Allan deviation, σ_{AD} (*black circles*); predictions from simulation (*blue dashed line*). *(a)* 227 molecules (43 %) show stable fluorescence, FRET and stoichiometry for the duration of the measurement. *(b)* 191 molecules (36 %) show step-like E fluctu-ations with a corresponding sharp change in AA emission and without a corresponding change in N emission, characteristic of acceptor photophysics. *(c)* 58 molecules (11 %) show slow E fluctuations with corresponding slow change in total emission intensity under donor excitation, characteristic of focal drift. 53 molecules (10 %) could not be clearly classified into any of the three populations.

be clearly classified into any of the three populations.

The first population is consistent with static molecules, with heterogeneity as predicted by theory. The second population most likely arises from stochastic photophysical fluctuations in quantum yield and emission or absorption spectra of the acceptor, resulting in a transient change in R_0 for the FRET pair [76]. The first and second populations likely reflect two snapshots of the same underlying population; if the first population were observed for sufficient duration, I expect that stochastic photophysical fluctuations would have been observed. These results establish that acceptor photophysics is the major limiting factor on FRET resolution at long timescales (> 200 ms) for the FRET pair used in this study.

The most likely source of the third population, which showed slow fluctuations in FRET and fluorescence intensity is focal drift (variation in the distance between the coverslip and the objective lens). Although raw images do not show visually detectable focal drift, intensity fluctuations are correlated for a significant minority of the molecules within affected movies (e.g., ∼13 of 42 molecules for the movie presented in Figure 4.5). The fact that intensity fluctuations are not observed for *all* the molecules within affected movies appears to exclude laser power fluctuations as the source of this behaviour. For a stable measurement apparatus and acquisition times of 20 s, the fraction of molecules affected by focal drift was relatively small (10 %), but clearly, focal drift is a significant potential source of excess dynamic heterogeneity for timescales >200 ms.

4.3.1.2   Static heterogeneity analysis

To investigate the static heterogeneity present within ensembles of molecules, I carried out static heterogeneity analysis on the same dataset analysed via dynamic heterogeneity analysis. Static heterogeneity analysis revealed large excess heterogeneity compared with simulations (red circles deviate from blue dashed line, Figure 4.3,
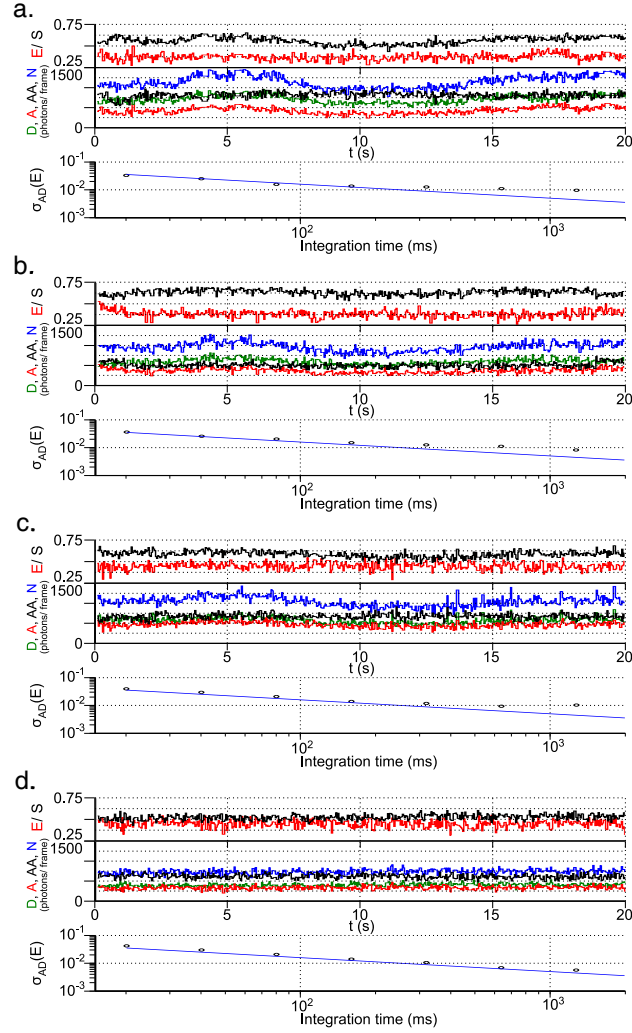
Figure 4.5 *Focal drift within a single FOV causes excess dynamic heterogeneity. (a-c).* Examples of molecules from a single FOV showing slow correlated fluctuations in total photon count N, and excess dynamic heterogeneity, consistent with the source being focal drift. Interestingly, not all molecules within a single FOV appear to be affected by focal drift; an exemplar molecule shown in *d*, from the same FOV as the molecules shown in *a-c* shows stable photon counts and FRET over the whole measurement. For the FOV shown here, only ~ 13 out of 42 molecules within the FOV appeared to be affected by focal drift.

from 50 % at 20 ms to 634 % at 1280 ms). I considered four possible sources of static heterogeneity to explain these deviations:

1. *Intrinsic heterogeneity*, which I use to describe the dynamic heterogeneity on an individual molecule, which largely agreed with theoretical predictions.

2. *Location-dependent heterogeneity*, i.e., heterogeneity across the field of view (FOV), e.g., due to chromatic aberration or image distortion.

3. *Focal drift* on combination of data from multiple fields of view, due to stage drift and manual refocusing between acquisition of images for each FOV.

4. *Inter-molecular heterogeneity*, i.e., differences between individual molecules which remained constant over the duration of the measurement.

To measure the magnitude of the different heterogeneity sources, I carried out static heterogeneity analysis on ensembles of molecules subject to different combinations of static heterogeneity (Figure 4.6). I first measured the heterogeneity on a single individual molecule in a single position on the FOV (*single position*, σ_A, Figure 4.6a), which should reflect only intrinsic heterogeneity. I next measured the heterogeneity on an individual molecule moved to multiple different positions within the FOV using an xy-scanning stage (*multiple positions*, σ_B, Figure 4.6a) which should include intrinsic heterogeneity, location-dependent heterogeneity and focal drift. I also measured the heterogeneity for multiple different molecules in a single FOV, (*multiple molecules*, σ_C, Figure 4.6a) which should include intrinsic heterogeneity, location-dependent heterogeneity and inter-molecular heterogeneity. Finally, the heterogeneity on multiple molecules in multiple FOVs was measured (*multiple FOV*, σ_D, Figure 4.6a), which should include all four heterogeneity sources.

a. T1B18 static heterogeneity   b. Static heterogeneity sources
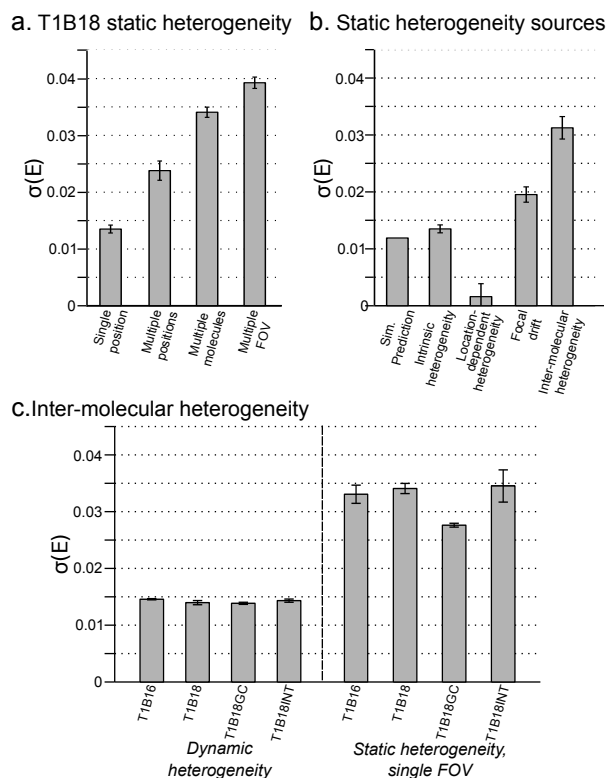
c. Inter-molecular heterogeneity

Figure 4.6   *Sources of static heterogeneity. (a) Sources of static heterogeneity on T1B18 dsDNA standard probed in the presence of different heterogeneity sources. Single position*, static heterogeneity on a single molecule in a single position on the FOV. *Multiple positions*, single molecule moved between multiple different positions on the field of view (FOV) using a scanning stage. *Multiple molecules*, multiple molecules from a single FOV only. *Multiple FOV*, multiple molecules from multiple FOVs. Measurement parameters: Integration time, 100 ms; duration of measurement, 5 s; 80 photons per ms/ molecule. Results for *multiple molecules* and *multiple FOV* from 3 separately prepared samples, > 400 molecules per sample, ~20 FOV per sample. Results for *single position* and *multiple positions* are from 19 molecules, each measured for 5 s in $\geq$ 4 different positions within an area of $\sim$ 1 FOV, yielding in total 84 distinct, randomly distributed positions across the FOV. This dataset is necessarily small, since only molecules within a small area could be used, and all molecules retained in the analysis were excited for >20 s without bleaching. *(b) Magnitudes of static heterogeneity sources calculated using results from a. (c) Inter-molecular heterogeneity investigated using dsDNA FRET standards shown in Figure 4.1.* Measurement parameters: integration time, 100 ms; duration of measurement, 5 s; 80 photons per ms/ molecule; 3 sample repeats for each measurement; > 20 FOV per sample; > 190 molecules per sample.

Assuming linear addition of the variances [90], estimates for the magnitude of the individual heterogeneity sources were obtained using the following simple model:

$$\sigma_A = \sigma_I = 0.0135 \pm 0.0007, \tag{4.2}$$

$$\sigma_B = \sqrt{\sigma_I^2 + \sigma_L^2 + \sigma_F^2} = 0.0238 \pm 0.0017, \tag{4.3}$$

$$\sigma_C = \sqrt{\sigma_I^2 + \sigma_L^2 + \sigma_M^2} = 0.0341 \pm 0.0009, \tag{4.4}$$

$$\sigma_D = \sqrt{\sigma_I^2 + \sigma_L^2 + \sigma_F^2 + \sigma_M^2} = 0.039 \pm 0.001. \tag{4.5}$$

σ_A, σ_B, σ_C and σ_D are the measured heterogeneities, as above, and σ_I, σ_L, σ_F and σ_M are the heterogeneity sources: intrinsic heterogeneity, location-dependent heterogeneity, focal drift and inter-molecular heterogeneity respectively. Solving this model yields estimates for the contribution of each heterogeneity source (Figure 4.6b):

1. Intrinsic heterogeneity, $\sigma_I = 0.0135 \pm 0.0007$

2. Location-dependent heterogeneity, $\sigma_L = 0.0016 \pm 0.0023$;

3. Focal drift, $\sigma_F = 0.0195 \pm 0.0013$;

4. Inter-molecular heterogeneity, $\sigma_M = 0.031 \pm 0.002$.

Intrinsic static heterogeneity is close to predictions from simulations (σ_{sim}=0.0119), consistent with the results of dynamic heterogeneity analysis. Inter-molecular heterogeneity was the largest heterogeneity source, with focal drift also being significant. Location-dependent heterogeneity was not observed, even though some image distortion was visibly present.

Inter-molecular heterogeneity very likely arises due to the slowly-interconverting photophysically distinct states of the acceptor [75, 76], or possibly from slow fluctuations in donor-acceptor separation, e.g., due to DNA-fluorophore interactions [121]. I investigated whether inter-molecular heterogeneity was specific to the DNA sequence,

Sample	Cy3B anisotropy	ATTO647N anisotropy
Cy3B	0.04	N/A
T1B16	0.20	0.15
T1B18	0.22	0.16
T1B18GC	0.22	0.15
T1B18INT	0.22	0.17

Table 4.1 *Ensemble fluorescence anisotropy measurements for dsDNA standards show similar anisotropy for all samples.* The control sample, free Cy3B-NHS ester, showed very low anisotropy consistent with high rotational freedom. All dsDNA FRET standards show increased anisotropy (consistent with slow global rotation of dsDNA), but anisotropy is not sufficiently large to suggest restricted rotational freedom of the fluorophores on the millisecond timescale. Anisotropy is similar for all dsDNA standards suggesting no change in rotational freedom of the dyes between the samples. Measurements carried out in PBS buffer. Cy3B anisotropy measurements were carried out at 540 nm excitation, 580 nm emission. ATTO647N measurements were carried out at 635 nm excitation, 675 nm emission.

FRET values or fluorophore local environment of the sample using 4 different dsDNA standards (Figure 4.1). All 4 samples showed near identical dynamic heterogeneity (Figure 4.6c). Three of the samples (T1B18, T1B16, T1B18INT) showed similar static heterogeneity, measured for a single FOV to exclude focal drift (σ=0.0341±0.0009, 0.0331±0.0016, and 0.0345±0.0002, respectively). In contrast, the sample with a more GC-rich local environment in the region of the donor (T1B18GC) showed a statistically significant reduction in noise ($\sigma = 0.0276$±0.0003). Although the source of this difference is unclear, all the samples showed very similar low steady-state anisotropies (0.15 - 0.22, see Table 4.1), insufficient to indicate restricted rotational freedom on timescales resolvable by tFRET measurements [29]. Additionally, the variation on total photon count upon donor excitation (D) and acceptor photon count upon acceptor excitation (AA) for the different samples was small compared to the error on the measurements, suggesting that sample-specific reduction of donor quantum yield (quenching), or acceptor photophysics, are not responsible for the reduction in heterogeneity.

Photophysical fluctuations cause a much larger increase in static heterogeneity than dynamic heterogeneity, indicating that the ensemble and single molecule averages of this process are not equivalent; this is likely an example of non-ergodicity on the timescale of observation [122]. These results show that recent efforts to reduce static heterogeneity via accurate FRET correction on a single-molecule basis [123] may indeed reduce the effects of a major broadening source (focal drift); however, this approach cannot reduce the largest broadening source, i.e., inter-molecular, position independent heterogeneity (due to photophysics).

4.3.2   Defining the limits of resolution

To quantify the current practical limits of tFRET spatial resolution I compared the observed experimental resolution (Figure 4.3c) with the resolution required to resolve a one base-pair distance difference. The Förster radius, R_0, for Cy3B-A647N on dsDNA was measured as 6.2 nm [2]. I estimated that a distance difference equivalent to a 1-bp step (0.34 nm) corresponded to a FRET difference of $\Delta E = 0.08$ in the range of maximum FRET resolution ($0.4 \lesssim E \lesssim 0.6$) for this pair. Using a Rayleigh-limit approximation [65], $\Delta E_{min} \sim 2\sigma(E)$, a limit on the FRET resolution required to resolve a single base-pair step was obtained, $\sigma_{1bp}(E) < 0.04$.

For studies of dynamic heterogeneity, $\sigma_{1bp}(E) < 0.04$ is observed even at an integration time of 20 ms (60 photons per ms/ molecule) (black circles, Figure 4.3c), showing that 1-bp resolution is possible for measurements of dynamic heterogeneity even at very short integration times and moderate photon counts.

For studies of static heterogeneity, greater excess heterogeneity places 1-bp resolution on the limit of the observed FRET resolution (red circles, Figure 4.3c). To investigate whether this resolution could be achieved, I prepared a mixture of two static dsDNA samples with a D-A separation of 15-bp (T1B16, E_0=0.53 when measured alone, Figure 4.7a, top) and 16-bp (T1B17, E_0=0.47 when measured alone,
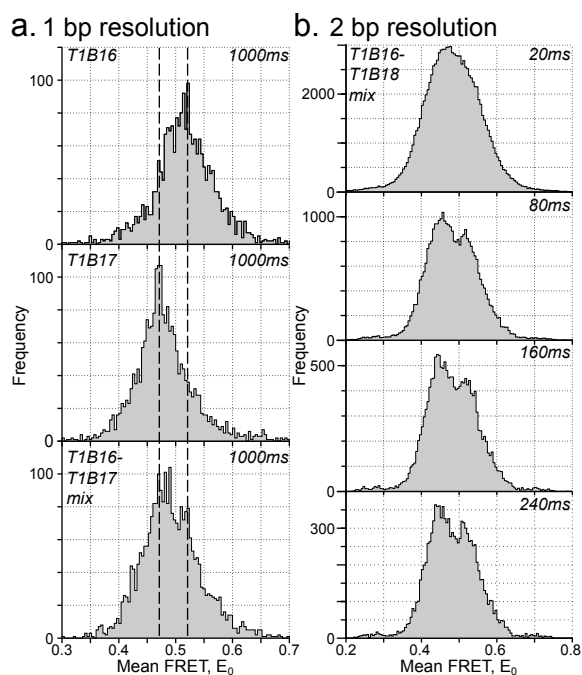
Figure 4.7 *High resolution static heterogeneity analysis. (a) One base-pair resolution with 1000 ms time resolution.* Measured FRET distributions for dsDNA with 15-bp (T1B16) and 16-bp (T1B17) donor-acceptor separation, and for an equimolar mixture of each (T1B16-T1B17 mix). *(b) Two base-pair resolution with 80 ms time resolution.* Measured FRET distribution at increasing integration times for an equimolar mixture of dsDNA with 15-bp and 17-bp D-A separation (T1B16-T1B18 mix). Measurement parameters, 1-bp data: integration time at acquisition, 100 ms; duration of measurement, 5 s; $\sim$50 photons per ms/ molecule; $>$ 1200 molecules; $\sim$ 45 combined FOV. Measurement parameters, 2-bp data: integration time at acquisition, 20 ms; duration of measurement, 20 s; 55 photons per ms/ molecule; 335 molecules; 11 combined FOV.

Figure 4.7a, middle). Resolution was maximized by using software binning to extend integration time to 1000 ms and by sampling a large number of molecules (1236 molecules). This revealed a main peak at $E = 0.47$ and a secondary peak at $E = 0.53$ (Figure 4.7a, bottom), matching the positions of the peaks for the pure T1B17 and T1B16 samples, respectively. However the separation of the two peaks is clearly at the limit of resolution of the measurement; I conclude that 1-bp resolution represents a 'best case' for static heterogeneity studies, at the limit of current experimental capabilities.

To test the minimum distance difference which could be unambiguously resolved, I prepared a mixture of dsDNA standards with a two base-pair distance difference, using dsDNAs with a separation of 15-bp (T1B16, $E_0=0.53$) and 17-bp (T1B18, $E_0=0.45$) (Figure 4.7b). I analysed the observed FRET distributions for the presence of peaks at these E_0 values, acquiring data at 20 ms integration time, using software binning to analyse longer integration times. At 20 ms, the two species were not resolved; however, on increasing the integration time to 80 ms (55 photons per ms/ molecule) the two species were clearly resolved, demonstrating clear two base pair spatial resolution with high temporal resolution. Increasing the integration time to 160 ms and 240 ms further increased resolution.

The resolution limits which I report should be achievable on any apparatus with similar photon detection rates and focal stability to those reported here, using gel-purified dsDNA standards and the Cy3B-ATTO647N FRET pair.

4.4   Conclusions

Despite the importance and popularity of tFRET, a theoretical and experimental characterization of the limits of resolution of the technique has not been previously reported. This is a significant omission, particularly for the ultra-high-resolution studies required for the study of DNA processing machinery such as polymerases and

helicases. To address this, I derived a novel theoretical description of the maximum signal-to-noise achievable for a tFRET measurement, and observed good agreement between theory, simulation and experimental measurements of dynamic heterogeneity at short timescales (< 200 ms). Significant excess heterogeneity was observed for dynamic heterogeneity analysis at long timescales (> 200 ms) and for static heterogeneity analysis over all timescales measured. In both cases, the excess heterogeneity was identified as arising primarily from acceptor photophysics, with focal drift also being significant. Excess static heterogeneity was also dependent on dsDNA sequence adjacent to the donor fluorophore, which merits further investigation.

The current limits of tFRET resolution were quantified. For studies of dynamic heterogeneity, e.g., conformational changes of individual molecules, 1-bp resolution can be achieved for short integration times (20 ms, 60 photons per ms/ molecule). For studies of static heterogeneity, i.e., resolution of multiple species within a single sample, I established that 2-bp resolution is possible even at short integration times (80 ms, 55 photons per ms/ molecule). Previous FRET measurements of distance changes on the order of 1-bp were either based on analysis of the mean values of FRET histograms [11, 72], or exploited the coupling of a small distance change to a larger observable [11, 124]. This quantification of FRET resolution for direct measurements will provide a useful reference for experimental design and analysis, and indicates the feasibility of single base-pair translocation studies for helicases and DNA/ RNA polymerases via tFRET, consistent with recent reports [11].

Clearly, the exact magnitudes of different excess heterogeneity sources will be unique to the tFRET apparatus, FRET pairs and imaging buffers of an individual lab. However, for an optimized tFRET apparatus, I expect that acceptor photophysics and focal drift will be the limiting factors for FRET resolution. Importantly, the methods described here can be applied to any surface-immobilization-based smFRET apparatus (including prism-type TIRF and epifluorescence smFRET apparatus) to

quantify its performance, and determine its FRET-resolution limit; the magnitude of excess heterogeneity and the dsDNA standards reported here may be used as initial reference standards.

The major limiting factors to FRET resolution were identified as acceptor photophysics, emphasizing the fundamental importance of understanding and controlling fluorophore photophysics, and designing more photostable fluorophores. Focal stability of tFRET apparatus was also a limiting factor to FRET resolution even where focal drift was not visibly apparent on raw images, making high focal stability an important consideration in experimental design, particularly for measurements over extended periods (facilitated by optimized fluorophores and buffers [62, 125, 126]). Finally, FRET resolution is also limited by the OLS fitting algorithm used for data extraction. At present, the OLS algorithm does not achieve optimal signal-to-noise, introducing $\sim$30 % excess heterogeneity into measurements. Recent work [88] showed that it should be possible to improve the fitting algorithm by use of maximum-likelihood methods rather than OLS, allowing near-optimal signal-to-noise to be achieved.

These results demonstrate a good predictive understanding of tFRET dynamic heterogeneity at short timescales. Conformational changes in biological systems often occur on the timescale of 1-10 ms, currently at the limit of tFRET temporal resolution (at $\sim$5 ms [127]). This work also paves the way for the extension of Probability Distribution Analysis [23, 71–73, 128] and Burst Variance Analysis [23, 129] to tFRET measurements, which should allow analysis of unresolved dynamic heterogeneity at or just below the temporal resolution of the measurement, extending the utility of the technique.

Super-resolution microscopy

5.1 Introduction

In 1873, Ernst Abbe showed that the resolution of a light microscope is fundamentally limited by diffraction [130]. For over a century, the diffraction limit, ~ 200 nm for visible light, was regarded as unbreakable. For biological research, where the distance scales of interest are the size of eukaryotic cells (several microns), prokaryotic cells (one micron), and of individual proteins (several nanometres), only the largest cellular structures such as microtubule or actin filament networks may be resolved using conventional light microscopy. Although electron microscopy can give far higher resolution (order of nanometres [24]), this requires fixation and harsh treatment of the samples [24], and has poor discrimination between different cellular components [24]. By contrast, fluorescence microscopy allows non-invasive visualization of specific cellular structures in live cells for extended periods [24].

However, the recent advent of "super-resolution" methods has allowed the diffraction limit to be dramatically broken; fluorescence microscopy with resolution of tens of nanometres is now possible [13], and single-nanometre resolution images are on the horizon [131]. In this chapter, I present an introduction to super-resolution mi-

croscopy, and provide a review of existing super-resolution microscopy image analysis algorithms. Table 5.1 was adapted from Ref. 18. Figure 5.1 was adapted from Ref. 132 with permission.

5.2 Principles

The recent advances in spatial resolution have been largely brought about by two approaches. The first class of methods, "patterned-illumination-based" super-resolution microscopy [133, 134] uses a non-uniform excitation illumination to circumvent the diffraction limit. Patterned-illumination methods may be further divided into two main approaches.

The first patterned-illumintation method is called RESOLFT (reversible saturable optical fluorescence transitions) microscopy [135], which uses non-uniform illumination coupled with scanning point-based detection to achieve super-resolution. Conceptually, RESOLFT methods use non-uniform illumination to switch all molecules in an envelope outside of a small, sub-diffraction-limit-sized volume into a dark state. Therefore, only the molecules in the sub-diffraction-limit-sized emission volume remain fluorescently active. All the fluorescence collected must come from the sub-diffraction-limit-sized emission volume; thus the diffraction limit is broken. The emission volume is raster scanned throughout the sample, and a super-resolution image is obtained.

The most common implementation of RESOLFT is Stimulated Emission Depletion (STED [136]) microscopy; I discuss the principles of two-dimensional STED here. Here, a "probe beam" is focussed to a diffraction limited spot and used to excite molecules in the sample. A few hundred picoseconds later, a doughnut-shaped "STED beam" focus, causes molecules in the area around the centre of the probe focus to return to their ground state by stimulated emission, without emitting fluorescence. Only molecules within a smaller, sub-diffraction-limit sized area emit fluorescence;

		Widefield	Structured illumination	STED	STORM/ PALM
xy-**resolution**	Typ.	200–250 nm	130 nm	25–80 nm	25–40 nm
	Best			≤10 nm	~10 nm
z-**resolution**	Typ.	500–700 nm	250 nm	150–600 nm	60 nm–none
	Best		200 nm	30 nm	~10 nm
Speed, large field of view	Typ.	1–10 im. s^{-1}	0.1–1 im. s^{-1}	0.05–0.3 im. s^{-1}	0.001 im. s^{-1}
	Best	30–100 im. s^{-1}	~10 im. s^{-1}	1 im. s^{-1}	1 im. s^{-1}
Speed, small field of view	Typ.	Similar to above	Similar to above	~1 im. s^{-1}	Similar to above
	Best.			10–60 im. s^{-1}	
Instrument complexity		Low	Medium	High	Low–high
Imaging regime		Continuum	Continuum	Continuum	Single molecule

Table 5.1 *Comparison of microscopy methods.* Typical and best case performance is indicated. Typ., typical; im., images. Adapted from Ref. 18, 19.

this sub-diffraction-limited spot is raster scanned through a sample, producing a super-resolved image. The area of the fluorescently emitting region, and thus the image resolution, is determined by the laser power of the STED beam [13],

$$\delta \approx \Delta/\sqrt{I_{STED}/I_{sat} + 1}. \tag{5.1}$$

δ is the resolution, Δ is the size of the diffraction-limited PSF, I_{STED} is the intensity of the STED probe beam and I_{sat} is the characteristic saturation intensity of the the probe molecule. STED may be extended for use in 3D-super-resolution microscopy by using a hollow-sphere-, rather than doughnut-shaped STED probe, to generate a resolution enhancement in all three dimensions.

The typical xy-resolution of STED is ~30–80 nm [137–139], and resolution below 10 nm has been reported [140], although this latter case required specialized probes (nano-diamond nitrogen vacancy centres) and has not yet been realized in biological samples. STED requires probes which can undergo stimulated emission, and high laser intensities, to achieve a sizeable resolution increase [18]. An important feature of STED is that, with fast optical scanning of the PSF position, quite high image acquisition speeds can be achieved, particularly for small image areas (up to 60 im-

ages s^{-1}, see Table 5.1), although the raster-scanning nature of the method means that acquisition speed scales poorly with image area. Perhaps the greatest drawback of STED is that its experimental complexity is high [133], primarily due to the need for femtosecond pulsed lasers* for the STED probe beam, and very precise alignment of the excitation optics.

The second form of patterned-illumination microscopy, structured illumination microscopy (SIM [141]) uses (typically sinusoidally) patterned illumination to excite the sample. The effective superposition of the excitation pattern with the sample structure, creating Moiré fringes [65] is essentially a form of interferometry, because the high frequency underlying structure is calculated from the shorter frequency Moiré fringes. Analysis of the fringe pattern produced for different angles of patterned illumination, allows reconstruction of the higher frequency structure (inaccessible due to the diffraction limit) from the low frequency fringes, allowing an improvement in resolution by approximately a factor of two [141].

Two-dimensional SIM is intermediate in complexity between STED and conventional widefield imaging, only requiring the addition of a module to implement the structured illumination pattern to a conventional widefield imaging instrument. Three-dimensional SIM, where the illumination is structured in all three dimensions, is conceptually quite a simple extension to 2D-SIM; in practice, the apparatus required becomes quite complex [142]. Hintzmann and Gustafsson [134] provide an elegant discussion of the theoretical basis of patterned-illumination-based super-resolution microscopy.

"Basic" SIM can be used with any fluorescent probe, but its resolution enhancement is limited to approximately a factor of two (xy-resolution $\sim$ 130 nm [18]). An extension to the method based on saturation fluorescence emission (saturated SIM, SSIM) allows further improvements in resolution [143], but requires very photostable

---

*Although it is possible to use continuous-wave lasers for STED [138], the large reduction in power-density limits spatial resolution and requires very high laser intensity.

probes.

The second class of methods, "localization-based" super-resolution microscopy [13, 133], breaks the diffraction limit by quite different means. If we consider a conventional epifluorescence microscopy image of a two-dimensional sample, the key factor which limits the resolution of the image is the size of the PSFs in the image. Each individual molecule, although perhaps only a few nanometres in size, is observed in the image plane as a PSF with a size of ~ 200 nm due to diffraction. The separation at which two PSFs overlap significantly, and thus cannot be resolved (to first approximation), is called the Rayleigh limit, d_R, and defines the resolution of the image [144]:

$$d_R = \frac{0.61\lambda}{NA}.$$

(5.2)

λ is the wavelength of light, and NA is the numerical aperture of the microscope (between 1–1.5). A fluorescently-labelled structure may contain hundreds of fluorophores within this area, leading to Rayleigh-limited resolution.

Given a perfectly defined PSF, perfect optics, no background noise, and detectors with infinite spatial resolution, diffraction does not actually cause loss of resolution. No information is lost between the object and image plane, so this ideal image could be used to perfectly reconstruct the object. Unfortunately, none of these requirements are well satisfied; in particular, Poisson noise is inherent to fluorescence emission, so it is not possible to obtain a noise-free image. In a limited context, however, this hypothesis remains extremely useful; given an image of a single isolated fluorophore, the PSF model is good enough to localize the position of the fluorophore with resolution much greater than the Rayleigh limit [145, 146]; sub-nanometre resolution has been reported [131]. The theoretical aspects of super-resolution localization of isolated fluorophores are well established [77, 88], and in the absence of background
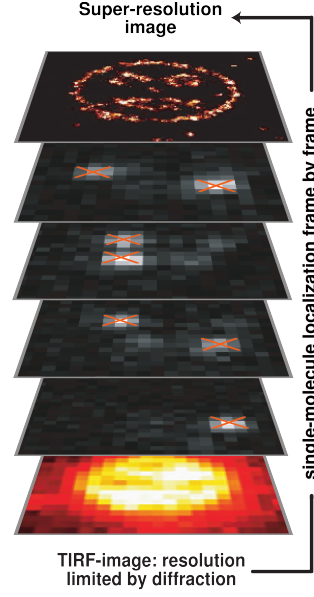
Figure 5.1 *Localization-based super-resolution image reconstruction.* Imaging without photoswitching gives diffraction-limited imaging. Sampling of sparse subsets of molecules via photoswitching allows localization of individual fluorophores and reconstruction of a super-resolved image. Adapted from Ref. 132 with permission.

noise, neglecting pixellation effects, the localization accuracy, σ_x, is given by

$$\sigma_x^2 = \frac{s_x^2}{N},\tag{5.3}$$

where s_x is the PSF width (defined here as the standard deviation of the PSF), and N is the number of photons detected. The details of localization algorithms are discussed in Section 5.3; for the discussion that follows, it is sufficient to assume that there exist estimators capable of the performance predicted by Eq. 5.3 for isolated fluorophores, i.e. for $x_{nn} \gg s_x$, where x_{nn} is the distance of the fluorophore to its nearest (active) neighbour.

Super-resolution localization of isolated fluorophores has yielded many useful insights in the field of particle tracking [108, 146]. However, for conventional epifluorescence data the isolated fluorophore requirement is patently false; at first glance the study of isolated fluorophores seems irrelevant to super-resolution imaging. This

changed with the discovery of fluorophores which could be stochastically switched between a fluorescently active and inactive state [147–149]. If a structure is labelled with such molecules, the majority can be switched to an inactive state so that the small fraction of active molecules are sufficiently spatially isolated for super-resolution localization. Since switching is stochastic, repeated imaging samples different subsets of localized molecules; combination of all localizations gives a reconstructed image (Figure 5.1).

There are several methods for localization-based super-resolution microscopy, including photoactivated localization microscopy (PALM [16]), fluorescence photoactivation localization microscopy (FPALM [150]) and stochastic optical reconstruction microscopy (STORM [14]). PALM and FPALM are essentially simultaneous inventions of the same method, hereafter PALM, in which genetically encoded photoactivatable fluorescent proteins, tagged to proteins of interest are the fluorescent labels used to generate a super-resolved image. Initially most fluorophores are in a dark, inactive state. A subset of fluorophores are activated with UV light, and imaged using visible light until they irreversibly photobleach [16]. This process is repeated until sufficient molecules have been localized to form an image. Localization-based methods can be extended to three-dimensional imaging by measurement of z-position either using known variation of the shape of the PSF with z-position [151, 152], or by interferometry [153].

STORM [14] uses organic fluorophores, usually attached to a target structure via immunolabelling [15], to achieve the same goal. STORM requires labelling of the target molecule with two closely spaced fluorophores; an activator dye (e.g. Cy3) and an imaging dye (e.g. Cy5). Shortly afterwards, a modified version of STORM, called dSTORM, was invented [15], which uses the same approach as STORM but without the need for an activator dye. The key difference between STORM and PALM is that STORM is based on reversible, rather than irreversible photoswitching;

each molecule can switch between the inactive and active state multiple times. For STORM, an activator laser controls the switching rate from the inactive to active state, and an imaging laser is used to excite fluorescence and to control the switching rate from the active to inactive state [15]. The STORM imaging buffer components are very important in determining the switching rates and photobleaching lifetime of the molecules [154–157].

PALM and STORM should be considered as complementary methods. The ability to use genetically encoded fluorophores for PALM is a significant advantage, since it allows very high protein-labelling specificity, and is compatible with live cell imaging [158]. The immunolabelling strategy usually employed for STORM makes live cell imaging much more difficult (particularly for prokaryotes), although alternative labelling strategies show significant promise in this area (trimethoprim conjugates [20], and SNAP tags [159]). However the organic fluorophores used in STORM are significantly brighter that the fluorescent proteins used for PALM, which increases maximum spatial resolution [133]. Dyes can also be used to label a wider range of targets (such as nucleic acids or small molecules), rather than just protein, as for genetically encoded fluorescent proteins.

PALM and STORM generate high spatial resolution images (typical xy-resolution 25–40 nm [18]), but the image acquisition rate of these methods is slow (typically minutes) compared to other super-resolution methods. The factors which limit image acquisition speed, together with strategies to reduce it, are discussed in Chapter 6. The experimental apparatus required for 2D-STORM/ PALM is simple; only a regular widefield/ TIRF instrument with an EMCCD camera is required. Experimental complexity increases for 3D-STORM/ PALM [151–153]. The computational complexity of STORM/ PALM localization algorithms is high, and until recently, software to carry out localization was not readily available; this is changing with the recent release of publicly available software [160, 161].

On comparison of the various super-resolution microscopies, each has its own advantages (see Table 5.1). SIM may be applied for any fluorescent probe, is of only moderate experimental complexity, and has quite high time resolution, but provides only a limited resolution enhancement. STED has high spatial resolution and image acquisition speed, but is experimentally very complex and requires specialized fluorescent probes. STORM/ PALM has similarly high spatial resolution, and is experimentally straightforward, but again requires specialized fluorescent probes, and (currently) has quite low image acquisition speed. A key advantage of STORM and PALM is that they are inherently single-molecule measurements, in contrast to patterned-illumination methods, which assume that the sample under observation is inherently continuous. This fact, which is only beginning to be fully exploited, means that STORM/ PALM is not just an imaging technique, and has much broader potential applications. Initial examples are high-density single particle tracking [17] and analysis of the spatial distribution and clustering of individual proteins in the bacterial cell [162]; I expect that combination with other single-molecule methods, such as single-molecule stoichiometry determination [163] and possibly even combination with smFRET, will prove to be very useful.

5.3   Super-resolution localization algorithms

The super-resolution localization problem is very similar to TIRF-FRET image analysis; i.e., parameter estimation from the image of a molecular PSF, the primary difference being that the parameter of interest is position rather than photon count. Data analysis speed is particularly important for super-resolution localization, since real-time or near real-time imaging is desirable. The performance of the estimator in the presence of overlapping PSFs, i.e., a high surface density of simultaneously active molecules (hereafter imaging density), is also an important consideration since it fundamentally limits acquisition time and spatial resolution; this point will be discussed
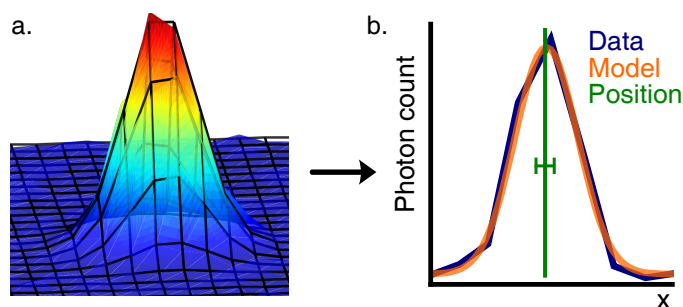
Figure 5.2   *Principle of super-resolution localization. (a)* A small image centred around the observed, isolated, PSF (*colour-map*) is fitted with a model PSF (*wire mesh*). *(b)* The position coordinates correspond to the location of the fluorescent molecule; the uncertainty on the position is much less than the width of the PSF, and is determined by the noise in the image.

in detail in Chapter 6.

As with TIRF-FRET analysis, a very effective parameter estimation method, shown in Figure 5.2, is to fit the data with a 2D Gaussian (Eq. 3.27) via ordinary least-squares minimization (OLS, [14, 16, 67]). This has the advantage that overlapping PSFs may be excluded from fitting using the methods discussed in Chapter 3, i.e. filtering based on eccentricity (shape-based filtering) or PSF width (size-based filtering). This substantially reduces localization error due to overlapping PSFs (see Chapter 6).

Although OLS is unbiased and quite accurate, it is not a minimum variance estimator; instead it introduces $\sim 30\ \%$ excess localization error into the results [77, 88]. This is because OLS assumes uniform noise across an image, whereas in fact the noise varies significantly because fluorescence emission obeys Poisson statistics. A promising alternative to this approach is fitting via maximum likelihood estimation (MLE), which has been shown to achieve minimum variance performance [88, 161, 164] by explicitly incorporating an accurate noise model into the fit. A disadvantage of OLS or MLE methods is that their computational complexity makes real-time analysis non-trivial, although several real-time implementations have been reported [67, 161, 164], some of which use parallel-processing schemes to achieve this goal [161, 164].

Two alternative methods have been proposed, which have poorer localization accuracy but are much faster. The centre of mass estimator [81, 160] calculates the centre of mass of a small sub-image centred around the PSF. This method is sufficiently fast to allow real-time analysis, but gives poor performance in the presence of background noise [88]. The fluoroBancroft estimator [165, 166] is an algebraic algorithm adapted from position estimation for Global Positioning System (GPS) devices, which is reported to achieve performance almost as good as OLS, but with significantly increased speed ($\sim$ 10–100$\times$ faster [166]). Currently, neither the centre of mass or fluoroBancroft algorithms permit shape/size-based filtering to exclude overlapping PSFs; therefore I expect their localization accuracy at high imaging density to be poor.

Another super-resolution imaging approach, super-resolution optical fluctuation imaging (SOFI [167, 168]) uses a correlation-based, rather than localization-based, approach. Essentially, the autocorrelation function of the fluctuations around the mean value for each individual pixel is calculated across multiple frames. Large fluctuations due to the presence of a photoswitching molecule give high correlation, and small fluctuations in the absence of photoswitching give low correlation. A simple (but lower-resolution) approximation of the method is to calculate the variance over all frames of the image. Sub-pixel resolution may be achieved by calculating the cross-correlation function between adjacent pixels [168].

It can be shown [167] that SOFI produces sub-diffraction-limit resolution enhancement; the precise degree of resolution enhancement is not a straightforward function of photon count or laser intensity, but instead depends on the maximum usable cumulant order n of the correlation function, as $\sqrt{n}$. The cumulant order is effectively the time-lag of the correlation function, i.e., the number of frames used to calculate the correlation function; the maximum useful value of n depends on the length of the data series, the noise in the image, the magnitude of brightness fluctuations, and the

temporally averaged brightness differences across the image [167]. Further work is required to precisely define the SOFI resolution enhancement in terms of these key image parameters. Since the approach does not require isolated PSFs, it is likely that it performs quite well at high imaging density. The disadvantage of SOFI is that the sample is assumed to be entirely immobile during the image acquisition process; this will make study of live cell dynamics [20] difficult, particularly for applications which combine super-resolution imaging with single particle tracking [17].

CHAPTER 6

High-density super-resolution localization

6.1 Introduction

Optical microscopy is currently undergoing dramatic changes due to localization-based super-resolution microscopies such as STORM [14] and PALM [16], which use stochastic photoswitching to resolve closely spaced fluorophores and reconstruct "super-resolved" images with sub-diffraction limit resolution. Although these methods have the potential to significantly impact cell biology, they are currently limited by the requirement for their biological specimen to have a density of active fluorophores (hereafter "imaging density") lower than 1 molecule/ μm^2. A major cause of this limitation is that current super-resolution localization algorithms extract the position of fluorescent molecules by fitting images using only a single model point spread function (PSF; the diffraction-limited far-field image of an individual fluorophore). This limits the maximum achievable spatial resolution (see Section 6.2) and leads to long image-acquisition times (typically seconds to minutes [19, 20]), thwarting studies of dynamics in living cells.

By adapting techniques originally developed by astronomers to analyse images of crowded stellar fields (DAOPHOT II [89, 169]), I developed DAOSTORM, an

algorithm for analysis of high imaging density super-resolution data (up to 10 molecules/ μm^2). The DAOPHOT II algorithm [169] (applied only once previously to single-molecule fluorescence data [21]) identifies molecular PSFs (hereafter "molecules") which overlap significantly, and simultaneously fits overlapping molecules with multiple model PSFs, instead of just one. This advance allows successful analysis of high imaging density data. DAOSTORM (described in Section 6.3.3) adapts DAOPHOT II for super-resolution imaging by increasing its automation and robustness.

DAOSTORM was compared to two common localization algorithms. "Sparse Algorithm 1" (SA1) [14] fits candidate molecules with a single elliptical Gaussian PSF of variable size and ellipticity. Localizations arising from multiple overlapping molecules are rejected if the fitted PSF appears too elliptical ("shape-based filtering"), or if the observed PSF width is too large or small ("size-based filtering"). "Sparse Algorithm 2" (SA2) [67] fits candidate molecules with a single Gaussian PSF of fixed shape and size, without shape/ size-based filtering.

In this chapter, I first provide brief theoretical description of some of the limiting factors for spatial resolution and acquisition time. I then describe the DAOSTORM algorithm, together with existing approaches. I describe simulations and experiments to quantify the relative performance of each of the algorithms, demonstrating that DAOSTORM shows significant advantages compared with existing algorithms. Finally, I discuss some considerations regarding performance of the DAOSTORM algorithm in the context of recent literature.

Super-resolution imaging of fluorescently-labelled microtubules was performed together with Stephan Uphoff; all other work was carried out independently. The work presented in this chapter has recently been published as Ref. 170.

6.2 Theory

6.2.1 Factors determining spatial resolution

The primary consideration for accurate localization of a single, isolated fluorophore is the SNR of the measurement [88]. However, if super-resolution methods are applied to the imaging of extended structures, rather than isolated points, a key consideration is the size of the image sampling interval, i.e., the density of fluorescent labels on the structure [158, 171]. The Nyquist-Shannon sampling theorem states that the spatial resolution, Δx_{min}, is twice the image sampling interval [171]. Assuming uniform two-dimensional labelling density, ρ_l, and high SNR, then:

$$\Delta x_{min} = \frac{2}{\sqrt{\rho_l}}. \qquad (6.1)$$

The average imaging density, ρ_i, and labelling density are related by:

$$\rho_i = \rho_l/r, \qquad (6.2)$$

where r is the rate-ratio,

$$r = \tau_{off}/\tau_{on}, \qquad (6.3)$$

The rate-ratio [172] describes the ratio of fluorophores in the dark, inactive, state to those in the active state, and is determined by the mean lifetimes of the inactive and active states, τ_{off} and τ_{on}, respectively.

Therefore, assuming that the labelling density may be chosen arbitrarily (i.e., that it is not limited by factors such as the size of the labels, which may become important at very high ρ_l [173]), the spatial resolution is determined by the rate-ratio and the imaging density,

$$\Delta x_{min} = \frac{2}{\sqrt{r\rho_i}}. \qquad (6.4)$$

This result shows that there are two main ways to increase the maximum spatial resolution: either the rate-ratio or the imaging density should be increased. Since maximum off-on ratio is currently limited to about 100-1000 by experimental factors such as fluorophore and imaging buffer properties [172], I conclude that a high maximum imaging density, largely determined by localization algorithm performance, is a significant factor for maximum spatial resolution.

6.2.2   Factors determining acquisition time

Assuming that the time required for collecting photons is not a limiting factor (i.e., in the limit of high photon counts), the time required to acquire a super-resolved image may be estimated by considering an ensemble of molecules, all initially in their dark state, which can switch reversibly to the bright state at rate τ_{off}^{-1}. The rate of transition from the bright state to the dark state is τ_{on}^{-1}. The probability that a molecule has switched on at least once, irrespective of further switching on or off, P_{on}, is determined by:

$$\frac{\mathrm{d}P_{on}}{\mathrm{d}t} = \tau_{off}^{-1}(1 - P_{on}). \tag{6.5}$$

Integrating and using the boundary conditions $P_{on}(t = 0) = 0$, and $P_{on}(t \to \infty) \to 1$, yields

$$P_{on} = 1 - \exp\left(-t/\tau_{off}\right). \tag{6.6}$$

This allows us to predict the average acquisition time, t_{aq}, required to image a given fraction, α, of the molecules present in a sample:

$$t_{aq} = \tau_{off} \ln\left\{(1 - \alpha)^{-1}\right\}. \tag{6.7}$$

However, this result is not very instructive since it simply suggests that we should choose $\tau_{off} = 0$ for fast imaging, i.e., that non-photoswitching molecules should be used! To formulate this result more usefully, I use Eqs. 6.2, 6.3 to obtain $\tau_{off} =$

$\tau_{on}\rho_l/\rho_i$. This yields:

$$t_{aq} = \frac{\tau_{on}\rho_l}{\rho_i} \ln\left\{(1-\alpha)^{-1}\right\}. \tag{6.8}$$

Therefore, acquisition time is minimized by decreasing τ_{on} (faster photoswitching), decreasing either α or ρ_l (reduced labelling density), or by increasing ρ_i (higher imaging density).

I conclude that the maximum useable imaging density of given super-resolution localization algorithm is a crucial factor for both acquisition time and maximum spatial resolution.

6.3   Materials and Methods

6.3.1   STORM imaging of COS-7 microtubules

COS-7 cells were plated onto LabTek 8-well chambered cover-glass (Nunc) and grown for 12 hours. Cells were fixed with a solution of 4 % paraformaldehyde and 250 mM HEPES-NaOH pH 7.8 for 15 min, washed three times and stored in PBS at 4°C. Cells were incubated with mouse monoclonal anti-beta-tubulin (Sigma T9026) for 30 min, followed by washing three times with PBS. Secondary antibody (goat anti-mouse F(ab')2 fragment labelled with Alexa647, Invitrogen A-21237) was incubated for 30 min, and washed three times with PBS. Before imaging, the PBS storage solution was replaced by imaging buffer containing PBS, 50 mM β-mercaptoethylamine (MEA), 10 % w/ v glucose, 1 mg/ ml glucose oxidase, and 40 μg/ ml catalase (dSTORM imaging conditions [15]). The sample chamber was sealed from air with a microscope cover-slide after addition of the imaging buffer.

Total internal reflection fluorescence (TIRF) imaging of the sample was performed using apparatus described in Chapter 4. Briefly, the sample was continuously illuminated with a green laser (532 nm) at 100 μW and a red laser (635 nm) at 4 mW. The green and red laser beams were coupled into the same single-mode optical fibre. At

the fibre output, the laser beams were collimated, directed into an inverted microscope (IX71, Olympus) and focused ($100\times$ oil-immersion objective, NA 1.4, Olympus) onto the sample at an angle allowing for total internal reflection. The fluorescence emission was collected by the same objective, separated from excitation light by a dichroic mirror (545 nm/ 650 nm, Semrock) and additional filters (545 nm LP, Chroma; and 633 nm/ 25 nm notch filter, Semrock, 630 nm DRLP; Omega). Fluorescence emission was imaged using an EMCCD camera (iXon DU-897, Andor). The pixel size was measured as 94 nm using a 10 μm stage micrometer. The 1-sigma PSF width for Alexa647 measured as $\sim$ 165 nm. A series of 2000 frames was recorded at an integration time of 100 ms. A mean photon count of 4000 photons per molecule/ frame was observed.

6.3.2 Sparse super-resolution localization algorithms

Detection of candidate molecular point spread functions (PSFs) in the data, "peak-finding", was carried out as described below, followed by use of one of the sparse localization algorithms to generate super-resolved localizations.

6.3.2.1 Peak-finding

For a fair comparison of the algorithms, I used the same peak-finding algorithm to calculate initial localizations for each algorithm. I used the "DAOFIND" routine from DAOPHOT II [89, 169], which is mathematically closely related to Thompson's Gaussian Mask Estimator (GME) [77, 88], but is calculated with only single-pixel, rather than sub-pixel resolution.

DAOFIND proceeds by convolution of a truncated circular symmetric Gaussian kernel with the input image [89]. Given a user-specified estimate of the background noise standard deviation b (photons/ pixel), local maxima in the convolved image are identified at a threshold of nb above the local background, where n is a user

set parameter. For the high signal-to-noise ratio (SNR) simulations (5000 photons per molecule/ frame in the PSF core*, b=3.2 photons/ pixel, SNR $= 50$) and experimental data (4000 detected photons per molecule/ frame, $b \sim 6.5$ photons/ pixel, SNR ~ 40), a threshold of $n = 15$ was chosen. For the low SNR data (200 photons per molecule/ frame in the PSF core, b=3.2 photons/ pixel, SNR $= 8$), a threshold of $n = 4$ was chosen.

I observed that thresholds below $n = 4$ led to a large number of false localizations. For the experimental data, a value of $b = 6.5$ photons/ pixel was used (approximately matching the experimentally observed background noise level). For simulations a value of $b = 3.2$ photons/ pixel was used.

6.3.2.2   Sparse algorithm 1

Sparse Algorithm 1 (SA1) is based upon the approach described by Rust et al. [14]. Small sub-images were formed by choosing a 7×7 pixel window centred on the initial localization position. The data were then fitted with an elliptical Gaussian model [14] (as in Chapter 3, repeated here for clarity),

$$N_{ij} = \frac{N}{2\pi s_x s_y} \exp\left(\frac{x'^2}{2s_x^2} + \frac{y'^2}{2s_y^2}\right) + B. \tag{6.9}$$

N_{ij} and N indicate the expected photon count for a single pixel and for the entire PSF, respectively; and B is the expected background level. y' and x' are the pixel coordinates in the coordinate system aligned to the major axis, $y' = (i - x_0)sin\theta + (j - y_0)cos\theta$, and minor axis, $x' = (i - x_0)cos\theta - (j - y_0)sin\theta$, of observed elliptical PSF. (x_0, y_0) is the expected position of the molecule, (i, j) are the pixel coordinates and θ is the angle between the (i, j) and (x', y') coordinate systems. s_y and s_x are

---

*The PSF core is defined as the region where the photon count estimated from the best-fitting Gaussian model PSF is non-negligible, as opposed to the full photon count for a freely-rotating dipole model PSF, which contains ~ 65 % more photons in an extended, low-amplitude tail; see Section 6.3.5 and Ref. 88.

the PSF widths along each elliptical axis.

Fitting was carried out via ordinary least-squares minimization as previously described [80], with all fit parameters left free to vary. Data arising from multiple overlapping molecules were excluded using shape/ size-based filtering [14, 80, 174]. Data were filtered based on the fitted PSF width, and on the eccentricity

$$\varepsilon = \sqrt{1 - \frac{s_y^2}{s_x^2}}, \tag{6.10}$$

For simulations (see Section 6.3.5), where the best fitted Gaussian PSF gave $s_x \sim s_y$=1.33 pixels, all molecules with $\min(s_y, s_x) < 1.0$ pixels, $\max(s_y, s_x) > 1.7$ pixels or $\varepsilon > 0.6$ were excluded from analysis. For experimental results, where $s_x \sim s_y \sim 1.75$ was observed, all molecules with $\min(s_y, s_x) < 1.0$ pixels, $\max(s_y, s_x) > 2.5$ pixels, or $\varepsilon > 0.6$ were excluded from analysis.

Molecules whose final localization position differed from the initial position estimate by greater than 1.5 pixels were rejected, in order to minimize the effects of bright molecules on fitting of adjacent dimmer molecules.

6.3.2.3   Sparse algorithm 2

Sparse Algorithm 2 (SA2) is based upon the approach described by Wolter et al. [67]. The same method as for SA1 was used, except that s_x, s_y and θ were set as fixed parameters in the fit, chosen based on the best-fitting model PSF obtained using SA1 on isolated molecules. For simulations, s_x and s_y were set to 1.33 pixels, and for experimental results, s_x and s_y were set to 1.75 pixels.

Shape/ size-based filtering was not performed for SA2, instead only molecules whose final position was greater than 1.5 pixels distant from the initial localization were excluded. Unlike SA1, SA2 does not allow filtering of overlapping molecules; if multiple molecules are fitted with a single model PSF by SA2, the observed localiza-

tion will be the averaged position of all the molecules.

6.3.3 Super-resolution localization using DAOSTORM

The DAOSTORM algorithm adapts the DAOPHOT II algorithm (which has previously been described in detail [89, 169]) to make it suitable for super-resolution localization. I discuss the theoretical principles behind the DAOPHOT II algorithm, followed by a description of how the model PSF is calculated, and a description of the DAOSTORM algorithm.

6.3.3.1 Principles behind the DAOPHOT II algorithm

The theoretically optimal method of localizing multiple molecules in a high density image is global minimization of a fit of all model PSFs to the whole image. However, for M molecules, the run time of this process scales as order of M^3 [89], which would lead to very slow fitting even for relatively small M. However, for the case of stochastic photoswitching, it is exceedingly unlikely that all molecules in an image overlap to such a degree that this approach is required. Instead, molecules may be split up into ν (approximately) statistically independent non-overlapping groups, each containing several overlapping molecules. These groups may then be fitted independently of each other. The number of groups, ν, is approximately M/n, where n is the mean number of overlapping molecules per group. It can be shown [89] that the run time of this algorithm scales as order of M^3/ν^2, which approximates to Mn^2. This approach, adopted by DAOPHOT II, is far more computationally efficient than full global minimization, with little loss of precision. Molecules are split up into independent groups based on the spatial separation at which the brightness contribution of a molecule is less than the observed background noise [89].

Some considerations regarding the DAOSTORM minimization algorithm in the context of recent literature are discussed in Section 6.4.1.

6.3.3.2   Estimation of a model PSF

Before fitting, a model PSF is required; DAOPHOT II estimates an empirical model PSF directly from isolated molecules within the data [89]. A model PSF with fixed shape and size is used, which simplifies the fitting problem, since the only free parameters are the PSF positions and amplitudes (the local background is estimated directly [89]).

For the original application of DAOPHOT II, i.e., measurement of absolute photon counts in astronomy, it was recommended that isolated PSFs should be *manually* identified for each frame of the data. This is clearly an impractical undertaking for the thousands of frames that comprise even a single super-resolution data series. It was found that for accurate estimation of position, an automatically-derived model PSF from a single frame of an experimental dataset could be used for all frames of a data series, even in the presence of small amounts of focal drift (a few hundred nanometres) without significant increase in the localization error. Additionally, it was found that the same model PSF could be used for different datasets from the same instrument, again without significant increase in the localization error.

I therefore chose the following approach: a model PSF is automatically generated from low or moderate imaging density data using the DAOSTORM "generatePSF" algorithm. Briefly, this algorithm proceeds by identifying a number of bright molecules within a single image, which are then used to generate an initial model PSF. Localization of the molecules in the image using the methods described below is carried out. All identified molecules are then subtracted from the image except the selected bright molecules, leaving an image containing only the molecules intended for PSF generation. These molecules are then used to generate a more accurate model PSF. This algorithm is iterated four times to produce an accurate model PSF, even in the presence of significant molecular overlap. For all in-focus measurements on the same instrument (with the same filter set, excitation/ emission wavelengths, and flu-

orophores), this model PSF is used. Should it be necessary to generate a model PSF for an individual data series, this is straightforward even for high imaging density data.

6.3.3.3   The DAOSTORM algorithm

Once a model PSF has been generated, the DAOSTORM algorithm may be applied to the data. A schematic diagram of the DAOSTORM algorithm is shown in Figure 6.1. For a single frame of a data series, after obtaining a set of initial localizations (Figure 6.1, step 1), the DAOPHOT II "ALLSTAR" routine is used to automatically group overlapping molecules, and to fit each group with multiple model PSFs simultaneously (Figure 6.1, step 2). After several iterations, ALLSTAR checks whether PSFs have migrated to form new groups. ALLSTAR also checks whether two localizations have converged below a minimum critical separation, 0.4 times the PSF full-width at half-maximum (FWHM). If this is the case, the number of model PSFs in the group is reduced by one to prevent the fitting of multiple low-amplitude PSFs to the same position. The fitting error is also periodically checked: if the fitting error for a particular molecule is very large (a symptom of spurious molecules in the fit), that molecule is deleted [172]; for example, in Figure 6.1, step 2, note the deletion of the dim molecule in group A, adjacent to a much brighter molecule. At this stage of the algorithm, the characteristic averaging of the positions of overlapping PSFs may still be observed (Figure 6.1, step 2, groups A and B).

After the initial round of fitting, a residuals image is calculated (Figure 6.1, step 3) containing PSFs which were not identified during the initial localization step, together with a list of localizations from the first ALLSTAR iteration. Peak-finding is carried out on the residuals image and the list of newly identified molecules is added to the list of localizations from the first iteration.

ALLSTAR is re-run on the original image using the updated list of localizations
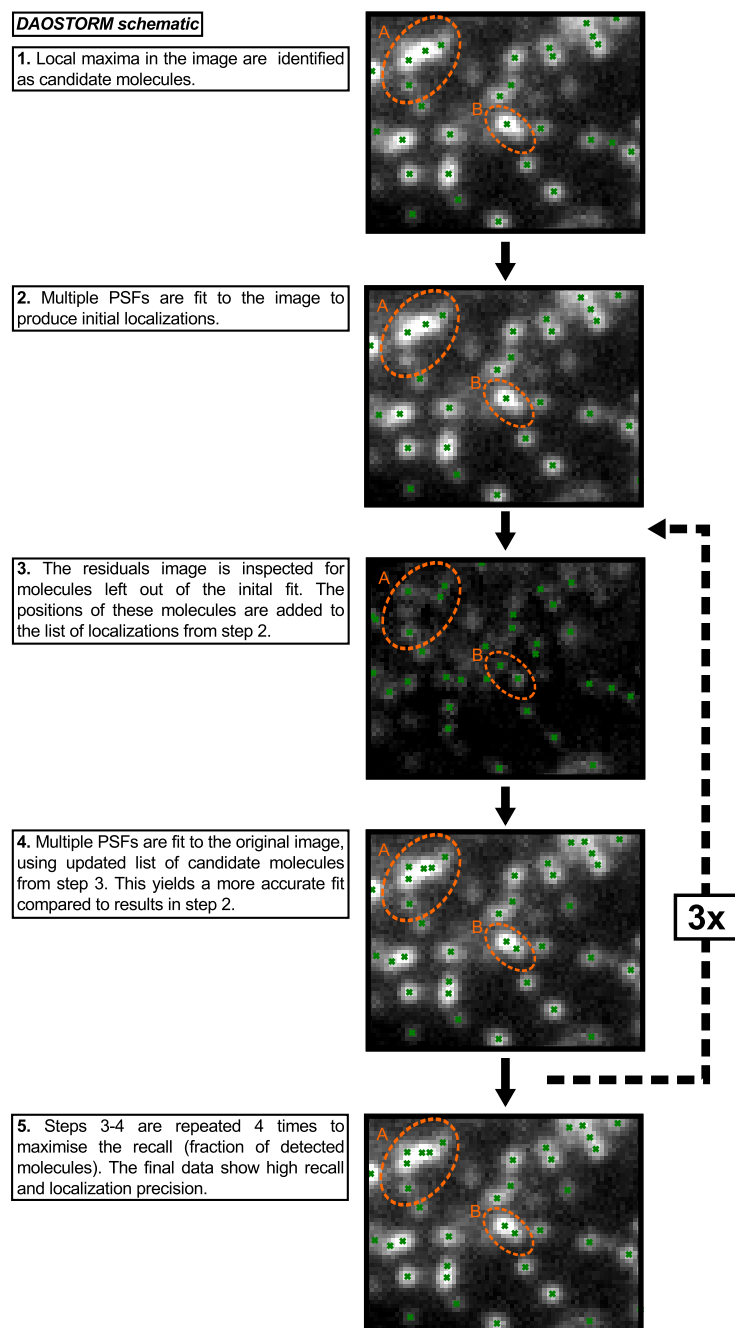
DAOSTORM schematic

1. Local maxima in the image are identified as candidate molecules.

2. Multiple PSFs are fit to the image to produce initial localizations.

3. The residuals image is inspected for molecules left out of the inital fit. The positions of these molecules are added to the list of localizations from step 2.

4. Multiple PSFs are fit to the original image, using updated list of candidate molecules from step 3. This yields a more accurate fit compared to results in step 2.

5. Steps 3-4 are repeated 4 times to maximise the recall (fraction of detected molecules). The final data show high recall and localization precision.

3x

Figure 6.1   *Schematic illustration of the DAOSTORM algorithm.*   For a detailed description of algorithm, see Supplementary Methods.   Circled areas A-B identify regions showing typical behaviour of DAOSTORM in the presence of overlapping molecules.

(Figure 6.1, step 3). The addition of the extra molecules identified from the residuals image allows accurate fitting of multiple overlapping PSFs (Figure 6.1, step 2, groups A and B). This process may be repeated until no above-threshold molecules are found in the residuals image; 4 iterations of this routine were found to be sufficient to produce accurate results at acceptable speed (100 localizations per second on a single 2.4 GHz CPU). DAOSTORM automates all steps in the above process (which would otherwise have to be manually performed with DAOPHOT II), and performs it for all frames of a data series.

DAOSTORM is written in Python, using the pyRAF [175] interface to the astronomy software package IRAF [176], which contains DAOPHOT II. IRAF and DAOPHOT II are largely written in FORTRAN.

6.3.4   Super-resolution data visualization

Data were visualized by producing a two-dimensional histogram of all localizations at five times the resolution of the original image, giving a pixel size of 19 nm. For display purposes, all images were separately normalized, and the image contrast adjusted such that the brightest and dimmest 1 % of all pixels were saturated. The line plots in Figures 6.2, 6.5 and the histogram in Figure 6.4 show 1D histograms of localizations along an interpolated rectangle of width of 2 pixels (38 nm). Data visualization was carried out using MATLAB (Mathworks, USA) and ImageJ (NIH, USA).

6.3.5   Simulations

Monte Carlo simulations were carried out for multiple randomly distributed surface-immobilized molecules with uniform mean intensity. Simulations were essentially identical to those described previously [80], except that I updated the fluorophore model PSF in light of recent work [88]. Instead of a Gaussian model PSF, the theoretical PSF of a freely rotating surface immobilized dipole under circularly polarized

TIRF illumination was used. The fluorophores were modelled as emitting photons with wavelength 668 nm, corresponding to the emission maximum of Alexa647. Simulations included photon shot-noise, electron-multiplying gain noise and a general Gaussian background noise term, b, chosen as 3.2 photons/ pixel. The gain U (digital units per photon) was chosen to match the value for the camera, $U = 3.1$. Simulations were carried out over the area of a 256×256 pixel grid, with a pixel size of 94 nm. For these parameters, the freely rotating dipole PSF was well fitted by a 2D Gaussian PSF with $s_x = s_y = 1.33$ pixels.

It was shown in Ref. 88 that for the model PSF used, only ~ 60 % of the photons are contained in the PSF core, defined here as the region where the photon count estimated from a best-fitting Gaussian model PSF is non-negligible, as opposed to the full photon count from the freely-rotating dipole model PSF. The additional photons are contained in an extended, low-amplitude, power-law tail [88]. The experimental photon count per molecule per frame, N, is estimated via a Gaussian fit to the PSF. Therefore, to carry out simulations of similar data, a model PSF with a *total* photon count of $N/0.6$ should be used. For high SNR simulations with 5000 photons per molecule/ frame in the PSF core, a total photon count of 8333 was used. For low SNR simulations with 200 photons per molecule/ frame in the PSF core, a total photon count of 333 was used.

Super-resolution localization algorithms SA1, SA2, and DAOSTORM were applied to the simulated data, yielding sets of observed localizations and simulated molecule positions for each simulated image. I analysed the relationship between the sets of observed and simulated molecules based on the approach of Wolter et al. [67]. For each observed localization, the nearest simulated molecule within a radius of 3 PSF widths was searched for. If a simulated molecule was found within this radius, the observed localization was counted as valid, otherwise it was counted as a false positive. This process was repeated for all observed molecules in an image.

The recall, precision, localization error, and redundancy were calculated. The recall [67] is defined as the number of simulated molecules successfully detected divided by the total number of simulated molecules, i.e., the fraction of molecules successfully identified. The precision [67] is the number of valid localizations divided by the total number of observed molecules, i.e., the fraction of observations which were valid. The localization error is the root mean square distance between valid localizations and the actual position of the simulated molecules. I introduced a new metric, redundancy, defined as the number of "excess" localizations (i.e., where the same simulated molecule is detected multiple times) divided by the number of simulated molecules successfully detected.

For simplicity, the detection threshold was set sufficiently high such that the precision was always close to 100 %, even though this led to a reduction in the maximum recall for simulations at low SNR. The only exception to this is for low SNR simulations with SA2; at very low imaging density (< 10 molecules/ μm^2), SA2 precision is reduced to 80–90 %. For all simulations, the redundancy was uniformly close to 0 % for SA1 and DAOSTORM, while SA2 showed redundancy of up to 17 % at low SNR, and up to 8 % at high SNR for densities greater than 1 molecule/ μm^2.

Simulations were repeated 10 times at each imaging density and analysed separately to generate error estimates; error bars and the $\pm$ sign indicate one standard deviation.

6.3.6   Note on the DAOSTORM software

The DAOSTORM software will be made available to the community on publication of the associated manuscript [170]. DAOSTORM has been tested on Ubuntu Linux 10.04 (for 32- and 64-bit versions of the operating system), and should run on any UNIX-based operating system.

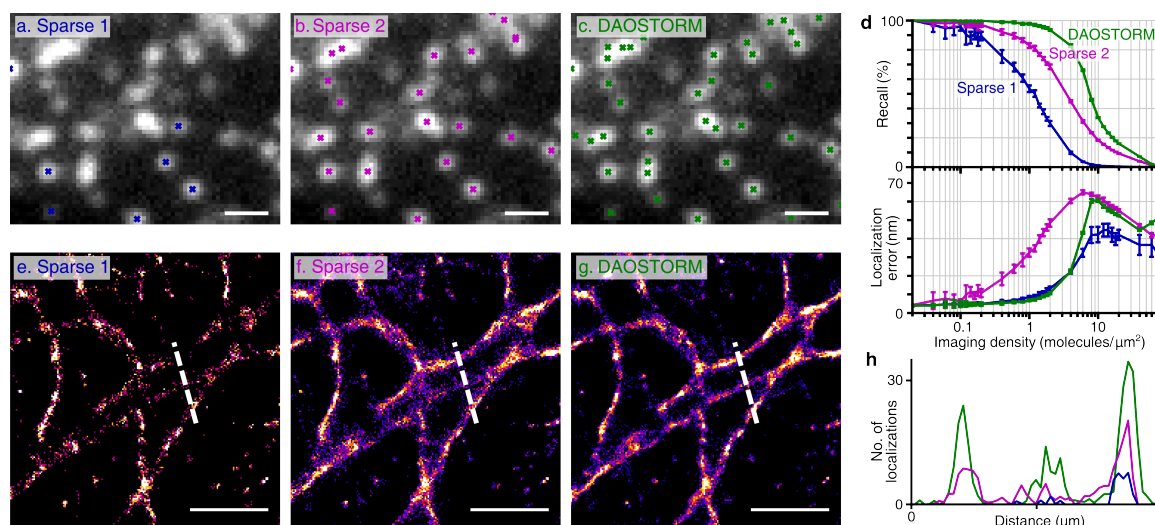I note that the current speed of DAOSTORM (100 localizations per second on a

Figure 6.2   *Comparison of DAOSTORM to existing super-resolution localization algorithms. (a-c)* Visual comparison of algorithms on a single dSTORM image. Each algorithm was applied to a single image of fixed COS-7 cells with Alexa647-stained microtubules under dSTORM photoswitching conditions. Crosses represent localizations for each algorithm. *(d)* Simulations of randomly distributed surface-immobilized molecules quantify localization performance. The density of surface-immobilized molecules (imaging density) was varied and the recall (the fraction of simulated molecules detected correctly) and localization error were calculated. Error bars indicate 1 s. d. *(e-g)* Super-resolution reconstruction of 2000-frame series recorded in a separate region of the sample of Alexa647-stained microtubules in a-c. The fluorescence average is also provided (Figure 6.3). *(h)* Line plot of region indicated by dashed line in a-c. Scale bars, 1 μm.

single 2.4 GHz CPU, see Section 6.3.3) prohibits real-time analysis during acquisition. Although future development of DAOSTORM may resolve this issue (e.g., using a parallelized GPU-processing-based approach [161]), I currently suggest the following analysis protocol for high imaging density data: an initial real-time analysis should be performed alongside data acquisition using a less accurate but faster algorithm [160, 161], followed by post-acquisition analysis using DAOSTORM to maximize recall and localization performance.

6.4   Results and discussion

I first investigated the qualitative performance of each algorithm on single images of Alexa647-labelled microtubules in fixed COS-7 cells (Figure 6.2a-c). Data were
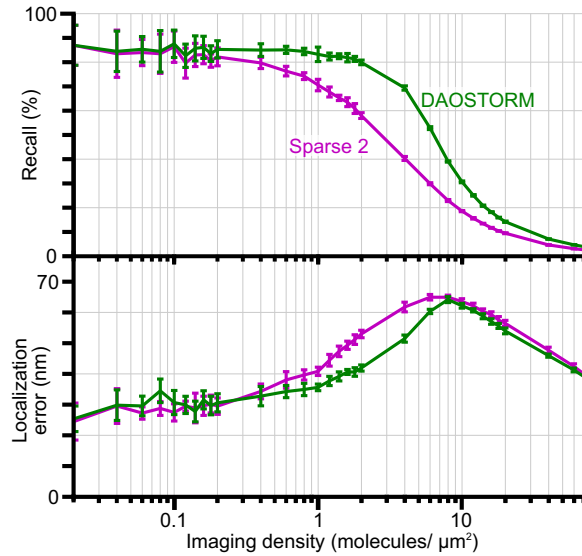
Figure 6.3 *Low SNR ("PALM-like") simulations of randomly distributed surface-immobilized molecules quantify performance of each algorithm.* The density of surface-immobilized molecules (imaging density) was varied, and the recall (the fraction of simulated molecules correctly detected) and localization error were measured. SA1 does not work at low SNR because the shape/ size-based filtering metrics fail in this regime (i.e., nearly all observed PSFs are erroneously rejected). DAOSTORM gives a $2\times$ performance increase in half-maximum recall density, ρ_{HM}, (at 33 % recall) compared with SA2, whilst retaining small localization error. 200 photons per molecule/ frame in PSF core; background noise, 3.2 photons per pixel/ frame.

recorded at high imaging density in total internal reflection fluorescence (TIRF) mode under dSTORM photoswitching conditions [15] (100 ms integration time per frame, mean photon detection rate, 4000 photons per fluorophore per frame). A plot of identified localizations on the raw image (crosses in Figure 6.2a-c) demonstrates the characteristic performance of each algorithm. SA1 identified only isolated molecules in the image, which were fitted with small localization error. SA2 identified a much larger fraction of the molecules, but showed large localization error in the presence of overlapping molecules. DAOSTORM outperformed both sparse algorithms by successfully identifying almost all visible molecules with small localization error, even in the presence of significant molecular overlap.

The performance of each algorithm was quantified by applying them to simulations of randomly distributed surface-immobilized fluorophores [80] using the theoretical
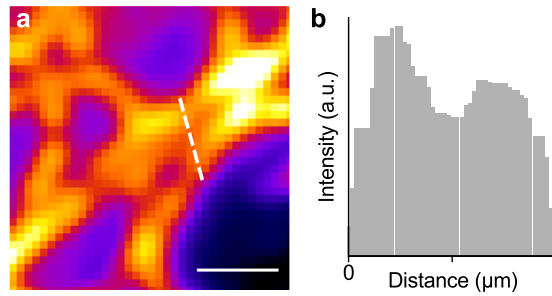
Figure 6.4   *Fluorescence average of raw images for data shown in Figure 1e-h. (a)* Averaged image of dSTORM movie. *(b)* 1D histogram of region in *a* indicated by dashed line. Scale bar, 1 μm

PSF of a freely rotating surface-immobilized dipole [88]. Simulations of high signal-to-noise ratio (SNR) data typical of STORM images (bright organic fluorophores, 5000 photons per molecule per frame in the PSF core) showed that DAOSTORM significantly outperformed the sparse algorithms (Figure 6.2d). SA1 showed a rapid decrease in recall (defined in Section 6.3.5) with increasing imaging density, with an imaging density at half-maximum recall, ρ_{HM} of 1.2 molecules/ μm². However, SA1 showed small localization errors even at high imaging density, since most overlapping molecules were excluded from analysis. SA2 showed a slower decrease in recall with increasing density ($\rho_{HM} = 3.4$ molecules/ μm²) but gave large localization errors even at low imaging density (> 0.1 molecules/ μm²). In contrast, DAOSTORM showed high recall even at very high imaging density, and gave small localization errors similar to the other "precise" algorithm SA1; crucially, its ρ_{HM} of 7.5 molecules/ μm² was 6-fold higher than SA1. DAOSTORM also gave a 2-fold increase in ρ_{HM} for simulations at low SNR values typical of PALM images (fluorescent proteins, 200 photons per molecule per frame in the PSF core; Figure 6.4).

I also examined the *precision* [67] and *redundancy* performance for the simulations, but these did not vary significantly between the algorithms (see Section 6.3.5).

Next, 2000 dSTORM images of the microtubule network described above were recorded, and each algorithm was applied to obtain super-resolved images (Fig-
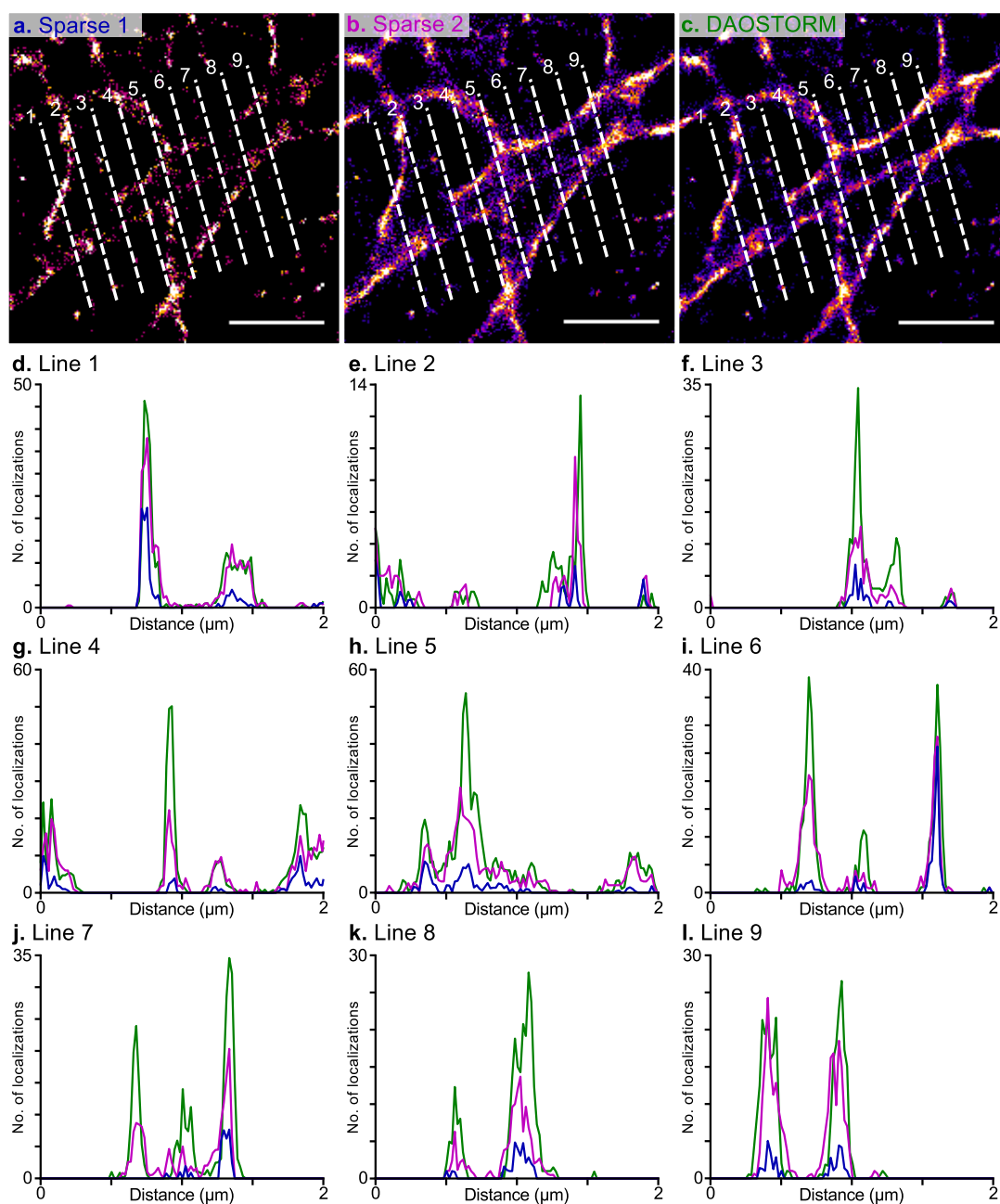
Figure 6.5 *Line plots at a range of positions for data shown in Figure 1e-h.* Blue line: results for SA1. Magenta line: results for SA2. Green Line: results for DAOSTORM. DAOSTORM shows improved recall (with DAOSTORM, microtubules have larger amplitude and new features are detected in the image) and reduced localization errors (with DAOSTORM, FWHM of microtubules is smaller and image is less noisy). Scale bars, 1 μm.

ure 6.2e-g). SA1 showed low recall, producing poorly sampled STORM images, while SA2 achieved higher recall, but with large localization error, leading to a poorly-defined, noisy images. DAOSTORM showed the highest recall and smallest localization error, producing well-defined, low-noise images of the microtubule network. A line-plot across three parallel microtubules demonstrates the performance difference among the algorithms (Figure 6.2h): DAOSTORM resolved all three microtubules, SA2 detected two and SA1 detected only one. A series of 9 line-plots across the images (Figure 6.5) further illustrates the relative performance of the algorithms.

These results clearly demonstrate the ability of DAOSTORM to provide a more quantitative report on the spatial distribution of fluorescent molecules, to increase the quality of super-resolved images of biological samples, and to maintain performance at high imaging density.

6.4.1   Considerations regarding the fitting algorithm

Recently, Mortensen et al. [88] carried out a detailed investigation into methods for localizing isolated fluorophores in the presence of uniform background noise. For freely rotating fluorophores, maximum likelihood estimation (MLE) using a Gaussian PSF was found to be superior to Gaussian Mask estimator (GME) methods [77, 88], which gave 30 % excess localization error compared to MLE.

SA1 and SA2 represent variations on the GME, and were expected to give GME localization errors. DAOPHOT II uses a modified form of MLE (although Ref. [89] calls it least-squares fitting, inspection of the DAOPHOT II source code confirms that MLE is used). As with standard MLE, least-squares fitting is carried out, with each pixel weighted with the expected photon count from the fitting model. However, several further ad-hoc weighting components are also included [89], including a radial weighting term based on the distance of each pixel from the PSF centroids, and a term which reduces the weight of individual outlier pixels. These weighting

components have been shown previously to be crucial in giving robust and rapid fits
in high-density images, and in the presence of outliers [89]. These considerations are
particularly relevant for super-resolution images of cellular structures. Even without
considering the effect of overlapping molecules, the presence of dimly fluorescent in-
active molecules, out-of-focus active molecules, and cellular autofluorescence will all
create "outliers" from a uniform background plus Gaussian model. The excess noise
introduced by an EMCCD camera is not currently included in the weighting scheme.
It is not obvious a priori whether these factors increase the DAOPHOT II localization
error above the theoretically optimal level for an MLE.

To investigate whether DAOPHOT attained unmodified-MLE localization per-
formance, I compared the observed localization error for simulations at low imaging
density with the predicted theoretical limits [88]. For the high SNR simulations,
(Figure 6.2, 8333 photons per molecule in the entire PSF, localization prediction as-
sumes 5000 photons in PSF core), the predicted localization error is 2.1 nm for MLE
and 3.7 nm for GME. At low imaging density, observed localization error for DAO-
STORM is 3.9 ± 0.4 nm, closely corresponding to the GME error. Similarly, for the
low SNR simulations, (Figure 6.3, 333 photons per molecule in the entire PSF, local-
ization prediction assumes 200 photons in PSF core), the predicted localization error
is 19.4 nm for MLE and 28.7 nm for GME; at low imaging density, localization error
for DAOSTORM is 25 ± 4 nm. Additional simulations with the EMCCD module of
the simulator turned off (i.e., without electron-multiplying gain) and in the absence
of background noise gave similar results.

I conclude that the modifications to the MLE weighting scheme introduced by
DAOPHOT II increase the localization error to the level of GME rather than MLE.
Although these deviations (1.6 nm at high SNR, 9.3 nm at low SNR) are relatively
small compared with typical experimental resolution (10–20 nm [15]), they will be-
come important as recently-reported ultra-precise localization methods [131] become

more commonplace. In this case, investigation of optimal fitting methods and localization error at high imaging density and in the presence of outliers will enable further improvements in the performance of the algorithm.

A final consideration is the PSF model employed by DAOSTORM during fitting. A useful feature of the DAOSTORM algorithm is that the PSF is derived directly from the data; therefore deviations from a simple Gaussian PSF model, such as those expected a priori [88], or unexpected deviations, e.g., due to imperfect optics, are automatically accommodated and do not affect fitting. However, to simplify fitting, and in particular to maximize fitting speed, the PSF shape is assumed identical for all fluorophores in an image. This is a reasonable assumption for freely rotating fluorophores; however, for the case of samples containing fluorophores with fixed dipole orientation on the timescale of observation, this approach may introduce errors on the order of tens of nanometres [88, 177]; fitting with a more complex model PSF can resolve this issue [88]. Extension of DAOSTORM to use a variable PSF may allow high imaging density analysis of such samples. A particularly exciting application of a variable PSF version of DAOSTORM would be its combination with 3D super-resolution methods [151, 152] which derive the z-position of the fluorophore from the PSF shape.

6.5   Conclusions

In summary, I presented a novel localization algorithm for super-resolution imaging, which significantly improves the performance at high imaging density. This algorithm will be useful for all localization-based super-resolution methods, because it maximizes information content extracted from raw data, reduces acquisition time and increases maximum spatial resolution; these improvements will be particularly useful for challenging applications such as live-cell super-resolution imaging.

DAOSTORM currently uses a model PSF with fixed shape for fitting; an extension

using PSFs with variable shape will allow fitting to fluorophores with fixed dipole orientation [88] and combination with 3D-STORM approaches [151, 152]. DAOSTORM could also be combined with other high-density super-resolution methods (such as PAINT [178, 179], which is based on transient binding of labelled molecules to target structures), increasing the applicability and appeal of super-resolution microscopy.

Conclusions

7.1 Discussion

Single-molecule fluorescence imaging has provided novel insight into many biological phenomena, across a wide range of distance scales of biological interest. On the nanoscale, TIRF-FRET can be used for *in vitro* studies of molecular dynamics over a distance range of $\sim$ 2-10 nm, which is a key scale for understanding how biomolecular machines work as single machines, e.g., the dynamics of DNA polymerase [11] and HIV reverse-transcriptase [10]. On the microscale, super-resolution imaging holds the promise of allowing individual biomolecules to be properly placed in their cellular context, allowing the spatial distribution of large ensembles of molecules to be analysed; initial applications include analysis of distribution of *E. coli* chemotaxis proteins [162], and analysis of chromosomal segregation during cell division in *Calobactur crescentus* [180].

In this thesis, I presented tools to define and extend the spatio-temporal resolution of widefield single-molecule imaging. For TIRF-FRET, I presented derivations which define the theoretical limits of resolution in a FRET measurement. I designed and implemented image analysis software to automate and optimize TIRF-FRET

data analysis. This software allowed us to obtain large, statistically robust datasets which could be used to define the current limits of FRET resolution. After extensive validation of the image analysis software via simulation, the resolution limits of the experimental system were characterized using dsDNA FRET standards. The largest sources of measurement error were identified as acceptor photophysics and focal drift; non-optimal profile fitting was also shown to introduce significant error. I demonstrated FRET resolution equivalent to a distance difference of one DNA base-pair for measurements of dynamic heterogeneity, i.e., for measurements of the fluctuations of an individual molecule. For static heterogeneity measurements, i.e., for the combined measurements of multiple molecules, which were subject to larger measurement errors, I showed that it was possible to resolve the presence of two sub-populations with a difference in donor-acceptor separation of two DNA base-pairs within a single sample.

For localization-based super-resolution imaging, I presented a novel super-resolution localization algorithm, DAOSTORM, designed to analyse images containing many overlapping molecular point spread functions. DAOSTORM and two alternative localization algorithms were used to analyse simulated and experimental data. The results of simulations showed that DAOSTORM can operate at significantly higher imaging density than previous algorithms; dSTORM imaging of fluorescently labelled microtubules confirmed that this algorithm also shows improved performance on real datasets.

7.2   Future work

The TIRF-FRET work presented here has facilitated a number of high-resolution studies in our group. Stephan Uphoff and Johannes Hohlbein are currently studying the binding dynamics of *E. coli* DNA polymerase I on various DNA substrates, and Thorben Cordes, Kristopher Gryte and Alexandra Tomescu are attempting to

resolve single-base-pair translocation events during *E. coli* RNA polymerase initial transcription. The TwoTone software has also generated interest within the research community, and has been downloaded by multiple researchers for use in their own experiments.

I identified that one of the limitations to TIRF-FRET resolution was the use of a non-optimal profile-fitting algorithm in TwoTone; work is currently being carried out by Stephan Uphoff to replace the current profile-fitting algorithm with a maximum likelihood estimator, which should resolve this issue.

An interesting potential application of the theoretical predictions of TIRF-FRET resolution is their combination with the Burst Variance Analysis (BVA) method. In recent work led by Joseph Torella [129], we introduced BVA, where dynamic fluctuations of diffusing biomolecules are detected by comparing the standard deviation of observed FRET distributions with the theoretical expectation value. The theoretical predictions of FRET distribution width for TIRF-FRET measurements will facilitate the application of BVA to surface-immobilized molecules imaged via TIRF. This may allow the measurement of unresolved dynamics in timetraces of individual surface-immobilized molecules, at or just below the temporal resolution of the measurement.

DAOSTORM is already being applied on a regular basis in the Kapanidis lab. Together with Robert Crawford and Javier Periz, I recently carried out initial STORM imaging measurements of the *E. coli* chromosome. Our attempts to carry out such measurements in live cells resulted in high imaging density data, and a small dataset due to an increased photobleaching rate for live-cell measurements. DAOSTORM is very useful in this context since it maximizes the information extracted from a necessarily small dataset.

The extension of DAOSTORM to use a variable PSF during fitting will allow high-resolution fitting of molecules with fixed dipoles [88]; it will also allow com-

bination of DAOSTORM with 3D-STORM methods [151, 152] which use variation in the PSF shape to calculate z-position. I consider "3D-DAOSTORM" a particularly exciting extension of the method since samples showing a large degree of three-dimensional structure necessarily have a much higher "projected" two-dimensional labelling density than relatively thin, flat samples. Since high resolution 3D-STORM imaging necessitates significantly higher effective labelling density than 2D-STORM, and thus higher imaging density, the use of 3D-DAOSTORM or similar methods will be particularly important.

It has not escaped my notice that DAOSTORM could be adapted for purposes other than super-resolution localization. Initially, the most obvious application is TIRF-FRET data analysis. However, for research purposes, the "imaging through-put", i.e., the rate at which data is acquired and analysed, is not as important a parameter for TIRF-FRET as it is for super-resolution microscopy, meaning that TwoTone (or similar software) is usually sufficient. This is not the case in the methodologically related field of fluorescence-based second- and third-generation DNA sequencing [181, 182], where in many cases, as for TIRF-FRET, the brightness of surface-immobilized molecules in multiple emission channels is recorded and analysed [181, 182]. Here, a 6-fold increase in imaging throughput could be very useful, since it could potentially significantly reduce the total genome sequencing time.

7.3 Acknowledgements

APPENDIX A

Publications

Holden S. J., Uphoff S. and Kapanidis A. N. DAOSTORM: an algorithm for high density super-resolution microscopy. *Nat. Methods*, 8(4):279–280, 2011.

Torella J. P., *Holden S. J.*, Santoso Y., Hohlbein J. and Kapanidis A. N. Identifying Molecular Dynamics in Single-Molecule FRET Experiments with Burst Variance Analysis. *Biophys. J.*, 100(6):1568–1577, 2011.

Holden S. J., Uphoff S., Yadin D., Hohlbein J., Le Reste L., Britton O. J. and Kapanidis A. N. Defining the limits of single-molecule FRET resolution in TIRF microscopy. *Biophys. J.*, 99(9):3102–3111, 2010.

Uphoff S., *Holden S. J.*, Le Reste L., van de Linde S., Heilemann M. and Kapanidis A. N. Measuring multiple distances within a single molecule using switchable FRET. *Nat. Methods*, 7(10):831–836, 2010.

Lymperopoulos K., Crawford R., Torella J. P., Heilemann M., Hwang L. C., *Holden S. J.* and Kapanidis A. N. Single-molecule DNA biosensors for protein and ligand detection. *Angew. Chem.*, 49(7):1316–1320, 2010.

Holden S.J. and Kapanidis A. N. Alternating-Laser Excitation and Pulsed-Interleaved Excitation of Single Molecules. In *Single Particle Tracking and Single Molecule Energy Transfer: Applications in the Bio and Nano Sciences.* Wiley-VHC, Berlin, Germany, 2009.

Hwang L. C., Hohlbein J., *Holden S. J.* and Kapanidis A. N. Single-Molecule FRET: Methods and Biological Applications. In *Handbook of Single Molecule Biophysics.* Springer, New York, 2009.

Refactoring the electron-multiplying gain equation

Simulations described in Chapter 3 included a model of the electron-multiplying gain register of an EMCCD, by performing rejection sampling [100] of the approximate probability density function for electron counts resulting from a gain register [99]:

$$P(n) \begin{cases} = \frac{(n-m+1)^{m-1}}{(m-1)!(G-1+1/m)^m} \exp\left(-\frac{n-m+1}{G-1+1/m}\right) & \text{if } n \geq m, \\ = 0 & \text{otherwise,} \end{cases} \tag{B.1}$$

where n is the final electron count, m is the input photon count and G is the electron multiplying gain.

If Eq. B.1 is used directly in the simulations, serious loss of precision and floating point overflow errors occur during calculation, because $P(n)$, which is between 0 and 1, is calculated by division of one very large number by another very large number. This can be avoided by refactoring Eq. B.1 as

$$P(n) \begin{cases} = \exp\left(\begin{array}{c} -\frac{n-m+1}{g-1+1/m} + (m-1)\ln(n-m+1) \\ -\ln(m-1)! - m\ln(g-1+1/m) \end{array} \right) & \text{if } n \geq m, \\ = 0 & \text{otherwise.} \end{cases} \tag{B.2}$$

For $(m - 1) \geq 50$, Stirling's approximation is applied, i.e.,

$$\ln(m - 1)! \approx (m - 1)\ln(m - 1) - (m - 1) + \frac{\ln(2\pi(m - 1))}{2}. \qquad \text{(B.3)}$$

The cut-off point of $(m - 1) \geq 50$ is arbitary, but at this point, the error introduced on application of Stirling's approximation is $\sim 2 \times 10^{-3}$, which is small compared to other terms in Eq. B.2. I therefore consider this to be a reasonable value to choose.

Derivation of photon counting error due to PSF overlap

C.1   Probability distribution of overlapping molecules

We require the probability distribution, P_g, that g molecules are in an "overlapping" group, given a random distribution of surface immobilized molecules, surface density n. I define overlapping as unresolved according to the Rayleigh criterion, i.e., that they are separated by $|\Delta \mathbf{x}| < 2s$, where s is the width of a circular 2D Gaussian PSF defined by Eq. 3.1. If we first consider the molecules on an individual basis, then the probability, P_i, that an individual molecule is in a group of i molecules is equal to the probability that there are $i - 1$ other molecules within an area $\pi(2s)^2$ around that molecule. This is determined by by Poisson statistics:

$$P_i = \frac{\mu^{i-1}}{(i-1)!}e^{-\mu}, \quad \mu = 4\pi s^2 n, \tag{C.1}$$

where n is the surface density of molecules.

We can relate the probability, P_i, of observing an individual molecule within a group of i molecules, to the probability, P_g, of observing a group containing $g = i$ molecules. This is achieved by noting that for P_g, each group is counted only once,

whereas for P_i, each group is counted $g = i$ times. Taking this into account, and normalising, we find:

$$P_g = \frac{P_i/i}{A}, \quad A = \sum_{i=1}^{\infty} \frac{P_i}{i} = \frac{1 - e^{-\mu}}{\mu}. \tag{C.2}$$

C.2   Photon counting error for overlapping molecules

The fractional root mean square (RMS) photon counting error, $\Delta M_{rms}/M$, is just equal to the counting error:

$$\Delta M_{rms}/M = \Delta g_{rms} = \langle (g-1)^2 \rangle^{1/2}. \tag{C.3}$$

This is because the "correct" count for a group of overlapping molecules is one, i.e., no counting error is observed for the case that all molecules are successfully resolved into individual groups containing $g = 1$ molecules. All unresolved groups of g molecules therefore have a counting error of $g - 1$.

Applying Eq. C.2, the RMS photon counting error is thus

$$\frac{\Delta M_{rms}}{M} = \left\{ \sum_{g=1}^{\infty} (g-1)^2 P_g \right\}^{1/2}, \tag{C.4}$$

$$= \left\{ A^{-1} \sum_{i=1}^{\infty} \frac{(i-1)^2}{i} P_i \right\}^{1/2}, \tag{C.5}$$

$$= \left\{ A^{-1} \sum_{i=1}^{\infty} \frac{(i-1)^2}{i!} \mu^{i-1} e^{-\mu} \right\}^{1/2}, \tag{C.6}$$

$$= \left\{ \frac{1 - e^{-\mu} - \mu + \mu^2}{1 - e^{-\mu}} \right\}^{1/2}. \tag{C.7}$$

Bibliography

[1] Shera, E. B., N. K. Seitzinger, L. M. Davis, R. A. Keller, and S. A. Soper, 1990. Detection of single fluorescent molecules. *Chem. Phys. Lett.* 174:553–557.

[2] Lakowicz, J. R., 2006. Principles of fluorescence spectroscopy. Kluwer Academic/ Plenum, New York; London, 3rd edition.

[3] Deniz, A. A., T. A. Laurence, G. S. Beligere, M. Dahan, A. B. Martin, D. S. Chemla, P. E. Dawson, P. G. Schultz, and S. Weiss, 2000. Single-molecule protein folding: diffusion fluorescence resonance energy transfer studies of the denaturation of chymotrypsin inhibitor 2. *Proc. Natl. Acad. Sci. U.S.A.* 97:5179–84.

[4] Schuler, B., and W. A. Eaton, 2008. Protein folding studied by single-molecule FRET. *Curr. Opin. Struct. Biol.* 18:16–26.

[5] Schuler, B., E. A. Lipman, and W. A. Eaton, 2002. Probing the free-energy surface for protein folding with single-molecule fluorescence spectroscopy. *Nature* 419:743–747.

[6] Rhoades, E., E. Gussakovsky, and G. Haran, 2003. Watching Proteins Fold One Molecule at a Time. *Proc. Natl. Acad. Sci. U.S.A.* 100:3197–3202.

[7] Rothwell, P. J., S. Berger, O. Kensch, S. Felekyan, M. Antonik, B. M. Wöhrl, T. Restle, R. S. Goody, and C. A. M. Seidel, 2003. Multiparameter single-molecule fluorescence spectroscopy reveals heterogeneity of HIV-1 reverse transcriptase:primer/template complexes. *Proc. Natl. Acad. Sci. U.S.A.* 100:1655–1660.

[8] Ha, T., I. Rasnik, W. Cheng, H. P. Babcock, G. H. Gauss, T. M. Lohman, and S. Chu, 2002. Initiation and re-initiation of DNA unwinding by the Escherichia coli Rep helicase. *Nature* 419:638–641.

[9] Myong, S., I. Rasnik, C. Joo, T. M. Lohman, and T. Ha, 2005. Repetitive shuttling of a motor protein on DNA. *Nature* 437:1321–1325.

[10] Abbondanzieri, E. A., G. Bokinsky, J. W. Rausch, J. X. Zhang, S. F. J. Le Grice, and X. Zhuang, 2008. Dynamic binding orientations direct activity of HIV reverse transcriptase. *Nature* 453:184–189.

[11] Christian, T. D., L. J. Romano, and D. Rueda, 2009. Single-molecule measurements of synthesis by DNA polymerase with base-pair resolution. *Proc. Natl. Acad. Sci. U.S.A.* 106:21109–21114.

[12] Margeat, E., A. N. Kapanidis, P. Tinnefeld, Y. Wang, J. Mukhopadhyay, R. H. Ebright, and S. Weiss, 2006. Direct observation of abortive initiation and promoter escape within single immobilized transcription complexes. *Biophys. J.* 90:1419–31.

[13] Hell, S. W., 2007. Far-Field Optical Nanoscopy. *Science* 316:1153–1158.

[14] Rust, M. J., M. Bates, and X. Zhuang, 2006. Sub-diffraction-limit imaging by stochastic optical reconstruction microscopy (STORM). *Nat. Methods* 3:793–796.

[15] Heilemann, M., S. van de Linde, M. Schuttpelz, R. Kasper, B. Seefeldt, A. Mukherjee, P. Tinnefeld, and M. Sauer, 2008. Subdiffraction-Resolution Fluorescence Imaging with Conventional Fluorescent Probes. *Angew. Chem., Int. Ed.* 47:6172–6176.

[16] Betzig, E., G. H. Patterson, R. Sougrat, O. W. Lindwasser, S. Olenych, J. S. Bonifacino, M. W. Davidson, J. Lippincott-Schwartz, and H. F. Hess, 2006. Imaging Intracellular Fluorescent Proteins at Nanometer Resolution. *Science* 313:1642–1645.

[17] Manley, S., J. M. Gillette, G. H. Patterson, H. Shroff, H. F. Hess, E. Betzig, and J. Lippincott-Schwartz, 2008. High-density mapping of single-molecule trajectories with photoactivated localization microscopy. *Nat. Methods* 5:155–157.

[18] Toomre, D., and J. Bewersdorf, 2010. A New Wave of Cellular Imaging. *Annu. Rev. Cell Dev. Biol.* 26:285–314.

[19] Steinhauer, C., C. Forthmann, J. Vogelsang, and P. Tinnefeld, 2008. Super-resolution Microscopy on the Basis of Engineered Dark States. *Journal of the American Chemical Society* 130:16840–16841.

[20] Wombacher, R., M. Heidbreder, S. van de Linde, M. P. Sheetz, M. Heilemann, V. W. Cornish, and M. Sauer, 2010. Live-cell super-resolution imaging with trimethoprim conjugates. *Nat. Methods* 7:717–719.

[21] Agrawal, A., R. Deo, G. D. Wang, M. D. Wang, and S. Nie, 2008. Nanometer-scale mapping and single-molecule detection with color-coded nanoparticle probes. *Proc. Natl. Acad. Sci. U.S.A.* 105:3298–3303.

[22] Cronin, B., B. de Wet, and M. I. Wallace, 2009. Lucky Imaging: Improved Localization Accuracy for Single Molecule Imaging. *Biophysical Journal* 96:2912–2917.

[23] Santoso, Y., C. Joyce, O. Potapova, L. L. Reste, J. Hohlbein, J. Torella, N. Grindley, and A. Kapanidis, 2010. Conformational transitions in DNA polymerase I revealed by single-molecule FRET. *Proc. Natl. Acad. Sci. U.S.A.* 107:715.

[24] Alberts, B., A. Johnson, J. Lewis, M. Raff, K. Roberts, and P. Walter, 2002. Molecular Biology of the Cell. Garland Science, London, 4 edition.

[25] Hohng, S., R. Zhou, M. K. Nahas, J. Yu, K. Schulten, D. M. J. Lilley, and T. Ha, 2007. Fluorescence-Force Spectroscopy Maps Two-Dimensional Reaction Landscape of the Holliday Junction. *Science* 318:279–283.

[26] Holden, S. J., and A. N. Kapanidis, 2009. Alternating-Laser Excitation and Pulsed-Interleaved Excitation of Single Molecules. *In* Single Particle Tracking and Single Molecule Energy Transfer: Applications in the Bio and Nano Sciences. Wiley-VHC, Berlin.

[27] Hwang, L. C., J. Hohlbein, S. J. Holden, and A. N. Kapanidis, 2009. Single-Molecule FRET: The Method and Its Applications. *In* Springer Handbook of Single-Molecule Biophysics. Springer Press, Berlin, Germany.

[28] Andrews, D., and D. Bradshaw, 2004. Virtual photons, dipole fields and energy transfer: a quantum electrodynamical approach. *Eur. J. Phys.* 25:845.

[29] Clegg, R. M., 1992. Fluorescence resonance energy transfer and nucleic acids. *Methods Enzymol.* 211:353–88.

[30] Jares-Erijman, E. A., and T. M. Jovin, 2003. FRET imaging. *Nat. Biotechnol.* 21:1387–1395.

[31] Dale, R. E., J. Eisinger, and W. E. Blumberg, 1979. The orientational freedom of molecular probes. The orientation factor in intramolecular energy transfer. *Biophys. J.* 26:161–93.

[32] Kapanidis, A. N., Y. W. Ebright, and R. H. Ebright, 2001. Site-Specific Incorporation of Fluorescent Probes into Protein: Hexahistidine-Tag-Mediated Fluorescent Labeling with (Ni^{2+}):Nitrilotriacetic Acid)$_n$-Fluorochrome Conjugates. *J. Am. Chem. Soc.* 123:12123–5.

[33] Stryer, L., and R. P. Haugland, 1967. Energy transfer: a spectroscopic ruler. *Proc. Natl. Acad. Sci. U.S.A.* 58:719–726.

[34] Clegg, R. M., A. I. Murchie, A. Zechel, and D. M. Lilley, 1993. Observing the helical geometry of double-stranded DNA in solution by fluorescence resonance energy transfer. *Proc. Natl. Acad. Sci. U.S.A.* 90:2994–2998.

[35] Miki, M., and T. Iio, 1993. Kinetics of structural changes of reconstituted skeletal muscle thin filaments observed by fluorescence resonance energy transfer. *J. Biol. Chem.* 268:7101–7106.

[36] Houston, P., and T. Kodadek, 1994. Spectrophotometric assay for enzyme-mediated unwinding of double-stranded DNA. *Proc. Natl. Acad. Sci. U.S.A.* 91:5471–5474.

[37] Lippincott-Schwartz, J., E. Snapp, and A. Kenworthy, 2001. Studying protein dynamics in living cells. *Nat. Rev. Mol. Cell Biol.* 2:444–456.

[38] Miyawaki, A., R. Y. Tsien, S. D. Emr, and J. N. A. J. Thorner, 2000. Monitoring protein conformations and interactions by fluorescence resonance energy transfer between mutants of green fluorescent protein. *In* Applications of Chimeric Genes and Hybrid Proteins - Part B: Cell Biology and Physiology, Academic Press, Burlington, MA, volume 327, 472–500.

[39] Zimmer, M., 2002. Green Fluorescent Protein (GFP): Applications, Structure, and Related Photophysical Behavior. *Chem. Rev.* 102:759–782.

[40] Clegg, R. M., 1995. Fluorescence resonance energy transfer. *Curr. Opin. Biotechnol.* 6:103–110.

[41] Selvin, P. R., 1995. Fluorescence resonance energy transfer. *Methods Enzymol.* 246:300–334.

[42] Selvin, P. R., 2000. The renaissance of fluorescence resonance energy transfer. *Nat. Struct. Biol.* 7:730–4.

[43] Ha, T., X. Zhuang, H. D. Kim, J. W. Orr, J. R. Williamson, and S. Chu, 1999. Ligand-induced conformational changes observed in single RNA molecules. *Proc. Natl. Acad. Sci. U.S.A.* 96:9077–9082.

[44] Kim, H. D., G. U. Nienhaus, T. Ha, J. W. Orr, J. R. Williamson, and S. Chu, 2002. Mg^{2+}-dependent conformational change of RNA studied by fluorescence correlation and FRET on immobilized single molecules. *Proc. Natl. Acad. Sci. U.S.A.* 99:4284 –4289.

[45] Henzler-Wildman, K. A., V. Thai, M. Lei, M. Ott, M. Wolf-Watz, T. Fenn, E. Pozharski, M. A. Wilson, G. A. Petsko, M. Karplus, C. G. Hubner, and D. Kern, 2007. Intrinsic motions along an enzymatic reaction trajectory. *Nature* 450:838–44.

[46] Zhuang, X., L. E. Bartley, H. P. Babcock, R. Russell, T. Ha, D. Herschlag, and S. Chu, 2000. A Single-Molecule Study of RNA Catalysis and Folding. *Science* 288:2048–2051.

[47] Zhuang, X., H. Kim, M. J. B. Pereira, H. P. Babcock, N. G. Walter, and S. Chu, 2002. Correlating Structural Dynamics and Function in Single Ribozyme Molecules. *Science* 296:1473 –1476.

[48] Solomatin, S. V., M. Greenfeld, S. Chu, and D. Herschlag, 2010. Multiple native states reveal persistent ruggedness of an RNA folding landscape. *Nature* 463:681–684.

[49] Hohng, S., T. J. Wilson, E. Tan, R. M. Clegg, D. M. Lilley, and T. Ha, 2004. Conformational Flexibility of Four-way Junctions in RNA. *J. Mol. Biol.* 336:69–79.

[50] Tan, X., P. Nalbant, A. Toutchkine, D. Hu, E. R. Vorpagel, K. M. Hahn, and H. Peter Lu, 2004. Single-Molecule Study of Protein-Protein Interaction Dynamics in a Cell Signaling System. *J. Phys. Chem. B* 108:737–744.

[51] Tomishige, M., N. Stuurman, and R. D. Vale, 2006. Single-molecule observations of neck linker conformational changes in the kinesin motor protein. *Nat. Struct. Mol. Biol.* 13:887–894.

[52] Mori, T., R. D. Vale, and M. Tomishige, 2007. How kinesin waits between steps. *Nature* 450:750–754.

[53] Börsch, M., M. Diez, B. Zimmermann, R. Reuter, and P. Gräber, 2002. Stepwise rotation of the γ-subunit of EF_0F_1-ATP synthase observed by intramolecular single-molecule fluorescence resonance energy transfer. *FEBS Lett.* 527:147–152.

[54] Diez, M., B. Zimmermann, M. Borsch, M. Konig, E. Schweinberger, S. Steigmiller, R. Reuter, S. Felekyan, V. Kudryavtsev, C. A. M. Seidel, and P. Graber, 2004. Proton-powered subunit rotation in single membrane-bound F_0F_1-ATP synthase. *Nat. Struct. Mol. Biol.* 11:135–141.

[55] Zimmermann, B., M. Diez, M. Börsch, and P. Gräber, 2006. Subunit movements in membrane-integrated EF_0F_1 during ATP synthesis detected by single-molecule spectroscopy. *Biochim. Biophys. Acta, Bioenerg.* 1757:311–319.

[56] Deniz, A. A., M. Dahan, J. R. Grunwell, T. Ha, A. E. Faulhaber, D. S. Chemla, S. Weiss, and P. G. Schultz, 1999. Single-pair fluorescence resonance energy transfer on freely diffusing molecules: Observation of Förster distance dependence and subpopulations. *Proc. Natl. Acad. Sci. U.S.A.* 96:3670–3675.

[57] Moerner, W. E., and D. P. Fromm, 2003. Methods of single-molecule fluorescence spectroscopy and microscopy. *Rev. Sci. Instrum.* 74:3597.

[58] Lamichhane, R., A. Solem, W. Black, and D. Rueda, 2010. Single-molecule FRET of protein-nucleic acid and protein-protein complexes: Surface passivation and immobilization. *Methods* 52:192–200.

[59] Nie, S., D. T. Chiu, and R. N. Zare, 1994. Probing individual molecules with confocal fluorescence microscopy. *Science* 266:1018–1021.

[60] Funatsu, T., and Y. Harada, 1995. Imaging of single fluorescent molecules and individual ATP turnovers by single myosin molecules. *Nature* 374:555–559.

[61] Axelrod, D., 2001. Total internal reflection fluorescence microscopy in cell biology. *Traffic* 2:764–774.

[62] Roy, R., S. Hohng, and T. Ha, 2008. A practical guide to single-molecule FRET. *Nat. Methods* 5:507–516.

[63] Tokunaga, M., N. Imamoto, and K. Sakata-Sogawa, 2008. Highly inclined thin illumination enables clear single-molecule imaging in cells. *Nat. Methods* 5:159–161.

[64] Lee, N. K., A. N. Kapanidis, Y. Wang, X. Michalet, J. Mukhopadhyay, R. H. Ebright, and S. Weiss, 2005. Accurate FRET measurements within single diffusing biomolecules using alternating-laser excitation. *Biophys. J.* 88:2939–53.

[65] Hecht, E., 1998. Optics. Addison-Wesley, Reading, MA.

[66] Schluesche, P., G. Stelzer, E. Piaia, D. C. Lamb, and M. Meisterernst, 2007. NC2 mobilizes TBP on core promoter TATA boxes. *Nat. Struct. Mol. Biol.* 14:1196–1201.

[67] Wolter, S., M. Schüttpelz, M. Tscherepanow, S. van de Linde, M. Heilemann, and M. Sauer, 2010. Real-time computation of subdiffraction-resolution fluorescence images. *J. Microsc.* 237:12–22.

[68] Kapanidis, A. N., N. K. Lee, T. A. Laurence, S. Doose, E. Margeat, and S. Weiss, 2004. Fluorescence-aided molecule sorting: Analysis of structure and interactions by alternating-laser excitation of single molecules. *Proc. Natl. Acad. Sci. U.S.A.* 101:8936–8941.

[69] Andrecka, J., R. Lewis, F. Bruckner, E. Lehmann, P. Cramer, and J. Michaelis, 2008. Single-molecule tracking of mRNA exiting from RNA polymerase II. *Proc. Natl. Acad. Sci. U.S.A.* 105:135–40.

[70] Berg, J., J. Tymoczko, and L. Stryer, 2002. Biochemistry. WH Freeman, New York, NY.

[71] Nir, E., X. Michalet, K. M. Hamadani, T. A. Laurence, D. Neuhauser, Y. Kovchegov, and S. Weiss, 2006. Shot-noise limited single-molecule FRET histograms: comparison between theory and experiments. *J. Phys. Chem. B* 110:22103–24.

[72] Antonik, M., S. Felekyan, A. Gaiduk, and C. A. M. Seidel, 2006. Separating structural heterogeneities from stochastic variations in fluorescence resonance energy transfer distributions via photon distribution analysis. *J. Phys. Chem. B* 110:6970–6978.

[73] Gopich, I. V., and A. Szabo, 2007. Single-Molecule FRET with Diffusion and Conformational Dynamics. *J. Phys. Chem. B* 111:12925–12932.

[74] Deniz, A. A., T. A. Laurence, M. Dahan, D. S. Chemla, P. G. Schultz, and S. Weiss, 2001. Ratiometric single-molecule studies of freely diffusing biomolecules. *Annu. Rev. Phys. Chem.* 52:233–53.

[75] Chung, H. S., J. M. Louis, and W. A. Eaton, 2010. Distinguishing between Protein Dynamics and Dye Photophysics in Single-Molecule FRET Experiments. *Biophys. J.* 98:696–706.

[76] Kalinin, S., E. Sisamakis, S. W. Magennis, S. Felekyan, and C. A. M. Seidel, 2010. On the Origin of Broadening of Single-Molecule FRET Efficiency Distributions beyond Shot Noise Limits. *J. Phys. Chem. B* 114:6197–6206.

[77] Thompson, R. E., D. R. Larson, and W. W. Webb, 2002. Precise nanometer localization analysis for individual fluorescent probes. *Biophys. J.* 82:2775–2783.

[78] King, I. R., 1983. Accuracy of measurement of star images on a pixel array. *Pub. A. S. P.* 95:163–168.

[79] Uphoff, S., 2009. Probing molecular and cellular structure using single molecule photoswitching. Master's thesis, University of Oxford.

[80] Holden, S. J., S. Uphoff, J. Hohlbein, D. Yadin, L. Le Reste, O. J. Britton, and A. N. Kapanidis, 2010. Defining the Limits of Single–Molecule FRET Resolution in TIRF Microscopy. *Biophys. J.* 99:3102–3111.

[81] Cheezum, M. K., W. Walker, and W. H. Guilford, 2001. Quantitative comparison of algorithms for tracking single fluorescent particles. *Biophys. J.* 81:2378–2388.

[82] Howell, S. B., 2006. Handbook of CCD Astronomy. Cambridge University Press, Cambridge, UK.

[83] Santoso, Y., L. C. Hwang, L. Le Reste, and A. N. Kapanidis, 2008. Red light, green light: probing single molecules using alternating-laser excitation. *Biochem. Soc. Trans.* 036:738–744.

[84] Basden, A. G., C. A. Haniff, and C. D. Mackay, 2003. Photon counting strategies with low-light-level CCDs. *Mon. Not. R. Astron. Soc.* 345:985–991.

[85] Irwin, M. J., 1985. Automatic analysis of crowded fields. *Mon. Not. R. Astron. Soc.* 214.

[86] Hogg, R., and A. Craig, 1978. Introduction to mathematical statistics. McMillan, New York, NY.

[87] Baker, S., and R. D. Cousins, 1984. Clarification of the use of chi-square and likelihood functions in fits to histograms. *Nucl. Instrum. Methods* 221:437 – 442.

[88] Mortensen, K. I., L. S. Churchman, J. A. Spudich, and H. Flyvbjerg, 2010. Optimized localization analysis for single-molecule tracking and super-resolution microscopy. *Nat. Methods* 7:377–381.

[89] Stetson, P. B., 1987. DAOPHOT: A computer program for crowded-field stellar photometry. *Pub. A. S. P.* 99:191–222.

[90] Taylor, J., 1997. An introduction to error analysis: the study of uncertainties in physical measurements. University Science Books, Herndon, VA.

[91] Robbins, M., and B. Hadwen, 2003. The noise performance of electron multiplying charge-coupled devices. *IEEE T. Electron. Dev.* 50:1227–1232.

[92] E2V Technologies. Low Light Technical Note 5: An Overview of the Ageing Characteristics of L3Vision Sensors. `http://www.e2v.com`. Accessed on 24 Jun. 2010.

[93] Tulloch, S. M., 2004. Photon counting and fast photometry with L3 CCDs. *In* Ground-based Instrumentation for Astronomy. SPIE, Bellingham, WA.

[94] Ulbrich, M. H., and E. Y. Isacoff, 2007. Subunit counting in membrane-bound proteins. *Nat. Methods* 4:319–321.

[95] Merline, W. J., and S. B. Howell, 1995. A realistic model for point-sources imaged on array detectors: The model and initial results. *Exp. Astron.* 6:163–210.

[96] van den Bos, A., 2007. Parameter Estimation for Scientists and Engineers. John Wiley & Sons, Inc., Hoboken, NJ, USA.

[97] Irwin, M. J., 1997. Detectors and Data Analysis Techniques for Wide Field Optical Imaging. *Instrumentation for large telescopes: VII Canary Islands Winter School of Astrophysics* 35.

[98] Howell, S. B., 1989. Two-dimensional aperture photometry - Signal-to-noise ratio of point-source observations and optimal data-extraction techniques. *Pub. A. S. P.* 101:616–622.

[99] Tubbs, R. N., 2004. Lucky exposures: diffraction-limited astronomical imaging through the atmosphere. Ph.D. thesis, University of Cambridge.

[100] Neumann, J. V., 1951. Various techniques used in connection with random digits. *Applied Math Series* 12:36–38.

[101] Crocker, J. C., and D. G. Grier, 1996. Methods of Digital Video Microscopy for Colloidal Studies. *J. Colloid Interface Sci.* 179:298–310.

[102] Buonanno, R., and G. Iannicola, 1989. Stellar photometry with big pixels. *Pub. A. S. P.* 101:294–301.

[103] Holden, S. J. TwoTone: TIRF-FRET data analysis software. `http://www.physics.ox.ac.uk/Users/kapanidis/Group/Main.Software.html`.

[104] Churchman, L. S., Z. Ökten, R. S. Rock, J. F. Dawson, and J. A. Spudich, 2005. Single molecule high-resolution colocalization of Cy3 and Cy5 attached to macromolecules measures intramolecular distances through time. *Proc. Natl. Acad. Sci. U.S.A.* 102:1419–1423.

[105] Groth, E. J., 1986. A pattern-matching algorithm for two-dimensional coordinate lists. *Astron. J.* 91.

[106] Murtagh, F., 1992. A new approach to point-pattern matching. *Pub. A. S. P.* 104:301–307.

[107] Hastie, T., R. Tibshirani, and J. Friedman, 2001. The elements of statistical learning: data mining, inference, and prediction. Springer-Verlag, New York, NY.

[108] Yildiz, A., J. N. Forkey, S. A. McKinney, T. Ha, Y. E. Goldman, and P. R. Selvin, 2003. Myosin V walks hand-over-hand: single fluorophore imaging with 1.5-nm localization. *Science* 300:2061–2065.

[109] Janes, K. A., and J. N. Heasley, 1993. Stellar Photometry Software. *Pub. A. S. P.* 105:527–537.

[110] Lourakis, M. I. A. levmar: Levenberg-Marquardt nonlinear least squares algorithms in C/C++. `http://www.ics.forth.gr/~lourakis/levmar/`. Accessed on 1 Oct. 2009.

[111] Dennis, J., and R. Schnabel, 1996. Numerical methods for unconstrained optimization and nonlinear equations. Society for Industrial and Applied Mathematics, Philadelphia, PA.

[112] Price, P. F., 1979. A comparison of the least-squares and maximum-likelihood estimators for counts of radiation quanta which follow a Poisson distribution. *Acta Crystallogr. A* 35:57–60.

[113] Stetson, P. B., 1990. On the growth-curve method for calibrating stellar photometry with CCDs. *Pub. A. S. P.* 102:932–948.

[114] Ferguson, T. S., 1996. A course in large sample theory. CRC Press, Boca Raton, FL.

[115] James, J., 1976. Light microscopic techniques in biology and medicine. Springer, New York, NY.

[116] Joo, C., and T. Ha, 2008. Single-Molecule FRET with Total Internal Reflection Microscopy. *In* Single-molecule techniques: a laboratory manual. CSHL Press, Cold Spring Harbor, NY.

[117] Zhang, N. F., 2008. Allan variance of time series models for measurement data. *Metrologia* 45:549–561.

[118] Allan, D., 1966. Statistics of atomic frequency standards. *Proc. IEEE* 54:221–230.

[119] Gibson, G. M., J. Leach, S. Keen, A. J. Wright, and M. J. Padgett, 2008. Measuring the accuracy of particle position and force in optical tweezers using high-speed video microscopy. *Opt. Express* 16:14561–14570.

[120] Czerwinski, F., A. C. Richardson, and L. B. Oddershede, 2009. Quantifying Noise in Optical Tweezers by Allan Variance. *Opt. Express* 17:13255–13269.

[121] Iqbal, A., S. Arslan, B. Okumus, T. J. Wilson, G. Giraud, D. G. Norman, T. Ha, and D. M. J. Lilley, 2008. Orientation dependence in fluorescent energy transfer between Cy3 and Cy5 terminally attached to double-stranded nucleic acids. *Proc. Natl. Acad. Sci. U.S.A.* 105:11176–11181.

[122] Brokmann, X., J. Hermier, G. Messin, P. Desbiolles, J. Bouchaud, and M. Dahan, 2003. Statistical Aging and Nonergodicity in the Fluorescence of Single Nanocrystals. *Phys. Rev. Lett.* 90:120601.

[123] McCann, J. J., U. B. Choi, L. Zheng, K. Weninger, and M. E. Bowen, 2010. Optimizing Methods to Recover Absolute FRET Efficiency from Immobilized Single Molecules. *Biophys. J.* 99:961–970.

[124] McKinney, S. A., C. Joo, and T. Ha, 2006. Analysis of Single-Molecule FRET Trajectories Using Hidden Markov Modeling. *Biophys. J.* 91:1941–1951.

[125] Cordes, T., J. Vogelsang, and P. Tinnefeld, 2009. On the mechanism of Trolox as antiblinking and antibleaching reagent. *J. Am. Chem. Soc.* 131:5018–5019.

[126] Aitken, C. E., R. A. Marshall, and J. D. Puglisi, 2008. An Oxygen Scavenging System for Improvement of Dye Stability in Single-Molecule Fluorescence Experiments. *Biophys. J.* 94:1826–1835.

[127] Uphoff, S., K. Gryte, G. Evans, and A. N. Kapanidis, 2011. Improved Temporal Resolution and Linked Hidden Markov Modeling for Switchable Single-Molecule FRET. *ChemPhysChem* 12:571–579.

[128] Santoso, Y., J. P. Torella, and A. N. Kapanidis, 2010. Characterizing Single-Molecule FRET Dynamics with Probability Distribution Analysis. *ChemPhysChem* 11:2209–2219.

[129] Torella, J. P., S. J. Holden, Y. Santoso, J. Hohlbein, and A. N. Kapanidis, 2011. Identifying Molecular Dynamics in Single-Molecule FRET Experiments with Burst Variance Analysis. *Biophys. J.* 100:1568–1577.

[130] Abbe, E., 1873. Beiträge zur Theorie des Mikroskops und der mikroskopischen Wahrnehmung. *Archiv für Mikroskopische Anatomie* 9:413–418.

[131] Pertsinidis, A., Y. Zhang, and S. Chu, 2010. Subnanometre single-molecule localization, registration and distance measurements. *Nature* 466:647–651.

[132] Cordes, T., M. Strackharn, S. W. Stahl, W. Summerer, C. Steinhauer, C. Forthmann, E. M. Puchner, J. Vogelsang, H. E. Gaub, and P. Tinnefeld, 2010. Resolving Single-Molecule Assembled Patterns with Superresolution Blink-Microscopy. *Nano Letters* 10:645–651.

[133] Huang, B., H. Babcock, and X. Zhuang, 2010. Breaking the Diffraction Barrier: Super-Resolution Imaging of Cells. *Cell* 143:1047–1058.

[134] Heintzmann, R., and M. G. L. Gustafsson, 2009. Subdiffraction resolution in continuous samples. *Nat. Photonics* 3:362–364.

[135] Hofmann, M., C. Eggeling, S. Jakobs, and S. W. Hell, 2005. Breaking the diffraction barrier in fluorescence microscopy at low light intensities by using reversibly photoswitchable proteins. *Proc. Natl. Acad. Sci. U.S.A.* 102:17565–17569.

[136] Hell, S. W., and J. Wichmann, 1994. Breaking the diffraction resolution limit by stimulated emission: stimulated-emission-depletion fluorescence microscopy. *Optics Letters* 19:780–782.

[137] Meyer, L., D. Wildanger, R. Medda, A. Punge, S. O. Rizzoli, G. Donnert, and S. W. Hell, 2008. Dual-Color STED Microscopy at 30-nm Focal-Plane Resolution. *Small* 4:1095–1100.

[138] Moneron, G., R. Medda, B. Hein, A. Giske, V. Westphal, and S. W. Hell, 2010. Fast STED microscopy with continuous wave fiber lasers. *Opt. Express* 18:1302–1309.

[139] Schröder, J., H. Benink, M. Dyba, and G. V. Los, 2009. In Vivo Labeling Method Using a Genetic Construct for Nanoscale Resolution Microscopy. *Biophys. J.* 96:L1–L3.

[140] Rittweger, E., K. Y. Han, S. E. Irvine, C. Eggeling, and S. W. Hell, 2009. STED microscopy reveals crystal colour centres with nanometric resolution. *Nat Photon* 3:144–147.

[141] Gustafsson, M. G. L., 2000. Surpassing the lateral resolution limit by a factor of two using structured illumination microscopy. *J. Microsc.* 198:82–87.

[142] Gustafsson, M. G. L., L. Shao, P. M. Carlton, C. J. R. Wang, I. N. Golubovskaya, W. Z. Cande, D. A. Agard, and J. W. Sedat, 2008. Three-dimensional resolution doubling in wide-field fluorescence microscopy by structured illumination. *Biophys. J.* 94:4957–4970.

[143] Gustafsson, M. G. L., 2005. Nonlinear structured-illumination microscopy: Wide-field fluorescence imaging with theoretically unlimited resolution. *Proc. Natl. Acad. Sci. U.S.A.* 102:13081–13086.

[144] Born, M., and E. Wolf, 1999. Principles of Optics. Cambridge University Press, Cambridge, UK.

[145] Ambrose, W. P., T. Basche, and W. E. Moerner, 1991. Detection and spectroscopy of single pentacene molecules in a p-terphenyl crystal by means of fluorescence excitation. *J. Chem. Phys.* 95:7150.

[146] Gelles, J., B. J. Schnapp, and M. P. Sheetz, 1988. Tracking kinesin-driven movements with nanometre-scale precision. *Nature* 331:450–453.

[147] Patterson, G. H., and J. Lippincott-Schwartz, 2002. A Photoactivatable GFP for Selective Photolabeling of Proteins and Cells. *Science* 297:1873–1877.

[148] Heilemann, M., E. Margeat, R. Kasper, M. Sauer, and P. Tinnefeld, 2005. Carbocyanine Dyes as Efficient Reversible Single-Molecule Optical Switch. *J. Am. Chem. Soc.* 127:3801–3806.

[149] Bates, M., T. R. Blosser, and X. Zhuang, 2005. Short-Range Spectroscopic Ruler Based on a Single-Molecule Optical Switch. *Phys. Rev. Lett.* 94:108101.

[150] Hess, S., T. Girirajan, and M. Mason, 2006. Ultra-High Resolution Imaging by Fluorescence Photoactivation Localization Microscopy. *Biophys. J.* 91:4258–4272.

[151] Huang, B., W. Wang, M. Bates, and X. Zhuang, 2008. Three-Dimensional Super-Resolution Imaging by Stochastic Optical Reconstruction Microscopy. *Science* 319:810–813.

[152] Pavani, S. R. P., M. A. Thompson, J. S. Biteen, S. J. Lord, N. Liu, R. J. Twieg, R. Piestun, and W. E. Moerner, 2009. Three-dimensional, single-molecule fluorescence imaging beyond the diffraction limit by using a double-helix point spread function. *Proc. Natl. Acad. Sci. U.S.A.* 106:2995–2999.

[153] Shtengel, G., J. A. Galbraith, C. G. Galbraith, J. Lippincott-Schwartz, J. M. Gillette, S. Manley, R. Sougrat, C. M. Waterman, P. Kanchanawong, M. W. Davidson, R. D. Fetter, and H. F. Hess, 2009. Interferometric fluorescent super-resolution microscopy resolves 3D cellular ultrastructure. *Proc. Natl. Acad. Sci. U.S.A.* 106:3125 –3130.

[154] Vogelsang, J., T. Cordes, C. Forthmann, C. Steinhauer, and P. Tinnefeld, 2009. Controlling the fluorescence of ordinary oxazine dyes for single-molecule switching and superresolution microscopy. *Proceedings of the National Academy of Sciences* .

[155] Heilemann, M., S. van de Linde, A. Mukherjee, and M. Sauer, 2009. Super-Resolution Imaging with Small Organic Fluorophores. *Angew. Chem., Int. Ed.* 48:6903–6908.

[156] Dempsey, G. T., M. Bates, W. E. Kowtoniuk, D. R. Liu, R. Y. Tsien, and X. Zhuang, 2009. Photoswitching Mechanism of Cyanine Dyes. *J. Am. Chem. Soc.* 131:18192–18193.

[157] Vogelsang, J., C. Steinhauer, C. Forthmann, I. H. Stein, B. Person-Skegro, T. Cordes, and P. Tinnefeld, 2010. Make them Blink: Probes for Super-Resolution Microscopy. *ChemPhysChem* 11:2475–2490.

[158] Shroff, H., C. G. Galbraith, J. A. Galbraith, and E. Betzig, 2008. Live-cell photoactivated localization microscopy of nanoscale adhesion dynamics. *Nat. Methods* 5:417–423.

[159] Klein, T., A. Loschberger, S. Proppert, S. Wolter, S. van de Linde, and M. Sauer, 2011. Live-cell dSTORM with SNAP-tag fusion proteins. *Nat. Methods* 8:7–9.

[160] Henriques, R., M. Lelek, E. F. Fornasiero, F. Valtorta, C. Zimmer, and M. M. Mhlanga, 2010. QuickPALM: 3D real-time photoactivation nanoscopy image processing in ImageJ. *Nat. Methods* 7:339–340.

[161] Smith, C. S., N. Joseph, B. Rieger, and K. A. Lidke, 2010. Fast, single-molecule localization that achieves theoretically minimum uncertainty. *Nat. Methods* 7:373–375.

[162] Greenfield, D., A. L. McEvoy, H. Shroff, G. E. Crooks, N. S. Wingreen, E. Betzig, and J. Liphardt, 2009. Self-Organization of the Escherichia coli Chemotaxis Network Imaged with Super-Resolution Light Microscopy. *PLoS Biol.* 7:e1000137.

[163] Reyes-Lamothe, R., D. J. Sherratt, and M. C. Leake, 2010. Stoichiometry and Architecture of Active DNA Replication Machinery in Escherichia coli. *Science* 328:498–501.

[164] Quan, T., P. Li, F. Long, S. Zeng, Q. Luo, P. N. Hedde, G. U. Nienhaus, and Z. Huang, 2010. Ultra-fast, high-precision image analysis for localization-based super resolution microscopy. *Opt. Express* 18:11867–11876.

[165] Andersson, S., 2008. Localization of a fluorescent source without numerical fitting. *Opt. Express* 16:18714–18724.

[166] Hedde, P. N., J. Fuchs, F. Oswald, J. Wiedenmann, and G. U. Nienhaus, 2009. Online image analysis software for photoactivation localization microscopy. *Nat. Methods* 6:689–690.

[167] Dertinger, T., R. Colyer, G. Iyer, S. Weiss, and J. Enderlein, 2009. Fast, background-free, 3D super-resolution optical fluctuation imaging (SOFI). *Proc. Natl. Acad. Sci. U.S.A.* 106:22287–22292.

[168] Dertinger, T., R. Colyer, R. Vogel, J. Enderlein, and S. Weiss, 2010. Achieving increased resolution and more pixels with Superresolution Optical Fluctuation Imaging (SOFI). *Opt. Express* 18:18875–18885.

[169] Stetson, P., L. Davis, and D. Crabtree, 1990. Future development of the DAO-PHOT crowded–field photometry package. *In* CCDs in Astronomy, ASP Conf. Ser. ASP, San Francisco, Volume 8, 289–304.

[170] Holden, S. J., S. Uphoff, and A. N. Kapanidis, 2011. DAOSTORM: an algorithm for high density super-resolution microscopy. *Nat. Methods* 8:279–280.

[171] Shannon, C., 1949. Communication in the Presence of Noise. *Proc. Inst. Radio Eng.* 37:10–21.

[172] van de Linde, S., S. Wolter, M. Heilemann, and M. Sauer, 2010. The effect of photoswitching kinetics and labeling densities on super-resolution fluorescence imaging. *J. Biotechnol.* 149:260–266.

[173] Bates, M., B. Huang, and X. Zhuang, 2008. Super-resolution microscopy by nanoscale localization of photo-switchable fluorescent probes. *Curr. Opin. Chem. Biol.* 12:505–514.

[174] Dempsey, G., W. Wang, and X. Zhuang, 2009. Fluorescence imaging at sub-diffraction-limit resolution with stochastic optical reconstruction microscopy. *Handbook of Single-Molecule Biophysics* 95–127.

[175] de la Pena, M., R. White, and P. Greenfield, 2001. The PyRAF Graphics System. *In* Astronomical Data Analysis Software and Systems X. Volume 238, 59.

[176] Tody, D., 1986. The IRAF Data Reduction and Analysis System. *In* Society of Photo-Optical Instrumentation Engineers (SPIE) Conference Series. Volume 627, 733.

[177] Stallinga, S., and B. Rieger, 2010. Accuracy of the Gaussian Point Spread Function model in 2D localization microscopy. *Opt. Express* 18:24461–24476.

[178] Giannone, G., E. Hosy, F. Levet, A. Constals, K. Schulze, A. Sobolevsky, M. P. Rosconi, E. Gouaux, R. Tampé, D. Choquet, and L. Cognet, 2010. Dynamic Superresolution Imaging of Endogenous Proteins on Living Cells at Ultra-High Density. *Biophys. J.* 99:1303–1310.

[179] Jungmann, R., C. Steinhauer, M. Scheible, A. Kuzyk, P. Tinnefeld, and F. C. Simmel, 2010. Single-Molecule Kinetics and Super-Resolution Microscopy by Fluorescence Imaging of Transient Binding on DNA Origami. *Nano Letters* 10:4756–4761.

[180] Ptacin, J. L., S. F. Lee, E. C. Garner, E. Toro, M. Eckart, L. R. Comolli, W. Moerner, and L. Shapiro, 2010. A spindle-like apparatus guides bacterial chromosome segregation. *Nat. Cell Biol.* 12:791–798.

[181] Harris, T. D., P. R. Buzby, H. Babcock, E. Beer, J. Bowers, I. Braslavsky, M. Causey, J. Colonell, J. DiMeo, J. W. Efcavitch, E. Giladi, J. Gill, J. Healy, M. Jarosz, D. Lapen, K. Moulton, S. R. Quake, K. Steinmann, E. Thayer, A. Tyurina, R. Ward, H. Weiss, and Z. Xie, 2008. Single-Molecule DNA Sequencing of a Viral Genome. *Science* 320:106 –109.

[182] Eid, J., A. Fehr, J. Gray, K. Luong, J. Lyle, G. Otto, P. Peluso, D. Rank, P. Baybayan, B. Bettman, A. Bibillo, K. Bjornson, B. Chaudhuri, F. Christians, R. Cicero, S. Clark, R. Dalal, A. deWinter, J. Dixon, M. Foquet, A. Gaertner, P. Hardenbol, C. Heiner, K. Hester, D. Holden, G. Kearns, X. Kong, R. Kuse, Y. Lacroix, S. Lin, P. Lundquist, C. Ma, P. Marks, M. Maxham, D. Murphy, I. Park, T. Pham, M. Phillips, J. Roy, R. Sebra, G. Shen, J. Sorenson, A. Tomaney, K. Travers, M. Trulson, J. Vieceli, J. Wegener, D. Wu, A. Yang, D. Zaccarin, P. Zhao, F. Zhong, J. Korlach, and S. Turner, 2009. Real-Time DNA Sequencing from Single Polymerase Molecules. *Science* 323:133–138.